Developing Calorimeters for Thermal Transport and Biological Measurements with Picowatt Resolution

by

Sung Hoon Hur

A dissertation submitted in partial fulfillment
of the requirements for the degree of
Doctor of Philosophy
(Mechanical Engineering)
in the University of Michigan
2019

Doctoral Committee:

Professor Edgar Meyhofer, Co-Chair
Professor Pramod Sangi Reddy, Co-Chair
Associate Professor Xiaogan Liang
Assistant Professor Swathi Yadlapalli

Sung Hoon Hur

hur@umich.edu

ORCID iD: 0000-0001-6985-5937

Dedication

This dissertation is dedicated to my family and friends whose unyielding love, support and encouragement have enriched my soul and inspired me to pursue and complete research.

Acknowledgments

When I look back on my first day at U of M, I was excited to do research and study abroad. But my expectations were not always met. Most of the time, research was painful and required a huge amount of effort and time. Living abroad often made me feel lonely. The only reason I could come to this point is that I was fortunate to work with excellent mentors and coworkers over the past five and a half years. I have many people to show my sincere appreciation to. Without them, I would not have achieved a Ph. D. degree at the University of Michigan.

First of all, I am indebted to my advisor, Prof. Pramod Reddy. He gave me a chance to work in his group and taught me how to do research. He showed me an ambitious research roadmap for answering big questions, which inspired me to pursue important but challenging questions. Without his guidance, I would not have thought of trying this challenging research. He waited with patience on my slow research progress so that I could finalize my research. I appreciate his lessons, which helped me grow into a better researcher.

I am thankful to Prof. Edgar Meyhofer. His insights and knowledge in many fields saved me whenever I was stuck on research problems and could not proceed any further. Without his broad knowledge in electronics, biology and optics, I could not have accomplished my Ph. D. goals. Whenever I have a word with him about my anxiety in research, he always calms me down and gives me the confidence to overcome barriers.

I appreciate Prof. Swathi Yadlapalli for being part of my dissertation committee. She provided biological samples for my research and gave much advice on handling them. Without her, research would have taken much longer and even been painful. I also thank Prof. Xiaogan Liang for being part of my dissertation committee. Notably, his lecture on nanotechnology was the base knowledge for my nanofabrication work. His lessons helped me to fabricate calorimeters successfully.

I thank my coworkers. Without Longji, my calorimeter would not have accomplished research goals that are close to the resolution limit. Dr. Wonho Jeong is my mentor both in research and graduate life. He always cares about me and teaches me to do nanofabrication based on his extensive experience. I still miss coffee breaks with him after the nanofabrication. I thank Dr. Kyeongtae Kim and Dr. Youngsang Kim for introducing me to this research field and being excellent researcher examples for me.

I thank Rohith. As a close coworker and friend, I could share not only research but also personal concerns with him. When we began biocalorimeter research from scratch, he always pointed out issues I did not recognize so that I did not get sidetracked. Without him, I would not have finished the biocalorimeter research. I appreciate my current and past laboratory members, Bai, Yashar, Anthony, Dakotah, Ruijiao, Charles, Linxiao, Kun, Shen, Ye, Juwon and Yuxuen. With them, I enjoyed working in the laboratory and I have learned many things by interacting with them.

Finally, I would like to thank my family for their endless love. My parents and my sister supported me and gave me the courage to keep moving forward throughout my life. Without them, I would have not overcome difficulties during graduate studies. Their support and love has made me a better person.

Table of Contents

List of Figures

Abstract

Calorimetry, a heat measuring process, has opened a way to quantify generated heat, both in physical and in biological systems. The resolution of a typical calorimeter ($\dot{Q} = G_{\mathrm{Th}} \times \Delta T$) can be improved in three ways, either by improving temperature resolution (ΔT) or by reducing thermal conductance (G_{Th}) or both. With intensive efforts to improve thermal resolution, microcalorimeters can now be widely used for measuring minute heat generation and transport in the micro/nanoscale. Still, there are several topics that remain insufficiently explored due to sensitivity limitations.

One unanswered question in nanoscale thermal science is of thermal transport in single-atomic or single-molecular junctions. Similar to electrical conductance, many theoretical studies suggest that thermal conductance is also quantized. While quantized electric conductance ($2e^2/h$ or 1/12.9 $k\Omega^{-1}$) was measured in the late 20th century, quantized thermal conductance measurements at room temperature ($\pi^2 k_B^2 T/3h$ or 300 pW/K) have been challenging due to insufficient calorimeter resolution and technical obstacles in creating stable atomic junctions.

A second elusive measurement is metabolic rates in small model organisms. This research is fueled by accrued evidence that human diseases, such as cancer and obesity, and aging are correlated to abnormal metabolic states. Recent advances in calorimetry have benefitted from both

operations in a vacuum where parasitic heat conduction can be attenuated and the use of microfabrication tools which significantly decrease thermal conductance and increase temperature resolution. However, such approaches cannot be simply adopted for biological systems so that none of the currently available bio-calorimetric tools are capable of the sub-nW resolution that is necessary for resolving *C. elegans* metabolic heat output. Biocalorimetery has to be performed in a liquid environment to keep organisms alive, and the size of calorimeters cannot be smaller than that of the micro-sized biological organisms. Moreover, integration of optical imaging is challenging as this naturally couples environmental temperature fluctuations into the system.

This dissertation presents two types of calorimeters. The first calorimeter is to measure thermal conductance at atomic scale, especially in single atomic or single-molecular junctions. It features a high stiffness (10 N/m) for stably holding atomic and molecular junctions at room temperature. Further, we achieved both a high temperature resolution (0.6 mK in a 10 Hz bandwidth) and a low thermal conductance (800 nW/K) of thermal bridge to resolve quantized thermal conductance (300 pW/K) in atomic junctions and length independent thermal conductance (25 pW/K) in molecular junctions. The second calorimeter is employed to measure metabolic heat outputs from *C. elegans*. Specifically, we achieved unprecedented heat resolution of 270 pW for biological systems, which represents a 500-fold improvement over calorimeters employed for past *C. elegans* studies and a 10-fold improvement compared to the state-of-the-art bio-calorimeters. This advance was realized by 1) achieving a low thermal conductance of 27 μW/K by operating in a high vacuum environment and attenuating the radiative conductance via gold coating, 2) achieving temperature stability of ±5 μK over a day using three nested shields with independent temperature control for each shield. Using this calorimeter, we demonstrate for the first time, time-resolved metabolic measurements of single *C. elegans* from ~4 nW for the L1 stage to ~100 nW

for the adult stage. These demonstrations clearly highlight the broad potential of this tool for studying the role of metabolism in disease, development and aging of small model organisms and single cells.

Chapter 1

Overview

1.1 Perspective

Energy conversion and heat transport have been, and are expected to continue to be, critical in science and engineering because of their high relevance to societal needs[1]. More than 50% of total energy consumption is spent on heating homes and providing heat for industrial purposes[2-4]. Therefore, it is impossible to differentiate thermal science from global concerns like energy inequality and climate change[5,6]. Although thermal science has been widely explored for centuries since industrialization, the role of thermal science has become more important with the advent of nanotechnology[7-11].

For example, as the size of transistors has shrunk from millimeter to nanometer scale over the decades, the integration density of transistors within the same chip size has increased dramatically resulting in very high densities of hear generation. That heat concentration brings thermal management issues[12,13]. Moreover, classical hat transfer laws in the macroscopic world are inadequate for describing nanoscale thermal transport phenomena[14]. As a result, several theoretical studies were launched, and experimental techniques to measure thermal transport phenomena were also introduced[15].

For probing thermal properties at the nanoscale, miniaturized thermometers or calorimeters were introduced[16,17]. Scanning thermal microscopy (SThM) and microcalorimetry are representative techniques for probing nanoscale thermal phenomena. SThM is a technique where a thermometer-integrated atomic force microscope probe is employed to simultaneously map topography and temperature[18] with nanometer resolution. Microcalorimeters measure heat output and temperature changes but are not designed for scanning purposes[19]. Through these tools (SThM and microcalorimeter), on can explore many interesting questions such as near-field[20] and far-field radiative enhancement[21], thermo-photovoltaic effects[22], nanoscale temperature mapping in ultra-high vacuum systems[23], molecular thermoelectrics[24] and molecular Peltier cooling[25].

Notably, developing the capabilities for probing single-atom and single-molecule thermal conductance is necessary to test numerous theoretical expectations, for example that thermal conductance will be quantized in atomic junctions and thermal conductance will be constant with respect to the length of a single molecule junction[26-30]. These measurements must precede atomic-scale electronic devices, which are the ultimate ends of electric components miniaturization.

Nanotechnology has also initiated research into micro-sized biochemical sensors[31-33]. Biochemical microsensors or microfluidic sensors are of interest in both academia and industry due to two critical reasons. First, they can save research and development costs significantly because a microsensor necessitates a very small amount of specimen in each test. These sensors, often called a lab on a chip, enable dozens of screening tests with samples less than a nano-liter within a minute[34]. Due to these advantages, microfluidic devices have been widely investigated and applied to biological research or medical fields[35,36]. Secondly, microsensors are expected to be capable of resolving heat outputs associated with biochemical reactions in small-sized model organisms such as *C. elegans* and single cells. Over the past 30 years, nanoscale thermal science

has played an important role in studying dissipated heat rates in biological samples through various approaches, from indirect calorimetry to direct calorimetry[37].

In order to make progress towards understanding thermal transport at the atomic scale and metabolic heat output from model organisms, I developed calorimeters to answer two questions. The first goal of my research is to experimentally probe thermal transport in single-atomic junctions and single-molecular junctions. It is now well known that electrical charge transport properties of metallic junctions are quantized regardless of temperature, both at low temperatures and at room temperature[26]. Although theoretical studies of thermal transport have accrued, experimental approaches have not yet probed quantized thermal conductance[29]. Besides, the single-molecular thermal conductance was expected to be constant regardless of the molecular lengths, which is counter-intuitive because the thermal conductance is typically known to be inversely proportional to the length[27,28,30]. Therefore, probing thermal conductance along atomic junctions or molecular junctions is expected to take nanoscale thermal science to the next level of sophistication.

The second question, I address in this thesis is whether one can probe real-time metabolic heat outputs from a microscopic organism. Past studies of metabolic heat outputs from biological samples have been largely limited to relatively larger biological samples. Recent technical advances from our group, that achieved ~100 nW resolution heat output measurements have made it possible to probe the metabolism of individual *Drosophila* in real time[38]. However, probing the metabolism of individual cells or small model organisms such as *C. elegans* is much more challenging as on needs sub-nW resolution. In fact, past studies have employed tens of thousands of cells in aggregation[39,40] to probe metabolism from cells and only managed to obtain an averaged

value of the metabolic heat output and that real-time metabolic heat output variance during an organism's physiological activities could not be differentiated.

1.2 Past works on calorimeter developments

The modern concept of calorimetry to understand thermal transport started from Lavoisier's calorimeter development in the late 18th century[39]. His calorimetry opened a way of quantifying the amounts of heat both in nature as biological metabolic rate, and in electronics as device heat dissipation[39,41,42].

The basic principle of any calorimetry technique is as follows[43]. A sensing chamber with temperature T is connected to a thermal reservoir (Figure 1.1). When heat is applied to the sensing chamber, the sensing chamber's temperature increases by ΔT. Until this point, a thermometer in the sensing chamber detects the temperature change but does not dictate the rate of heat transfer along a thermal bridge between the sensing chamber and thermal reservoir. Here, thermal conductance is required to quantify applied heat to the sensing chamber. This relationship can be written as

$$\dot{Q} = G_{\mathrm{Th}} \times \Delta T = \frac{\Delta T}{R_{\mathrm{Th}}} \tag{1.1}$$

The resolution of a typical calorimeter ($\dot{Q} = G_{\mathrm{Th}} \times \Delta T$) can be improved in two ways, either by improving temperature resolution (ΔT) or by reducing thermal conductance (G_{Th}). There are three key factors to achieve high-resolution calorimeters: 1) an effective thermal isolation of the sensing chamber from the thermal reservoir for G_{Th} reduction, 2) an integration of a very sensitive thermometer to sense minute changes of ΔT in the sensing chamber, and 3) an

introduction of a stabilized thermal system to reduce temperature fluctuations of the thermal reservoir and the sensing chamber.

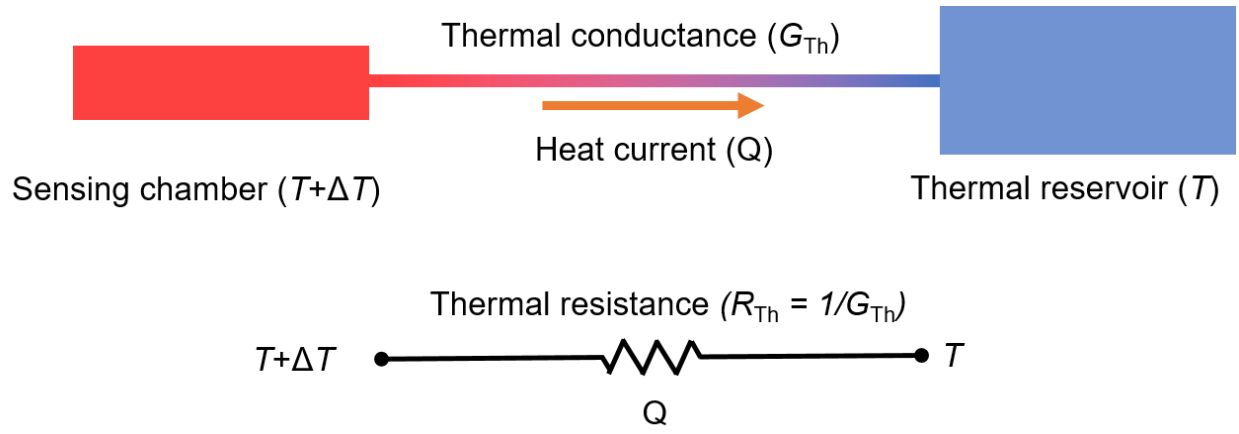

Figure 1.1 Basic principle of a calorimeter.
Note that lowering thermal conductance (G_{Th}) or increasing thermal resistance (R_{Th}), improving thermal resolution (Δ***T***), and achieving a stable reference temperature (***T***) are key factors for a high-performance calorimeter

With the application of vacuum systems and microfabrication, the thermal conductance and temperature stability of calorimeters have been significantly reduced and improved, respectively. Researchers implemented a suspended structure to the calorimeter design to reduce thermal conductance between the sensing chamber and the thermal reservoir. Since there is no gas-attributed conduction/convection under vacuum conditions, two heat pathways (thermal conduction along the beam $G_{\mathrm{Th,cond}}$ and thermal radiation $G_{\mathrm{Th,rad}}$) are usually considered. The thermal conductance of a beam is written as

$$G_{\mathrm{Th,cond}} = \frac{kA_c}{L} \tag{1.2}$$

where k is the thermal conductivity of the beam material, A_c is the cross-sectional area of the beam, and L is the length of the suspended beam. To achieve low thermal conductance of the

beam ($G_{\mathrm{Th,cond}}$), lower k materials such as silicon oxide, silicon nitride, or parylene are widely used[38,42,44-46]. Instead of flat thin films, grooved structures such as T-shaped beams are introduced to increase mechanical stiffness while reducing the cross-sectional area of the beam (A_c). Increasing the length of beams (L) can be an option but it could result in an increase of the time constant such that it is a less preferred option.

The contribution of thermal radiation becomes dominant as the structure size (L) decreases due to an increase of surface-to-volume ratio (area/volume ≈ *1/L*). The thermal radiation amount is approximated to

$$G_{\mathrm{Th,rad}} = 4\epsilon\sigma T_{avg}^{3} A, \tag{1.3}$$

where ϵ is the emissivity of the material, σ is the Stefan-Boltzmann constant, T_{avg} is the average temperature of the calorimeter, and A is the surface area of the calorimeter. Therefore, thermal conductance from radiation cannot be neglected, and thus researchers have coated the sensing chamber and thermal bridges with less emissive materials, such as gold (Au)[38].

Current microcalorimetric tools have achieved sub-picowatt resolution[42,44,45]. This resolution was realized by reducing thermal conductance of a calorimeter thermal bridge, by integrating a sensitive thermometer, and by achieving a temperature stabilizing control system. As microcalorimetry resolution has improved, more interesting thermal phenomena in micro/nanoscale are now able to be probed. The measurement of the thermal conductivity measurement of single-walled carbon nanotubes is a notable example[47] of advances enabled by micro-calorimetric tools. Although carbon nanotubes intrigued many researchers due to their directional thermal conductivity, their thermal conductivity could not be measured using past techniques such as the 3ω method[48] and time-domain thermoreflectance (TDTR)[49] for thin-films,

the pulsed power technique[50], and the laser flash method[51] which are used for bulk materials. This is because often very small and the high resolution of microcalorimeters is necessary for probing thermal transport and thermal conductance of 1D nanostructures. In fact the thermal conductance of carbon nanotubes was measured using a microcalorimeter by suspending a single nanotube in a vacuum between two suspended micro-calorimeters[47,52].

Microcalorimeters have also been used recently to demonstrate the breakdown of Planck's law in nanoscale gaps due to far-field and near-field radiation enhancement[20-22]. When the gaps between two surfaces are close to sub-micrometer, the classical Planck's radiation theory is no longer valid, and significant radiation enhancement can be observed. However, probing its effect through measurement was challenging due to experimental difficulties such as a realization of nanometer gap between two surfaces. Scanning thermal microscopy probes enabled local near-field enhancement using the tip[20], and a microcalorimeter successfully observed plate-to-plate large area near-field enhancement[37]. These findings will be useful to develop efficient heat exchangers or thermophotovoltaic devices[22]. Moreover, far-field enhancement when the thickness of the two planes thinner than the electromagnetic wavelength was also observed using microcalorimeters[21].

Even though calorimetric resolution has improved, there are still many topics that remain insufficiently explored due to sensitivity limitations. One big goal is to measure ultimate thermal conductance along single-atomic or molecular junctions. It is extremely challenging because the previous microcalorimeters were lacking in mechanical stability and sensitivity. Another challenging research goal is in the biochemical field, which is to probe metabolic rates of biological samples. In fact, metabolic rate measurement was an initial purpose of the calorimeter invented by Lavoisier in the late 18th century. However, the resolution of the biocalorimeters has not been

improved as much as general microcalorimeters for physical reaction measurements[45,46,53]. General microcalorimeters for probing thermal properties in inorganic materials are not applicable in metabolic rate measurements because they are miniaturized to increase sensitivity and no longer integrate liquid systems to sustain physiological activities. Therefore, the biocalorimeter is an important but insufficiently investigated device.

1.3 Organization of the dissertation

In this chapter, I briefly summarized the background of nanoscale thermal science and calorimetry. From this background, I have discussed the importance of experimentally probing heat transport in various fields. The organization of the rest of this thesis is as follows.

This dissertation presents two types of calorimeters which I have investigated in the past few years. Figure 1.2 shows two types of calorimeters that I developed. Chapter 2 addresses the calorimeter development to probe thermal transport at an atomic scale. The nanofabrication of calorimetric scanning thermal microscopy (C-SThM) probes is a core part of our work to examine the quantized thermal conductance in atomic junctions and the hypothesis of length independent molecular thermal conductance. By employing novel, custom-fabricated, picowatt-resolution calorimetric scanning probes, we measured the thermal conductance of gold and platinum metallic wires down to single-atom junctions. Our work reveals that the thermal conductance of gold single-atom junctions is quantized at room temperature, and shows that the Wiedemann-Franz law, which relates the thermal and electrical conductivities in metallic materials at the macroscopic length scale, is satisfied even in single-atom contacts. The experimental techniques reported here enable thermal transport studies in atomic and molecular chains, which are key to investigating numerous fundamental issues that have remained experimentally inaccessible.

In Chapter 3, sub-nanowatt resolution calorimetry that was employed to probe nanowatt range metabolic heat output from *C. elegans* is addressed. The size of biocalorimeters cannot be reduced to nanoscale dimensions due to the size of the liquid channel and the size of biological organisms. Since indirect calorimeters such as respirometers are only applicable to aerobic conditions, direct metabolic heat output measurements provide a more accurate characterization of metabolism, as they capture both aerobic and anaerobic components. However, such measurements have been limited due to lacking sensitivity, difficulties in controlling environmental temperature, and resolving a very small amount of released heat. I present a sub-nanowatt resolution calorimeter that I employed to probe the nanowatt-range metabolic heat output from *C. elegans*. A temperature control system with a vacuum was extensively leveraged to stabilize the experimental setting to resolve sub-nanowatt resolution in biological systems, which is the best resolution to date.

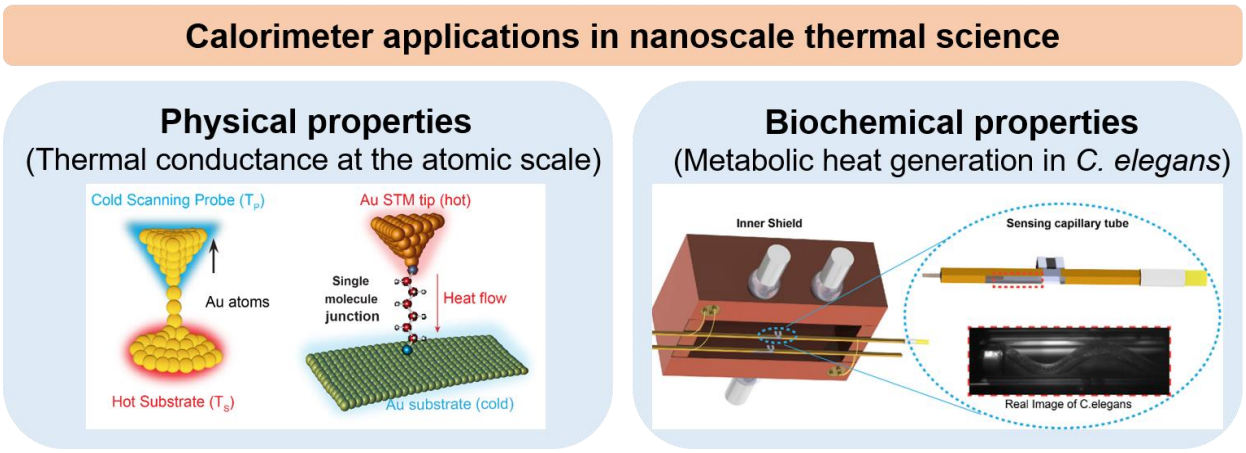

Figure 1.2 Calorimeter applications covered in this dissertation.
Each calorimeter was designed for probing physical properties (thermal conductance at atomic scale, Chapter 2[54,55] and biochemical properties metabolic heat generations, Chapter 3).

Chapter 2

A Calorimeter Development for Probing Thermal Transport at The Atomic Scale

This chapter focuses on the calorimeter developments for obtaining quantized thermal transport in single-atomic junctions and thermal conductance of single-molecule junctions that resulted in two publications[54,55]. Please note that the text and illustrations in this chapter are largely based and are reproduced with permission of *Science Magazine* and *Nature*. In addition, significant portions of the papers have also been rewritten to emphasize the role of calorimetry and my contributions to this work. Finally, I want to acknowledge the contributions of my collaborators *Longji Cui, Wonho Jeong, Manuel Matt, Jan C. Klöckner, Fabian Pauly, Peter Nielaba, Juan Carlos Cuevas, Zico Alaia Akbar, Sung-Yeon Jang, Pramod Reddy* and *Edgar Meyhofer* who have made to this work.

2.1 Abstract

Thermal transport in individual atomic junctions or molecular junctions is of great fundamental interest due to unique effects expected to arise in those systems. However, measurement of thermal conductance in single-atomic junctions or single-molecular chains has been inaccessible, owing to the challenge of detecting minute heat currents at the picowatt level. Here, by employing novel, custom-fabricated, picowatt-resolution calorimetric scanning probes, we measure the thermal conductance of gold and platinum metallic wires down to single-atom

junctions. Our work reveals that the thermal conductance of gold single-atom junctions is quantized at room temperature and shows that the Wiedemann-Franz law, which relates the thermal and electrical conductivities in metallic materials at the macroscopic length scale, is satisfied even in single-atom contacts. Besides, when used in conjunction with a time-averaging measurement scheme to increase the signal-to-noise ratio, picowatt-resolution scanning probes also allow quantification of the much lower thermal conductance of single-molecule junctions. Our experiments on prototypical Au–alkanedithiol–Au junctions containing two to ten carbon atoms confirm that thermal conductance is to a first approximation independent of molecular length. The experimental techniques reported here will enable thermal transport studies in many one-dimensional systems, such as atomic junctions, short molecules and polymer chains, which is key to investigating numerous fundamental issues that have remained experimentally inaccessible.

2.2 Introduction

2.1.1 Quantized thermal transport in single-atom junctions

The study of thermal transport at the nanoscale is of critical importance for the development of novel nanoelectronic devices and holds promise to unravel quantum phenomena that have no classical analogs[7,11,56]. In the context of nanoscale devices, metallic atomic-size contacts[26] and single-molecule junctions[57] represent the ultimate limit of miniaturization and have emerged as paradigmatic systems revealing previously unknown quantum effects related to charge and energy transport. For instance, transport properties of atomic-scale systems—such as electrical conductance[58], shot noise[59,60], thermopower[24,61,62], and Joule heating[63]—are completely dominated by quantum effects, even at room temperature. Therefore, they drastically differ from those of

macroscale devices. Unfortunately, the experimental study of thermal transport in these systems constitutes a formidable challenge and has remained elusive to date, in spite of its fundamental interest[64].

Probing thermal transport in junctions of atomic dimensions is crucial for understanding the ultimate quantum limits of energy transport. These limits have been explored in a variety of microdevices[29,65-68], where it has been shown that irrespective of the nature of the carriers (phonons, photons, or electrons), heat is ultimately transported via discrete channels. The maximum contribution per channel to the thermal conductance is equal to the universal thermal conductance quantum $G_{0.Th} = \pi^2 {k_B}^2 T/3h$, where $k_B$is the Boltzmann constant, T is the absolute temperature, and h is the Planck constant. However, observations of quantum thermal transport in microscale devices have only been possible at sub-Kelvin temperatures, and other attempts at higher-temperature regimes have yielded inconclusive results[69].

The energy-level spacing in metallic contacts of atomic size is on the order of electron volts (i.e., much larger than thermal energy). Therefore, these junctions offer an opportunity to explore whether thermal transport can still be quantized at room temperature. However, probing thermal transport in atomic junctions is challenging because of the technical obstacles in reproducibly creating stable atomic junctions while measuring the minuscule heat currents flowing through the atomic chains. Here, we present an experimental platform that allows us to measure the thermal conductance of metallic wires down to the single-atom limit. With this technique, we were able to observe quantized thermal transport at room temperature.

2.2.2 Thermal conductance of single-molecule junctions

Studies of charge and heat transport in molecules are of great fundamental interest, and are of critical importance for the development of a variety of technologies, including molecular

electronics[70], thermally conductive polymers[71], and thermoelectric energy-conversion devices[64]. Given this overall importance and the daunting experimental challenges, a number of initial studies explored charge transport in ensembles of molecules[72,73]. Although such measurements provided important insights, researchers gradually began to realize that it was necessary to develop single-molecule measurement techniques[24,63,74-76] to avoid the confounding effects of ensemble measurements, including uncertainties in the actual number of molecules contributing to transport through the junctions and the effects of intermolecular interactions, and to study systematically the electrical conduction properties of genuine single-molecule entities. Corresponding efforts over the past decade have been made to experimentally characterize heat transport in ensembles of molecules such as self-assembled monolayers[77-79] and polymer nanofibres[71,80]. Not surprisingly, these thermal ensemble measurements face challenges and uncertainties similar to those found in previous monolayer electrical measurements, and intermolecular interactions are expected to have an influence on the thermal transport properties of molecular junctions[27,81]. Although recent research[55,82] has enabled heat transport studies in metallic single-atom junctions (where thermal conductances are in the region of 500 pW K^{-1}), similar efforts for single-molecule junctions, where contributions to heat transport by electrons are negligible and heat flow is instead dominated by phonons resulting in low thermal conductance values (tens of picowatts per Kelvin), have remained inaccessible owing to experimental challenges in detecting such small conductances. Therefore, experiments have yet to reproduce the results of theoretical calculations which have predicted several interesting thermal transport properties in one-dimensional molecular and polymer junctions[27,28,30,83].

2.3 Fabrication of the caloric scanning thermal microscope (C-SThM) probe

For thermal measurements, a custom-made thermal probe was a prerequisite because there were no compatible probes for our experiment. In collaboration with Dr. *Wonho Jeong*, I microfabricated scanning thermal microscope probes and characterized their performance.

To measure thermal conductance of atomic junctions or molecular junctions, a thermal probe necessitates three critical features: 1) High stiffness to prevent vibrations, 2) sufficient sensitivity to resolve minute thermal signals, and 3) a metal (most often Au) layer on the sidewall of probe tip for forming Au junctions.

Generally, the tip of a thermal scanning probe is oriented vertically relative to the body of the probe for scanning substrates. In contrast, the tip of our probe is not in a vertical direction, but parallel to the probe body (Figure 2. 10 and 11). This orientation results in a very high stiffness in the axis normal to the substrate and makes possible to maintain atomic junctions for extended periods of time. Usual contact-mode AFM probes are comparatively compliant (less than 1 N/m), so that the probe's tip is attracted to the surface by van der Waals forces[84] at distances of a few nanometers. This is often referred to as snap-in. To avoid snap-in and approach the Au or molecular substrate in a controlled manner, the probe is slowly withdrawn from the surface until a single-atomic or molecular junction is formed.

One of the significant challenges in room temperature probe measurements are thermal vibrations whose amplitude is inversely related, as described by the equipartitioning theorem, to the square-root of the stiffness of the probe. Once atomic junctions are formed, the probe should maintain its connection for a long time to resolve the thermal signal, but thermal vibrations at room temperature result in excessively-large fluctuations with compliant cantilever. For this reason, a stiff cantilever with minimized vibrations and deflections is required.

At the same time, thermal conductance should be minimized to increase thermal sensitivity. Lowering the thermal conductance of the probe, ($G_{th,P}$), is critical to increasing the sensitivity of the probe. The expected thermal conductance along a single Au atomic junction is ~500 pW/K. If the temperature difference between a substrate and probe is ~20 K, then ~10 nW is expected to be transferred to the probe. In this case, the thermal conductance of the probe should not exceed 1 μW/K because the probe temperature resolution of the probe is limited to ~ 1mK (with a bandwidth of 100 Hz) due to thermal drift and electronic noise (Johnson Noise)

However, there is a trade-off between stiffness increase and thermal conductance reduction of a cantilever beam in a typical geometric design cantilever. To balance both goals (a high stiffness and a low thermal conductance) a T-shaped beam design was adopted.

A T-shaped beam has a larger width and height while maintaining a smaller cross-sectional area. Thus, the increase in stiffness is large while the thermal conductance increases comparatively little. For microfabricated probes, the first T-shaped beam was implemented by Miner[85]. To microfabricate such cantilevers, a trench is defined and the gap is filled with SiN_x to increase the stiffness of probe from 0.1 N/m to more than 10 N/m. The increased stiffness can be calculated from Euler-Bernoulli beam theory or classical beam theory:

$$Stiffness\left[\frac{\mathrm{N}}{\mathrm{m}}\right] = \frac{applied\ force}{beam\ deflection} = \frac{F}{\delta_{beam}} = \frac{EI}{L^3} \tag{2.1}$$

where E, I, and L are the modulus of elasticity, a moment of inertia and beam length, respectively[86]. Here, E is determined by the material selection and I is determined by cross-sectional shape. In Figure 2.1, two types of beams are presented to show the difference in the moment of inertia.

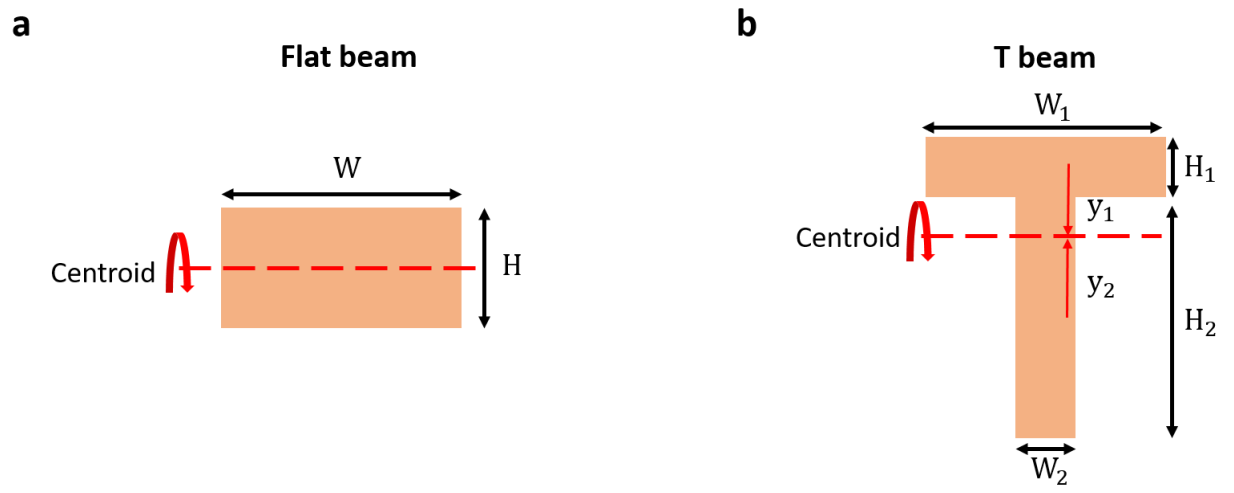

Figure 2.1 Moment of inertia (*I*) in two different beam structures.
(a) A flat beam with width (W) and a thickness (H). A centroid is located at the center of the beam. This is a typical structure of AFM probes. (b) T-shaped beam. T-beams are not commonly used in AFM cantilever, but these structures (T-beam or H-beam) are commonly used in construction fields.

The moment of inertia can be acquired from the equation.

$$I = \frac{WH^3}{12} \; in\ a\ flat\ beam \tag{2.2}$$

$$I = \frac{W_1{H_1}^3}{12} + \frac{W_2{H_2}^3}{12} + W_1H_1{y_1}^2 + W_2H_2{y_2}^2 \; in\ a\ T\ beam \tag{2.3}$$

In this case, if we assume: 1) W is ten times longer than H; 2) $W = W_1 = H_2$; 3) $H/2 = H_1 = W_2$, then the stiffness of a T beam (Figure 2.1(b)) is 132 times larger than that of a flat beam with the same cross-sectional area. In other words, the stiffness can be 132 times greater with the same thermal conductance (G_{Th}) using a simple beam structure modification.

The second challenging part was to increase the sensitivity of the probe. Both a decrease in thermal conductance and a highly resistive sensor contributes to sensitivity improvement. We used platinum (Pt) as a resistive material because it provides a stable temperature coefficient of resistance (TCR, ~0.2 %/K) with no hysteresis[87]. Although this material has widely been adopted in microcalorimeters, integrating a Pt heater into a small size probe tip is a challenge due to a

limited lithography resolution. We patterned Pt serpentine with 1 μm width of the lines and a 0.8 μm gap between lines. In general, Pt is a widely used material for the thermal sensing and heating current line, whereas a signal sensing line generally consists of Au. This is because a low resistance is preferred to sense signals and higher resistance is required for heater lines. When Pt lines and Au lines are patterned and deposited, there is a risk of electrical shortage because two lines are in close proximity to each other. Here, both Pt and Au lines are united to Pt to avoid multiple fabrication processes to prevent a shortage between two lines. We reduced the thickness down to 30 nm to further increase resistance. As a result, we could achieve a desirable range resistance (~25 kΩ) of the Pt resistive heater sensor.

The last challenging part of microfabrication was to deposit Au on the tip's sidewall. The Au (or Pt) should be placed on the side of the probe tip 1) to realize an uninterrupted electrical current flow and 2) to form atomic junctions to the Au (or Pt) substrate. Unlike a typical AFM probe, this probe approaches the substrate in a vertical direction so that a probe tip is defined in a parallel way to the probe body. Therefore, the Au (or Pt) layer must exist on the lateral side of the tip to make the metallic junction. However, the microfabrication steps are a top-down process such that no metal is deposited on the lateral side tip. Once the bulk fabrication is finished, it is challenging to selectively mask, pattern, and deposit metal only on the tip region to avoid an electrical shorting issue. There was little published data available on how to deposit metal on a sidewall. Finally, this issue was resolved by introducing a shadow mask. The probe is flipped and placed on the shadow mask to align tip to the open window so that metals are only deposited on the tip region. Figures 2.5 and 2.6 illustrate this process. Low-temperature crystal bond is used as adhesives. This alignment and the sputter's isotropic directionality result in the probe tip's sidewall being covered by metals. The alignment for this approach is somewhat difficult, because the probe

must be flipped and placed onto the shadow mask without being damaged during the mounting and unmounting procedures.

The steps involved in the nanofabrication of the C-SThM probes are shown in Figure 2.2.

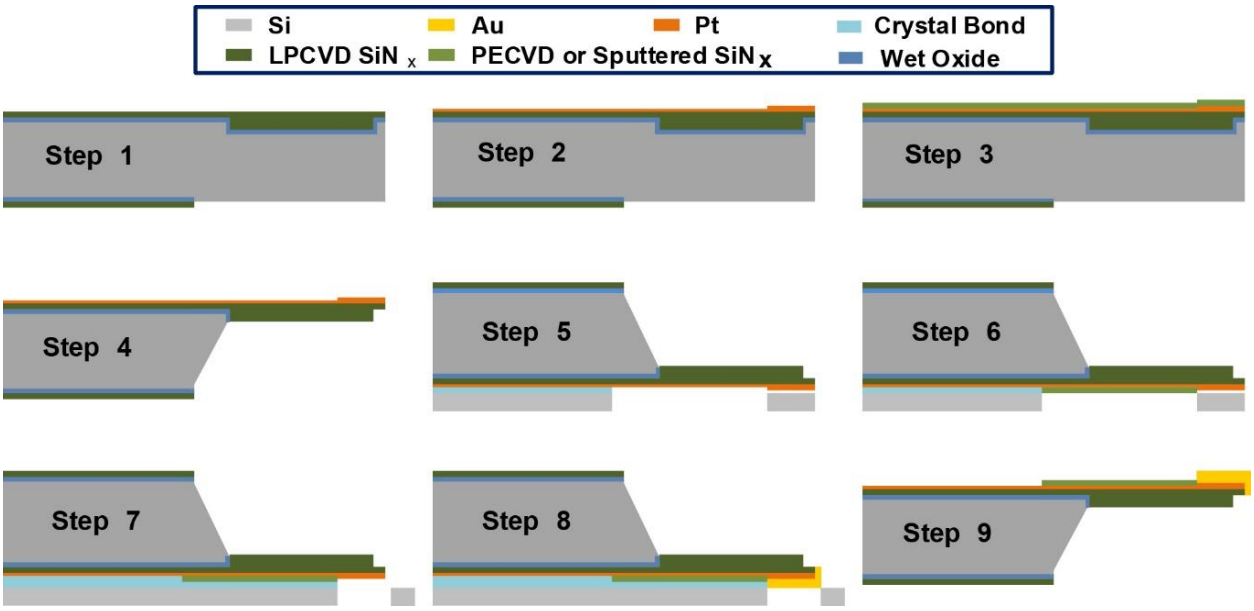

Figure 2.2 Microfabrication steps for thermal probes.
(Step 1) Backside and T-shaped cantilever patterning. (Step 2) Deposition of Pt for serpentine resistive sensor, pads and the tip. (Step 3) SiN_x layer deposition for the frontside KOH etching. (Step 4) Probe cantilever release. (Step 5) Aligning each probe on the first shadow mask using a thin low-temperature crystal bond layer. (Step 6) SiN_x sputtering on the Pt-serpentine covered region. (Step 7) Aligning each probe on the second shadow mask. (Step 8) Au sputtering on the tip region. (Step 9) Detaching the scanning probe from the shadow mask and removing the residual crystal bond by piranha cleaning.

The fabrication process proceeds as follows.

Step 1)

Fabrication begins with a double side polished silicon (Si) wafer. A photoresist was coated on the wafer through SPR220 (3.0) spin-coating of the wafer at 500 rpm for 7 seconds and at 3000 rpm for 35 seconds. A post-bake at 115 °C for 2.5 minutes is required after spinning. Since this process is repeated multiple times in the microfabrication process, it is named “PR coat” afterward. A T-shaped beam pattern is defined by photolithography using a stepper (GCA AS200 AutoStep) with 0.35 seconds of exposure time. The beam is soft-baked at 115°C for 2.5 minutes, then

developed with AZ 726 until all features are entirely developed. Subsequently, O_2 plasma cleaning for 1 minute at 100 mW is performed. These soft-bake, development and descum processes are also repeated multiple times so that it is named "development" afterward. The Si wafer is plasma etched for 20 minutes using STS Pegasus 4 (DRIE recipe 1). Subsequently, the PR is completely stripped using acetone and a short (~ a half minute) clean in piranha solution.

In Figure 2.3, a T-shaped cantilever is realized by making a trench on the Si wafer followed by 500 nm wet oxidation (using a S1T2 furnace). A 600 nm thick low-stress low-pressure chemical vapor deposition (LPCVD) SiN_x is deposited (using a S2T4 furnace) on both sides of the wafer. It should be noted that every furnace run requires a pre-furnace clean (PFC) before the step. The wet oxidation is to narrow down the trench width to reduce thermal conductance along the cantilever beam. LPCVD SiN_x is chosen for the cantilever base because it has low thermal conductivity (~1.2 W/mK) with chemical resistance during the wet etching process.

Subsequently, after PR coating, the backside is patterned by photolithography using MA/BA-6 Mask/Bond Aligner with 7 seconds of exposure time. The development process follows until all features are completely developed. The backside SiN_x is plasma etched for 4 minutes using LAM 9400. Subsequently, the PR is entirely stripped using acetone and a short (~ a half minute) clean in piranha solution. The SiN_x on the backside of the wafer is patterned to facilitate a KOH-based bulk etching to release the devices in the last step of fabrication. The KOH etching rate is anisotropic. Since Si etching has a certain angle (54º from flat water surface) so that both the front and backside probe pattern is critical to release a functionally shaped probe body. At this point, step 1 in Fig. 2.3 is accomplished.

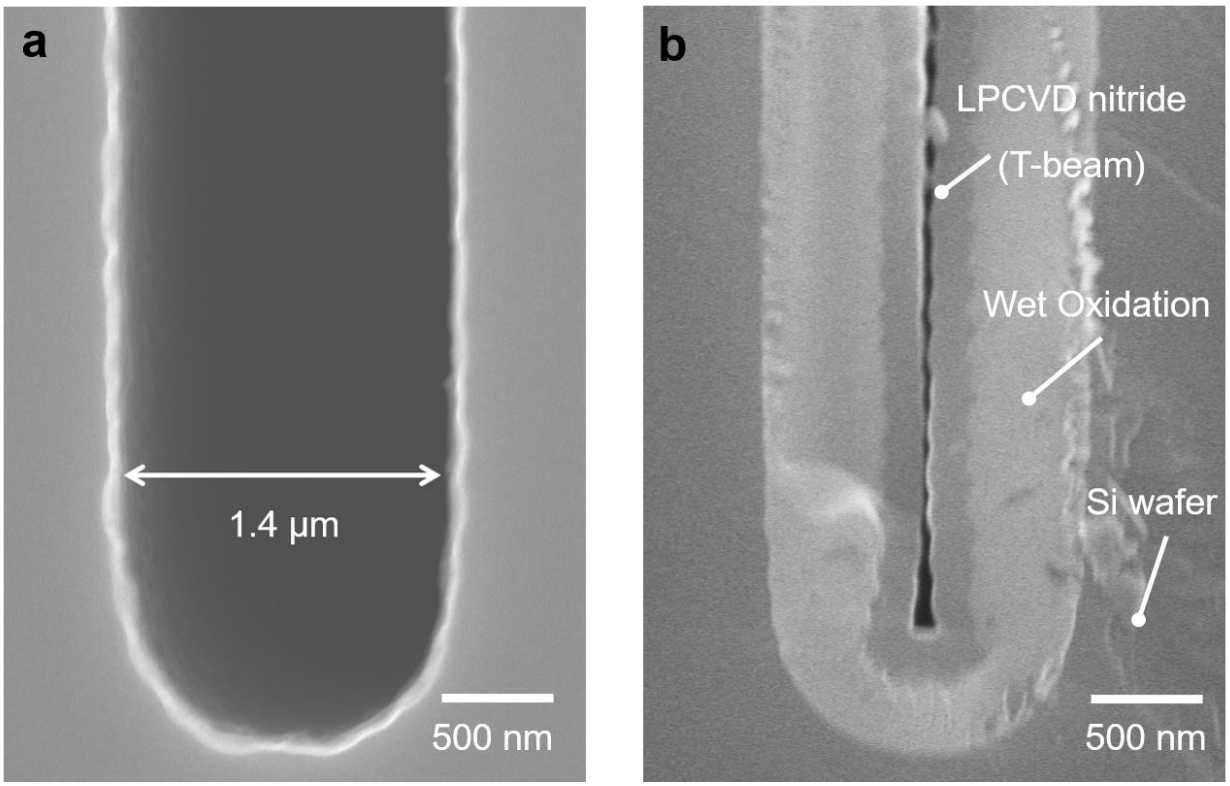

Figure 2.3 Defining a trench for T beam fabrication
(a) Cross-sectional view of a trench. DRIE was used to make an 18 μm depth and 1.4 μm wide trench. The actual trench was wider than the original mask pattern (0.8 μm wide) because of aberration and development limit in lithography. (b) Cross-sectional view of T-beam after two consecutive oxide and nitride fillings. Note that only LPCVD nitride is left after bulk etching so that we can achieve high stiffness with low thermal conductance.

Step 2)

A platinum (Pt) serpentine line (30 nm thickness, 1 μm width and 0.8 μm distance between lines) was defined by photolithography on a PR-coated wafer using a stepper (GCA AS200 AutoStep) with 0.35 seconds of exposure time, which patterns a very densely packed Pt serpentine. Development follows until all features are completely developed. 30 nm-thick Pt with a 3 nm Cr adhesion layer is deposited by evaporation using an EnerJet evaporator. Lift-off using acetone for >12 hours and a short (~ a half minute) clean in piranha solution follow. Here, both heating and sensing lines are made of Pt so that patterning and a metal deposit were processed only one time.

As a result, we avoid electrical shorting or misalignment concerns during Pt and Au lines microfabrication.

After Pt line deposition, Au pads are patterned and deposited on the pad sides and at the tip. Pad side Au can help improve wire bonding, and tip region Au addition connects the sensing Pt line to the end of the tip region. The electric resistance of the heater is 20 –30 kΩ and the electric line for sensing a junction is ~1 kΩ.

Step 3)

50 nm of PECVD SiN_x (Plasmatherm 790, 380 Silicon nitride Z recipe) is deposited to the front surface of the probe. This is for the etching time delay between the front and backside of the probe. If there is no front-side delay of KOH and both sides start etching together, there is excessive undercut on the front side which results in the cantilever and pads floating from the probe.

Step 4)

Subsequently, the T-shaped cantilever is released by a KOH etch. The KOH etching rate is known to be 1 μm/min, and it begins on the back-side due to SiN_x protection on the front-side. A 50nm layer of PECVD SiN_x prevents KOH etching on the front-side for up to 1 hour, so it causes a time delay in the etching between the front- and back-side of the wafer. Overall, KOH etching takes around 6 hours. Figure 2.4 shows a probe that has been released from the bulk etching. Note that this probe is not ready to use for actual experiments. The tip condition after step 4 is shown in Figure 2.6 (a) which denotes that the Au or Pt metal layer still needs be deposited to trap atomic or molecular junctions.

\

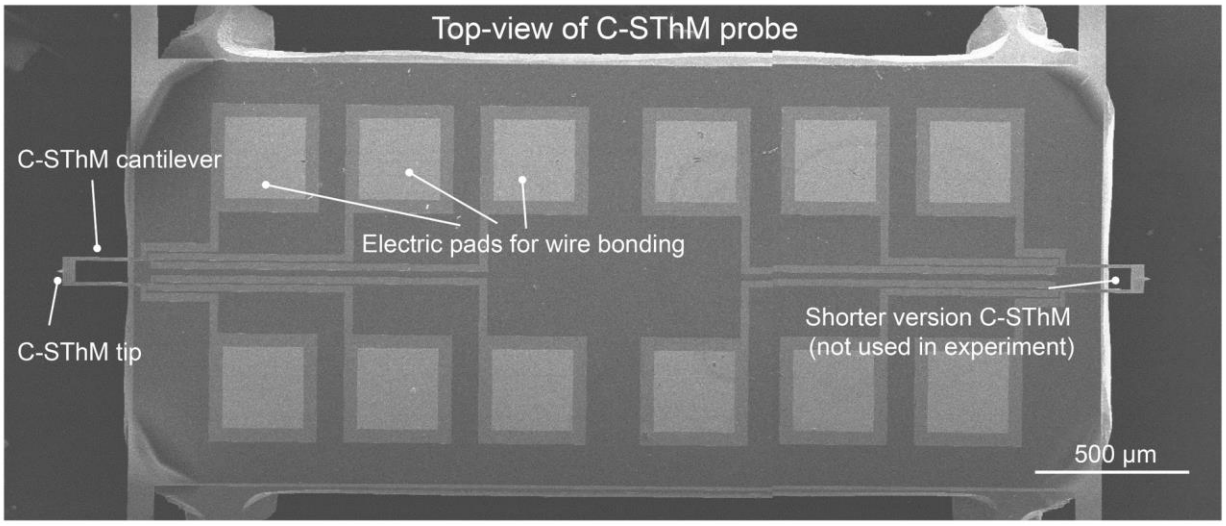

Figure 2.4 Top-down view of released probes.
There are two versions with different lengths (long and short). Here, all the experiments were conducted by the longer version.

Step 5)

After successfully releasing the probes, each of the probes is individually flipped and aligned on a shadow mask. The nanofabrication process of the shadow mask starts from a Si wafer. The use of a double-side polished Si wafer is not necessary. A 500 nm-thick low-stress low-pressure chemical vapor deposition (LPCVD) SiN_x is deposited using an S2T4 furnace on both sides of the wafer. PR is coated on the backside of the wafer. The backside pattern is patterned by photolithography using an MA/BA-6 Mask/Bond Aligner with 7 seconds of exposure time. After development, the backside of the wafer is plasma etched for 1 min using STS Pegasus 4 (DRIE recipe 1) to etch SiN_x. Subsequently, PR is completely stripped using acetone and a short clean in piranha solution (~ a half minute). Afterward, the PR coating, patterning, and development processes are repeated to acquire a front-side pattern. Finally, the shadow mask is released by KOH etching. The probe alignment on the shadow mask is challenging because each probe must

be handled separately. First, a probe is held and placed on a thin metal bar whose width is less than the probe body length to suspend the cantilever. After this, the probe is flipped using a tweezer. Simultaneously, a dilute crystal bond solution is prepared by mixing a low-temperature crystal bond with acetone. Acetone is the solvent normally used to erase crystal bond, but here it is used to dilute crystal bond. The crystal bond itself is a solid bar at room temperature. However, if it is mixed with the acetone, it becomes a diluted solution. 1 µL of this diluted liquid is dropped on the warmed shadow mask substrate using a pipette. The shadow mask is warmed at 70 °C to evaporate acetone and to melt the low-temperature crystal bond. The probe is then loaded on the shadow mask. The Pt heater integrated island is aligned to the through-hole to deposit SiN_x. Once probes are aligned, the heater is turned off to cool the wafer down to room temperature. Then crystal bond is solidified and serves as an adhesive to the probe during a wafer loading on the sputtering tool.

Step 6)

30 nm SiN_x is sputtered using the Lam18-01 tool (Kurt J. Lesker). After sputtering, the shadow mask is placed on the heater warmed at 70 °C to melt the crystal bond. When the crystal bond melts, the probes are held from the shadow mask and loaded on the thin metal bar to flip it. Afterward, the probe is cleaned to remove the remaining crystal bond using acetone and piranha solution. This SiN_x is to protect Pt serpentines during the cleaning procedure. Since Pt line is narrow and thin, aggressive plasma cleaning before loading to the UHV-system for experiments could damage the Pt sensor.

Step 7)

The alignment process is repeated in step 5) for probe alignments on the second shadow mask. The second shadow mask fabrication process is identical to the first shadow mask with a different patterning design. In Figure 2.5, the second shadow mask is to deposit metals on the

lateral side of the tip. Therefore, the probe tip region should be aligned to the shadow mask through-hole.

Step 8)

500 nm Au or Pt with 20 nm Ti as an adhesion layer is sputtered using a Lab18-02. 500 nm is deposited on the upper side of the tip so that the deposited metal thickness on the lateral side of the tip is lower than that. Based on isotropic directionality, approximately 50 nm is expected to deposit on the lateral tip end (see Figure 2.5). Note that the opening size of a shadow mask's top surface is smaller than that of the bottom surface to realize lateral side metal coating. The maximum deposition angle is determined by the thickness of mask, the size difference between the topside and the bottom of shadow mask openings. Since sputtering is isotropic, the tip should be extruded to the top side openings but the heater should be protected. The shadow mask in Figure 2.6(b) presents probes without metal coating just after a bulk release. Figure 2.6(c) clearly shows deposited metal at the end of the tip.

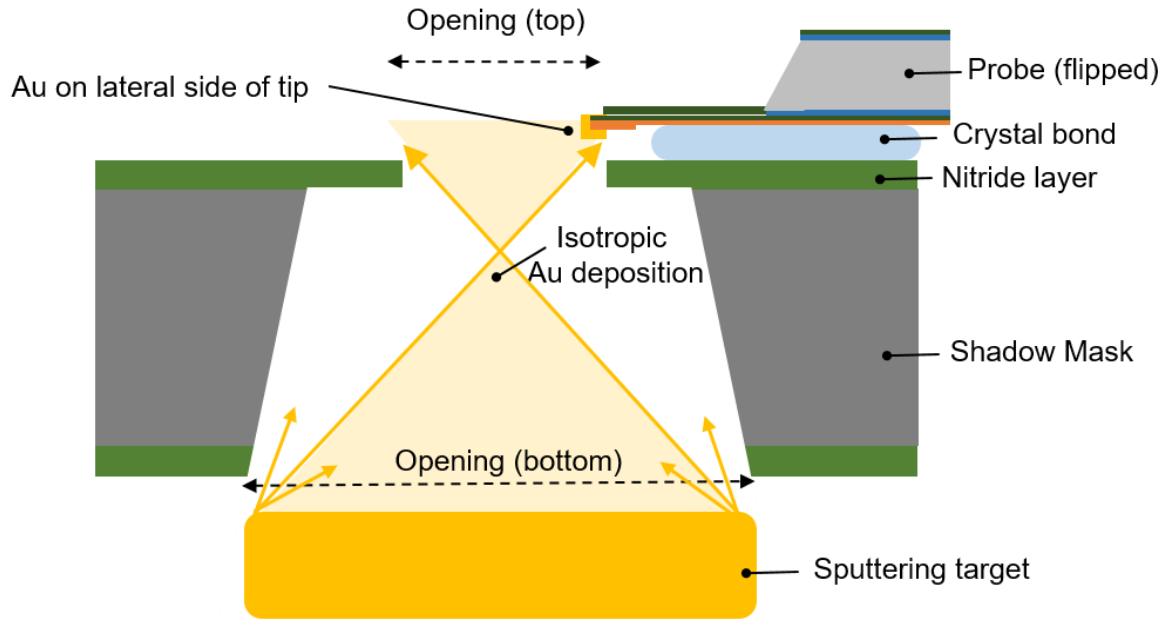

Figure 2.5 Schematics of sputtering for metal coating on the lateral side of a tip.
The yellow arrows denote the sputtering directions. Note that Au is deposited on the lateral side of the tip due to isotropic characteristic of the sputter.

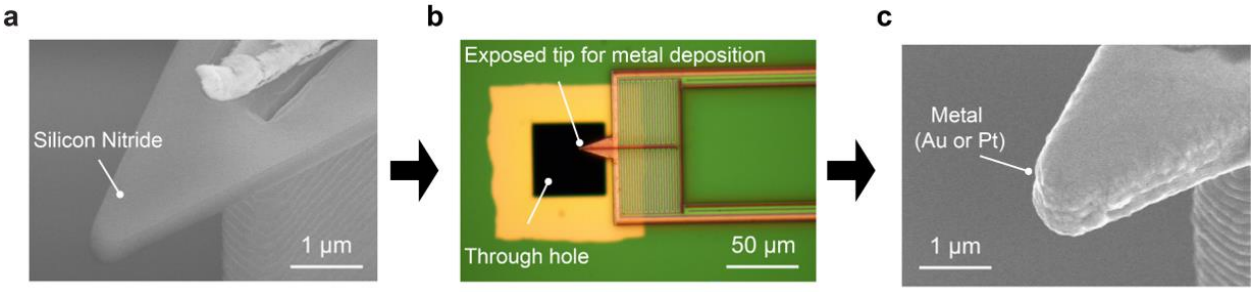

Figure 2.6 Metal addition on the side of probes.
(a) Probes right after a bulk release. (b) A probe is flipped and aligned on the shadow mask. Note that tip end must be exposed to the through-hole and Pt resistive sensors should be protected to avoid electrical shorting. (c) After sputtering, metal is added on the probe both on the top and on the side.

Step 9)

The probe is detached from the second shadow mask and the residual crystal bond removed by piranha cleaning. It should be noted that holding the probe during wet cleaning with typical

tweezers is difficult and the probe can be easily dropped. Therefore, we used a reverse action tweezer which holds the probe without applying pressure to the tweezers. Subsequently, the metal addition is verified on the lateral side of the tip under SEM and electrical resistance under a probe station. If metals (Au or Pt) are coated on the lateral side and electrical resistances are a reasonable range (~20 kΩ for a heater, ~0.5 kΩ for a tunneling electrode), the probe is ready to be used for experiments. The probes shown in Figure 2.7 are the complete version for experiments.

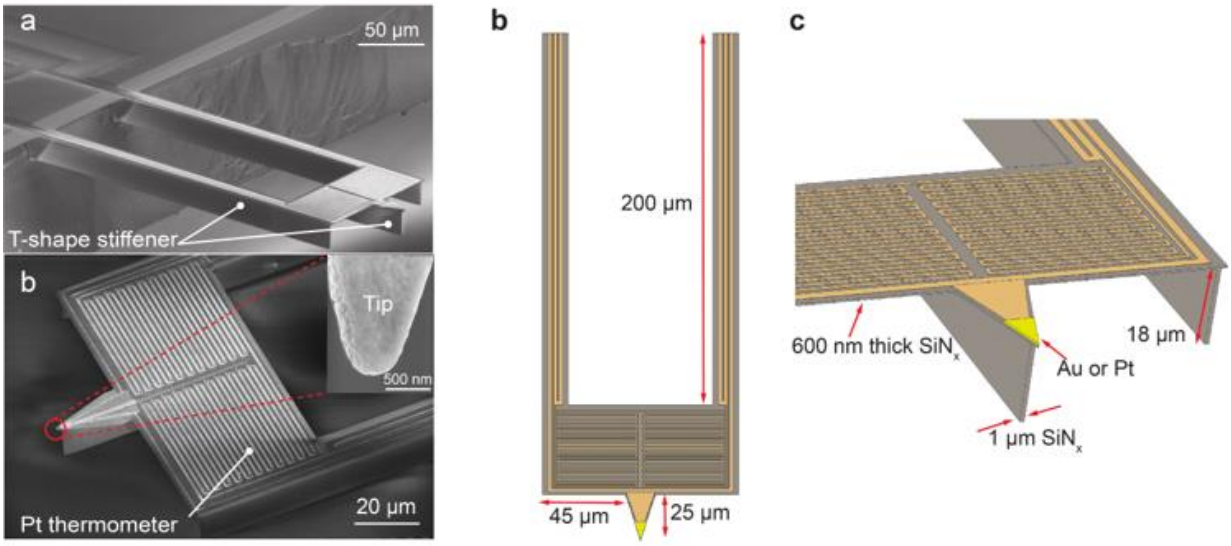

Figure 2.7 Probe images and geometries.
(a) SEM image (side view) of a scanning probe with two long and stiff T-shaped SiN_x beams. (**b**) SEM image (top view) of the scanning probe, featuring an Au-coated tip (inset) and a serpentine Pt thermometer. (c, d) Drawings show the geometry of the fabricated probe and relevant dimensions.

2.4 Characterization of thermal, electrical, and mechanical properties of probes

Characteristics of the scanning probes, including temperature coefficient of resistance of the embedded Pt resistance thermometer, thermal time constant, thermal conductance, as well as the mechanical stiffness of the probe, are crucial to measuring heat transport in single-molecule junctions quantitatively. To gain knowledge of these properties, we employed both experimental techniques and simulation methods. We achieved large thermal resistance by incorporating long, T-shaped beams with a small cross-sectional area, which also enable a very high stiffness (> 10^4 N/m in the normal direction). Both of these features are critical for accomplishing atomic junction thermal measurements. The C-SThM probes also have a sharp metallic tip that we coated with Au or Pt, but which can also be coated with other metals. The experimental characterizations were performed in a high-vacuum (< 10^{-6} Torr) environment, as described below.

2.4.1 Temperature coefficient of resistance (TCR) of the thermometer

The TCR of the Pt resistance thermometer is defined as $\alpha(T) = [R(T+\Delta T)/R(T)-1]/\Delta T$, where $R(T)$ is the temperature-dependent electric resistance and ΔT is the temperature change. To measure the TCR, a small alternating current of amplitude I_f = 1 nA at frequency f = 200 Hz was supplied to the embedded Pt serpentine line on the probe, and the resultant 1f component of the voltage signal, V_f, was measured using a lock-in amplifier (SR830) in a four-probe configuration. The temperature-dependent electric resistance defined as $R(T) = V_f/I_f$ was evaluated by varying the temperature of the probe inside a cryostat (Janis ST-100). A representative plot of the measured resistance of a scanning thermal probe as a function of temperature is shown in Figure 2.8(a). The TCR can be obtained by using the slope of the best-linear-fit curve of the measured data points. This TCR value is lower than the typical bulk Pt TCR which is about 2.5×10^{-3} K^{-1}. Since the

product of TCR and resistivity is constant, increased electrical resistivity results in lower TCR values in thin films than in the bulk material. This is due to non-isotropic diffusive transport caused by phonons, impurities, defects, and grain boundaries[88]. Figure 2.8(a) shows that the TCR was found to be $(1.45 \pm 0.01)\times10^{-3}$ K^{-1} at room temperature.

2.4.2 Thermal conductance of the probe

In order to characterize the thermal conductance of the probe, we applied a sinusoidal electrical current with fixed frequency f and varying amplitude I_f to the embedded Pt serpentine line. The modulated heating power imparted on the suspended island can be calculated as $Q_{2f} = I_f^2 R/2$, resulting in a corresponding temperature increase ΔT_{2f} of the island. Since the thermal time constant (τ) of the probe is ~25 msec, the heating frequency $2f$ was chosen to be 1 Hz to ensure a full thermal response of the device. Similar to the characterization of the thermal time constant, ΔT_{2f} can be quantified by recording the $3f$ component of the output voltage across the Pt line. Figure 2.8(c) displays the relationship between the amplitude of the measured temperature increase ΔT_{2f} and the input heating power Q_{2f}. The thermal conductance of the probe can then be obtained via $G_{th,P} = Q_{2f}/\Delta T_{2f}$, which is estimated to be about 800 nW/K. This thermal conductance can be translated to thermal resistance ($G_{th,p} = 1/R_{th,p}$), which is 1.34×10^6 K/W in Figure 2.8(c).

2.4.3 Thermal time constant of the probe

The thermal time constant indicates the time required for a sensor to respond to a change in temperature. When the sensor temperature increases from T_1 to T_2, the relationship between the time elapsed during the temperature change t, and the temperature T can be written as:

$$T = (T_2 - T_1)\left(1 - e^{-\frac{t}{\tau}}\right) + T_1 \tag{2.4}$$

where $t = \tau$ represents an elapsed time to reach 63% of total temperature change (T_2-T_1).

A short (smaller) thermal time constant is preferred because the probe can resolve the thermal signal within a short time. The thermal time constant is dependent on the thermal capacity of the probe. When the thermal capacity (C_{Th}) is large, the thermal time constant is increased. Our microfabricated probe mitigates this issue because the size of the probe is small (40 μm wide, 80 μm long, and 0.5 μm thickness).

The thermal time constant of the calorimetric scanning thermal probes was determined by applying a sinusoidal electrical current with constant amplitude I_f (I_f = 5 μA) and at varying frequency f to the Pt resistor. This current enables sinusoidal Joule heating of the suspended island, Q_{2f}, with an associated temperature fluctuation at $2f$ with an amplitude of ΔT_{2f}. The $3f$ component of the output voltage across the Pt resistor V_{3f} was recorded using a lock-in amplifier (SRS 830). ΔT_{2f} can subsequently be determined according to the relation $\Delta T_{2f} = 2V_{3f}/(\alpha I_f R)$, where α is the measured TCR and R is the electrical resistance of the Pt serpentine line. The measured ΔT_{2f} , which was normalized by the amplitude at the lowest frequency, is shown as a function of the heating frequency in Figure 2.8(b). Note that the -3 dB point (thermal cut-off frequency) is ~7 Hz. Therefore, the thermal time constant (τ) of the C-SThM probe, which to an excellent approximation is a first-order system, is given by $\tau = (2\pi f_{-3dB})^{-1}$, or ~25 msec. This means that the temperature of the probe can reach 63% of the total amount of increased/decreased temperature within 25 msec so that it can quickly catch added thermal pathways such as thermal conductance along At/Pt atomic junctions or molecular chain.

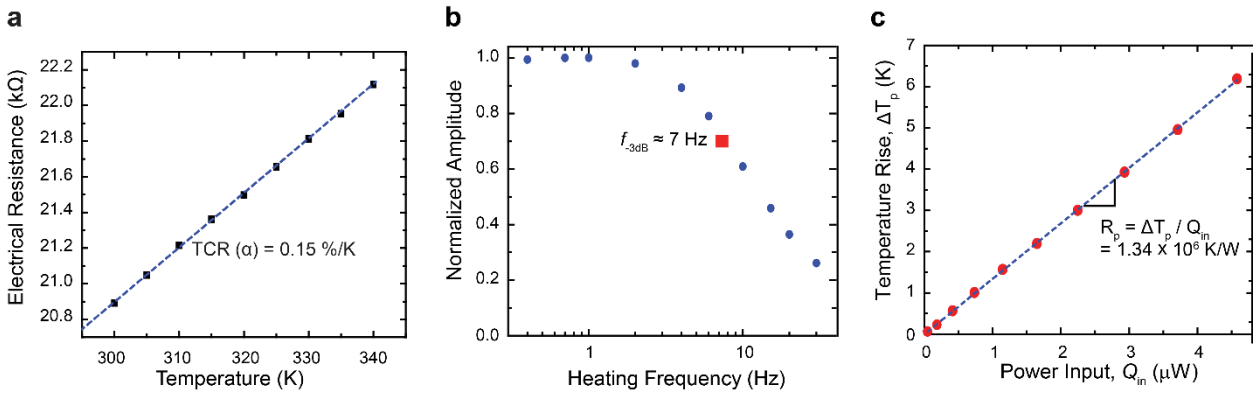

Figure 2.8 Characterization of thermal properties of the C-SThM probe.
(a) Measured electrical resistance of the Pt heater-thermometer as a function of temperature. (b) Normalized temperature rise of the probe as a function of frequency of heat input. The -3dB point is marked by a red square. (c) Temperature rise of the Pt resistance thermometer as a function of the heat input.

2.4.4 Noise characterization of the Pt resistance thermometer

The temperature resolution of the integrated Pt resistance thermometer was evaluated following the protocols developed by our group in the past[87]. Briefly, our temperature measurement employs a modulated electrical current at 1 kHz to measure unmodulated temperature changes in a bandwidth of 10 Hz. Given this scheme, the noise in the measurement has contributions from electronics (amplifiers), Johnson noise, shot noise and ambient temperature drift. We quantified these components and estimated the noise equivalent temperature (NET) of our current thermometry scheme to be ~0.6 mK RMS in a 10 Hz bandwidth.

2.4.5 Mechanical Stiffness of the probe

We note that a high stiffness is desirable for stable trapping of atomic or molecular junctions. We introduced a T-shaped cantilever to enable high stiffness while maintaining low thermal conductance.

In order to estimate the stiffness of the C-SThM probes, we performed finite element analysis (FEA) simulations using COMSOL™ (Solid Mechanics Module), which accurately

predicts device stiffnesses[89]. In performing these calculations, we applied fixed boundary conditions to the distal ends of the beams of the C-SThM probe as shown in Fig. 2.9 (a). The values of Young's modulus and Poisson's ratio of SiN_x were taken to be 290 GPa and 0.20 respectively[90]. To estimate the stiffness of the probe, a 100 nN force was applied either in the normal or longitudinal directions of the cantilever at the end of the probe tip (see Figures 2.9(d), (e) and (f)). The resultant displacement field, as computed by the FEA, enabled us to accurately estimate the stiffness of the probe. From the computed deflections, the stiffness of the probe was estimated to be ~12,500 N/m in the longitudinal direction and ~250 N/m and 9.1 N/m for normal directions. From our experiments, we found that these stiffness values were sufficiently large to ensure stable atomic junction formation. We note that substantially lower stiffness can severely compromise the junction stability due to thermal fluctuation induced deflections of the probes and due to elastic instabilities.

2.4.6 Temperature distribution of the probe

To confirm uniform temperature distribution on the probe, finite element analysis (FEA) simulations using COMSOL™ (Solid Heat Transfer Module) were employed to analyze the temperature distribution within the probe when a heat flux is applied at the tip. We note that, upon heating, the Pt thermometer island exhibits a uniform temperature distribution and the temperature drop occurs primarily along the beams as illustrated in Figure 2.9(a). This ensures that the temperature reported by the Pt resistance thermometer can be used to accurately estimate the heat flow into the probe.

The second question of importance is whether the sinusoidal electric current supplied to the Pt resistance thermometer causes deflections of the probe due to bimaterial effects. To answer this question we first employed the FEM simulations using COMSOL™ (Solid Heat Transfer and

Solid Mechanics Module) to compute the deflection of the probe when a direct electric current is supplied into the Pt thermometer resulting in a 1 K temperature rise of the suspended region. In Figure 2.9(c), our results show that the tip deflection is ~1.9 nm/K. In order to estimate the perturbations due to our sinusoidal electric currents (10 μA, f_s = 1 kHz) supplied into the Pt line, we estimate the temperature oscillations of the probe at 2 kHz (note that Joule heating occurs at twice the excitation frequency, $2f_s$) by noting that our probe behaves as a first-order system (see Figure 2.8(b)). Specifically, to estimate $\Delta T(2f_s)$ we use the expression $\Delta T(2f_s) \approx \Delta T_{DC} \times f_{-3dB}/(2f_s)$, where ΔT_{DC} (=3.25 K) is the temperature increase of the suspended device when a direct current of 10 μA is supplied to the probe, and f_{-3dB} is the cut-off frequency of our scanning probe (~7 Hz). From this analysis, we estimate the temperature rise at 2 kHz to be 11.4 mK. Thus the amplitude of fluctuations of the probe due to bimaterial effects is ~20 pm ($11.4\ \text{mk} \times 1.9\ \text{nm/K}$). Since this amplitude is much smaller than the lengths over which the atomic junctions are stretched, they do not have any adverse effects on our measurements.

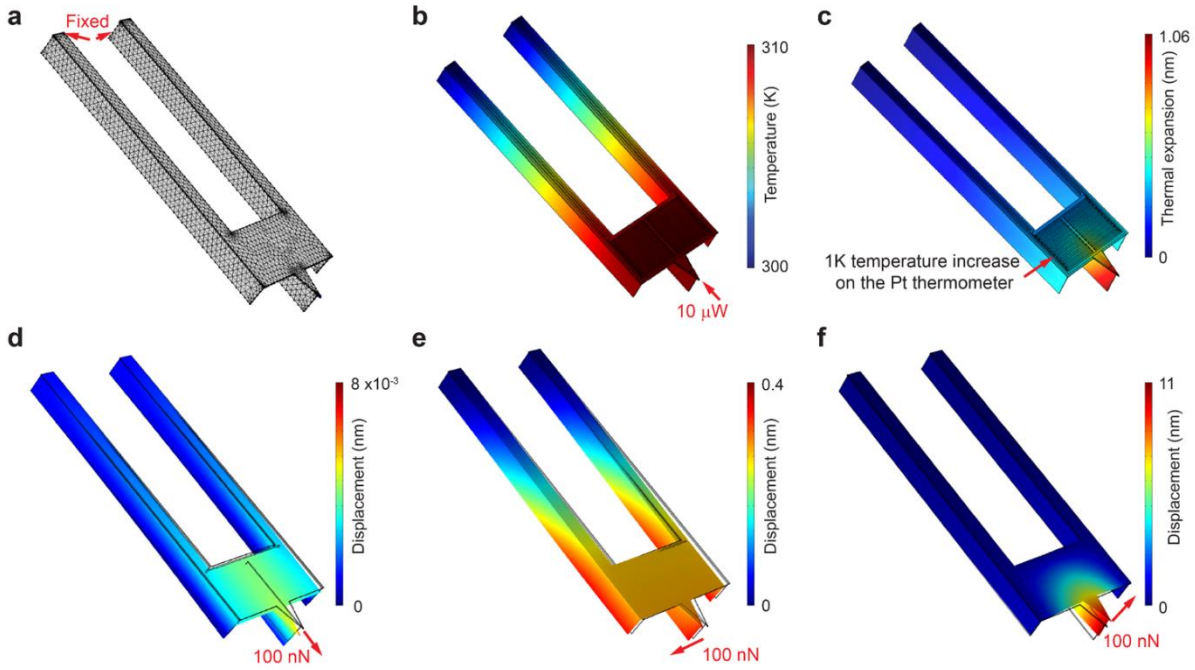

Figure 2.9 Finite element analysis of the mechanical and thermal properties of the probes.
(a) The mesh used in our FEM scheme for the computation of the stiffness. (b) Computed results for the temperature increase of the probe when power input of 10 μW is applied to the Au tip end. It can be seen that the majority of the temperature drops along the beams. (c) Deflection of the C-SThM probe, due to bimaterial effects, when the suspended region of the C-SThM probe was heated by 1 K (DC heating) (d–f) A 100 nN force was applied in normal and longitudinal directions of the cantilever, and the deflection for each of the cases was computed. From the calculations the stiffness of the probe was estimated to be 12,500 N/m (d), 250 N/m (e) and 9.1 N/m (f), respectively.

2.5 Experimental setups

This probe enables us to measure 1) the thermal conductance of metallic wires down to single-atom limit and 2) thermal conductance of a single molecular chain. The experimental setups for single molecular measurement and atomic junction are similar so both of them are described in this chapter. At this point, I would like to acknowledge that *Longji Cui*, my collaborator, conducted most parts of experiments with the C-SThM probes.

2.5.1 Experimental settings for single atomic junctions measurement

In this work, we present a novel experimental platform that allows us to measure the thermal conductance of metallic wires down to the single-atom limit. With this technique, we were able to observe for the first time quantized thermal transport at room temperature. Probing thermal transport in atomic junctions is challenging due to technical obstacles in reproducibly creating stable atomic junctions while measuring minute heat currents flowing through the atomic chains. To overcome these challenges, we developed a novel experimental platform called calorimetric scanning thermal microscopy (C-SThM; Fig. 2.10(a)). Briefly, C-SThM is a custom-fabricated scanning probe that features high temperature resolution (δT_{min} ~1 mK, in a 100 Hz bandwidth, see supplementary material (SM)) Pt thermometers[42,87] and a very large thermal resistance (R_P ~1.3 MW/K) enabling thermal conductance measurements with ~25 pW/K resolution, when a temperature bias of ~20 K is applied across atomic junctions (see SM). The excellent thermal resistance is achieved by incorporating long "T" shaped beams and a small cross-sectional area, which also enables high stiffness (>100 N/m, see SM for further information on the fabrication of the devices). Both these features are critical for accomplishing challenging atomic junction thermal measurements. The C-SThM probes also feature a sharp metallic tip that can be coated with the desired metal (Au or Pt in this study) by using a shadow mask.

Our strategy for quantitatively measuring the thermal conductance of atomic junctions is depicted in Figure 2.10(a) and (b). The Au substrate is heated to an elevated temperature T_S = 315 K, while the probe is connected to a thermal reservoir at a temperature T_P = 295 K. To perform our experiments, the probe was displaced towards the heated substrate by piezoelectric actuation until an electrical conductance of $5G_0$, was reached, with $G_0 = 2e^2/h \approx (12.9\ \mathrm{K\Omega})^{-1}$ being the electrical conductance quantum. This large electrical conductance signals the formation of a Au-Au contact involving several atoms as established by past work [26]. The probe to substrate electrical conductance was measured by applying a small sinusoidal voltage bias of amplitude 1 mV at a frequency of 10 kHz and recording the amplitude of the resultant electric current via a lock-in amplifier. Once the threshold conductance was reached, the probe was withdrawn slowly from the substrate at a rate of 0.05 nm/s. During this process, the probe-substrate contact region is expected to become more constricted until at last a single-atom wide junction is formed, which is broken upon further withdrawal (Fig. 2. 10 (b)) [75]. Thermal conductance measurements were concurrently performed by continuously measuring the change in probe temperature (ΔT_P) in response to heat flow (Q) through the atomic junction. The probe temperature was measured by monitoring the change in the resistance of the embedded Pt resistance thermometer by supplying a sinusoidal electrical current of fixed amplitude (10 μA) and frequency (1 kHz) into the probe while measuring the voltage drop across the resistor.

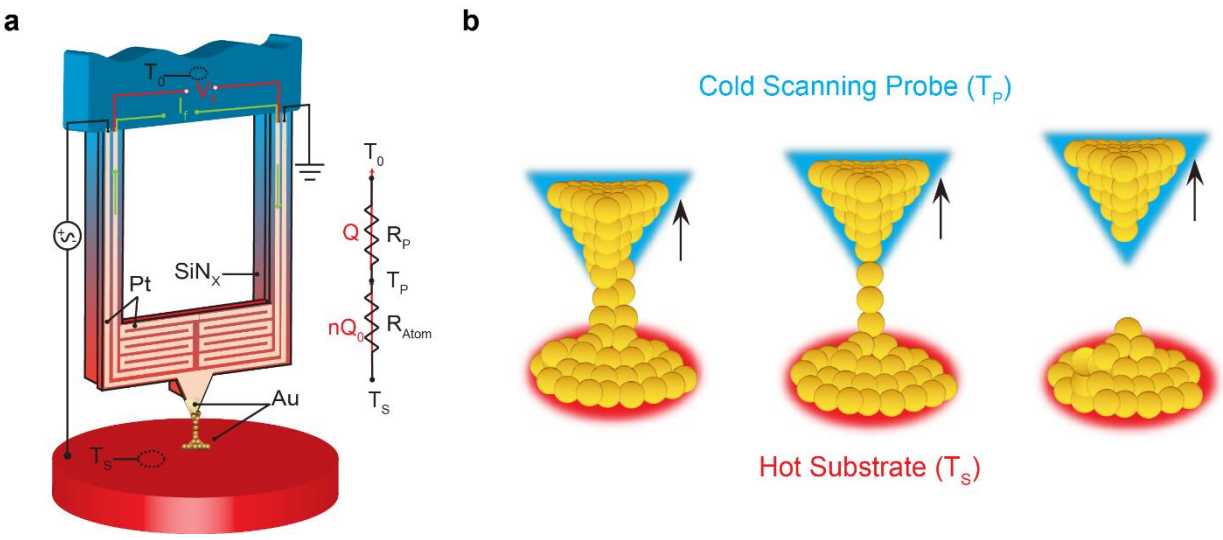

Figure 2.10 Experimental setup of the scanning thermal probes.
(a) Schematic of a calorimetric scanning thermal microscopy (C-SThM) probe, which is used to make atomic junctions with a heated metallic substrate. The tip and substrate coatings can be either Au or Pt. The electrical conductance of the tip-substrate junction is monitored by applying a small sinusoidal voltage bias and measuring the resultant current. The resistance of the Pt resistance thermometer is monitored by applying a sinusoidal current (amplitude I_f) and recording the voltage output (V_f). A thermal resistance network describes the resistances of the atomic chain [$R_{Atom} = (G_{Th})^{-1}$] and the scanning probe (R_P), as well as the heat current flow (Q, red arrow). The substrate, thermal reservoir, and tip temperatures are indicated fby T_S, T_0, and T_P, respectively. (b) Schematics of the atomic chains forming, narrowing, and breaking during the withdrawal of the probe from the heated substrate.

2.5.2 Experimental settings for single molecule measurement

The experimental setup and the basic strategy for quantifying thermal conductance at the single-molecule level are depicted in Figure 2.11. The C-SThM probe, located in an ultra-high vacuum (UHV) environment, is heated up to a temperature, T_P, above ambient, typically T_P = 320 – 340 K, by supplying a constant electric current (~30 – 40 μA) to the Pt serpentine resistor, while the Au substrate (also in an UHV environment) is connected to a thermal reservoir maintained at ambient room temperature T_S = 295 K. The planar surface of the Au substrate is coated with a self-assembled monolayer of molecules to facilitate formation of single-molecule junctions between the Au-coated tip of the scanning probe and the substrate. In this work, we choose prototypical thiol-terminated alkane molecules to perform experiments of heat transport through single-

molecule junctions as they are widely regarded as a model system and have been extensively explored computationally[28,30]. We first create molecular junctions by displacing the scanning probe at a constant speed via piezoelectric actuation towards the Au substrate until contact is made between the two Au electrodes, as signaled by a large, predictable increase in the electrical conductance which is recorded by applying a voltage bias between the Au tip and the substrate. Subsequently, the probe is withdrawn slowly from the substrate at a speed of 0.05 nm/s. During this process, the molecules trapped between the tip of the scanning probe and the Au-substrate break away from either the substrate or the tip until the last molecular junction is broken. During the tip withdrawal from the substrate, we continuously monitor both the electrical current through the junction for a fixed voltage bias and the temperature of the probe. As described in more detail below, the measured electrical currents enable us to determine the electrical conductance and identify single molecular conduction events, while the measured temperature change of the probe (ΔT_P) allows analysis of the thermal conductance of single molecule junctions ($G_{th,SMJ}$).

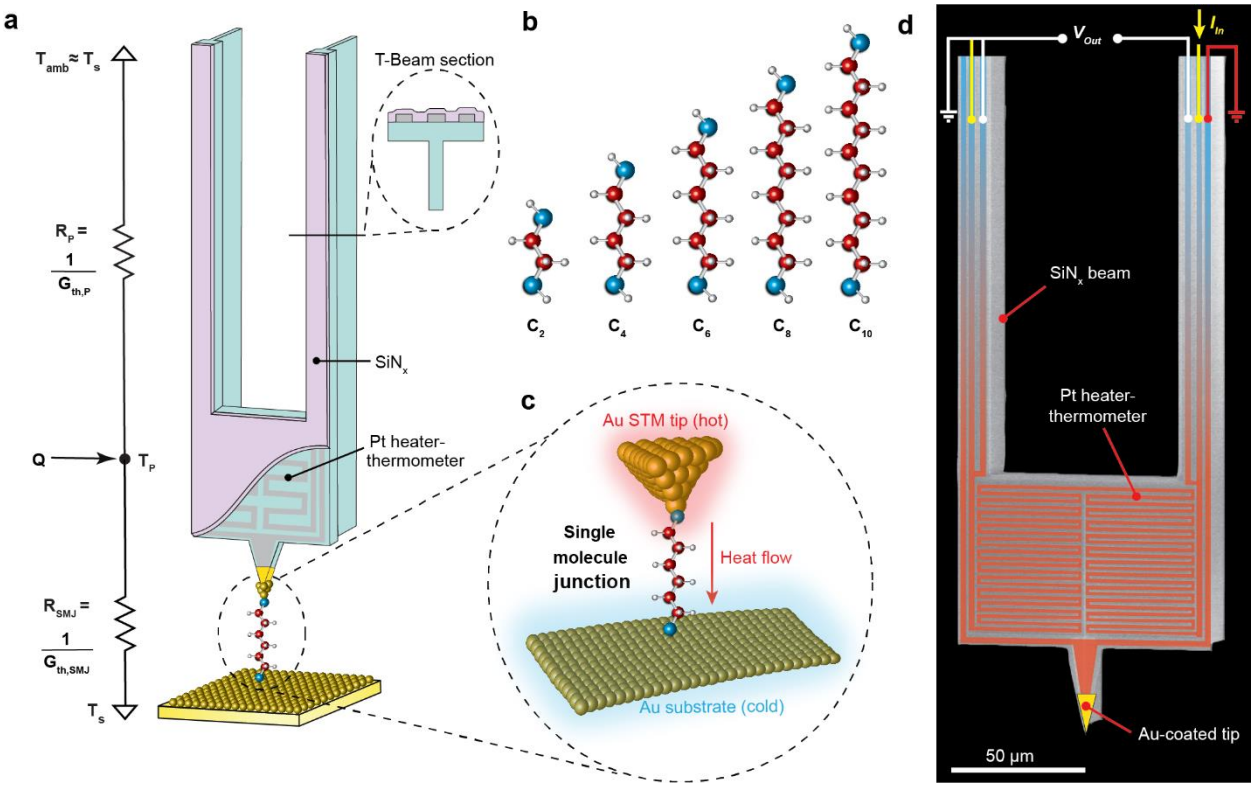

Figure 2.11 Experimental set-up and strategy for quantifying heat transport in single-molecule junctions. (a) Schematic of the calorimetric scanning thermal microscopy (C-SThM) set-up. Right, a single molecule is trapped between an Au-coated tip of the C-SThM probe, which features 'T'-shaped silicon nitride (SiN_x) beams and is heated to temperature T_P by input of a heat current (Q) via an embedded serpentine Pt heater-thermometer, and an Au substrate at temperature T_S that is equal to ambient temperature (T_{amb}). The thermal conductance of single-molecule junctions is quantified by recording the temperature change of the Pt heater-thermometer when a single-molecule junction is broken. Left, resistance network capturing the thermal resistances of the molecular junction ($R_{SMJ} = 1/G_{th,SMJ}$) and the scanning probe ($R_P = 1/G_{th,P}$). (b) Schematics of the alkanedithiol molecules (Cn) studied in this work; n = 2, 4, 6, 8, 10 denotes the number of carbon atoms in the molecules (red, carbon atom; grey, hydrogen atom; blue, sulfur atom). (c) Magnified view of ringed area in a, describing the trapping of a single C6 molecule between the heated Au STM tip and the cold Au substrate. (d) Scanning electron microscope image (false colored to highlight the Pt heater-thermometer) of a custom-fabricated C-SThM probe (which shows the tip end), featuring two long 'T'-shaped SiN_x beams (see beam cross-section shown ringed in a) and a serpentine Pt heater-thermometer integrated on a suspended micro-island. The electrical resistance of the Pt heater-thermometer is monitored by measuring the voltage output (V_{out}) in the presence of an input d.c. current (I_{in}).

2.5.3 Ultra-low Noise Measurement Environment

All measurements in this experiment were performed in the ultra-high vacuum (~10^{-9} Torr) scanning probe microscope (RHK UHV 750). The instrument was housed inside an ultra-low noise facility where the ground vibrations were attenuated to meet the requirement of NIST-A standard.

Temperature drift in the room where the scanning probe microscope is located was actively controlled to be within <100 mK around the set-point temperature (295 K).

2.5.4 Sample preparation and surface cleaning protocols

Employing proper surface cleaning protocols is essential for successfully eliminating any contamination on the surfaces that compromise the desired thermal measurements. Towards this goal, we developed protocols for sample preparation and for cleaning the surfaces of the scanning probe and the substrate sample.

In quantized thermal conductance in atomic junctions measurement, planar Au and Pt samples were prepared by employing a template stripping approach. Briefly, a 150 nm thick layer of Au/Pt was deposited using E-beam evaporation on a pristine Si wafer. Subsequently, a low-viscosity epoxy (Epotek 377) was applied uniformly on the metal-coated Si wafer to glue a clean 7 mm × 7 mm Pyrex piece to the top surface of the wafer. The wafer was cured at ~150 °C for two hours. Right before the experiment, the Pyrex substrate was peeled off to successfully expose a pristine Au/Pt sample, which is protected from oxidation by the Si substrate. The peeling off process is conducted in a pure N_2 filled glove box, minimizing the exposure of the clean surface to the ambient environment.

In single molecule thermal conductance measurement, to facilitate the formation of single-molecule junctions during the experiments, self-assembled monolayers of alkanedithiol molecules were prepared on a planar Au-coated substrate. A template-stripping approach was applied to prepare the Au substrates. Briefly, a 150 nm-thick Au film was first deposited on a clean Si wafer via e-beam evaporation. 7 mm-by-7 mm Pyrex pieces were then glued on the Au-coated silicon wafer using a low viscosity epoxy (EPOTEK 377) before curing the wafer (150 °C for 2 hours). Right before the molecular sample preparation, the Pyrex pieces were cleaved from the silicon

wafer to expose the pristine Au sample, and the Pyrex pieces were immediately immersed in 500 μM ethanol solutions of alkanedithiol molecules (C2, C4, C6, C8, C10 from Sigma Aldrich with purity >95%) to initiate the self-assembly process of the molecules on the Au surface. After ~12 hours of incubation, the samples were thoroughly rinsed in ethanol and dried in a nitrogen atmosphere before being transferred into the ultra-high vacuum measurement environment. We note that the whole preparation process was conducted in a nitrogen gas-filled glove box to minimize the potential contamination from ambient and other sources.

The above-described approach cannot be applied to the metal at the tips of the C-SThM probes. In order to ensure high cleanliness of the Au-coated scanning thermal probes, which is critical to successfully perform thermal transport measurements at the atomic and molecular scale[91], the following protocol was developed. After releasing the probe from the shadow mask as described in the nanofabrication process, the probes were first sonicated in acetone, IPA and then DI water, with each step continuing for ~10 mins. Subsequently, the probe was dried in N_2 and subjected to oxygen plasma cleaning cycles (300 W, 5 mins). For Pt coated scanning probes, additional hydrogen plasma cleaning cycles (50 W, 20 mins) were applied after oxygen plasma treatment. All cleaned probes and samples were always placed in a N_2 gas environment to avoid direct contact with the ambient. Successful experiments were accomplished when the apparent tunneling barriers measured in the experiments[91,92] were large (>2 eV).

2.5.5 Electrical conductance measurements

The electrical conductance of single atomic junctions (SAJs) is measured by supplying a small sinusoidal electric voltage of 1mV at 10 kHz across the scanning probe and the substrate, and monitoring the amplitude of the resultant current by using a current amplifier and a lock-in amplifier (SRS 810).

The electrical conductance of the single molecular junctions (SMJs) was also measured by supplying a d.c. voltage bias (30 mV, 50 mV, 100 mV, 100 mV, 200 mV, for C2-C10 junctions, respectively) across the scanning thermal probe and the Au substrate, while monitoring the tunneling current across the junctions via a current amplifier (SR570). Smaller voltage biases were chosen for shorter molecular junctions, which feature larger electrical conductances, to minimize the effects of Joule heating. In spite of the use of a smaller bias, Joule heating has significant contributions to C2 and C4 junctions and to a smaller degree for C6 junctions and is systematically accounted for in all SMJs.

All the SAJs and SMJs were created between the Au-coated scanning thermal probe and the metal/molecule-covered Au substrate. During the measurement, the scanning probe was controllably displaced towards the substrate at 1 nm/s using a piezoelectric actuator, and withdrawn from the substrate at 0.05 nm/s after making contact as indicated by a recorded, sufficiently large electrical conductance (compared to the SAJs or SMJs electrical conductance). The withdrawal of the scanning probe was stopped once SAJ or SMJ was formed, as indicated by an approximately constant electrical conductance corresponding to within one standard deviation of the SAJ conductance or SMJ conductance obtained from the conductance histogram. Simultaneous electrical and thermal conductance measurements were performed for a constant electrode separation (drift <1 Å/min) until the particular SAJ or SMJ spontaneously broke. The process of formation and breakdown of SAJ or SMJ was repeated several ten to hundred times for each type of metal or molecule.

In order to study the thermal conductance of the junctions, the temperature change of the scanning thermal probe was measured before and after the breakdown of the SAJs or SMJs. For this purpose, we monitored the change in the electric resistance of the embedded Pt resistance

thermometer via a half-Wheatstone bridge. The output voltage signal of the bridge circuit in the presence of a d.c. electric current was first amplified by an instrumentation amplifier (AD524) with a gain of 100 and subsequently measured using a low-noise voltage amplifier (SR 560 with a gain of 100).

2.5.6 Electrical circuitry and identification of thermal conductance

In order to study the thermal conductance of the junctions, the temperature change of the scanning thermal probe was measured before and after the breakdown of the SAJs or SMJs.

The thermal conductance measurement is enabled by recording the temperature change of the scanning probe. This is accomplished by monitoring the changes in the electrical resistance of the Pt serpentine line (Pt-thermometer). To accomplish this goal the Pt sensor forms part of a half Wheatstone bridge whose output signal was amplified by an instrumentation amplifier (AD524) with a gain of 100. The amplified signal was measured using a low-noise voltage amplifier (SR 560 with a gain of 100)

To analyze the thermal conductance of single-molecule junctions, we identify single-molecule events via off-line analysis from our continuous recordings by applying the following criteria: 1) The electrical conductance trace drops in a clear last step from a constant, expected electrical conductance value (corresponding to the previously established values, see above), signaling the presence of a single-molecule junction prior to break down. 2) During formation and following break down of the junction, the thermal conductance from the probe to the monolayer sample is relatively stable (drift <100 pW/K in 0.5 s), signifying a thermal measurement that is not compromised by the presence of background conduction pathways. The second criterion is principally informed by our group's published work[91], which suggests that the presence of organic

contamination leads to parasitic conductances. Rigorous application of the above criteria avoids artifacts and ensures reliable single-molecule thermal conductance measurements.

2.5.7 Noise reduction with a time-averaging scheme

The measured temperature change of the scanning thermal probe is associated with substantial noise contributions from electronics (amplifiers), Johnson noise, shot noise and temperature drift of the measurement environment. As shown in Figure 2.14 (b), the unprocessed thermal signals are featureless and buried in large noise (~100 pW K^{-1}). This noise level is affordable to measure the quantized thermal conductance of single atomic junctions. However, it is not sufficient to measure single molecule thermal conductance.

To improve the signal-to-noise ratio of the measurements, a time-averaging scheme is applied to the thermal conductance traces, which were acquired through independent measurements of many molecular junctions (~100). Briefly, the time at which a single-molecule junction breaks (t_b) was first detected by analyzing the time series of electrical conductance traces. Subsequently the ΔG_{th} signal corresponding to the same electrical conductance trace was demarcated into a τ = 0.5 s region (shaded in green in Figure 2.14(b), bottom panel) before t_b, and two intervals τ' = 0.1 s (unshaded) and τ = 0.5 s (shaded in brown) after t_b. We note that the τ' = 0.1 s interval (around four times the thermal time constant of the probe) corresponds to the time required to achieve the full thermal response of the probe after the junction-breaking event. Further, the average value of the ΔG_{th} signal in the subsequent 0.5 s after breaking of the molecular junction is averaged and set to zero by suitably offsetting the curve. (This procedure ensures compliance with the physical expectation that the thermal conductance change after breaking of the junction is negligibly small.) Finally, the thermal conductance traces from each of the individual experiments were aligned using t_b as the reference point, and data from corresponding

time points were averaged. Following a procedure described in detail in our previous work[63], we can estimate the smallest thermal conductance change ($\Delta G_{\text{th,min}}$) detectable using our time-averaging scheme to be:

$$\Delta G_{\text{th,min}} \sim \frac{G_{th,P}}{T_P - T_S}\frac{1}{IR_0\alpha}\left\{\int_{-\infty}^{+\infty}\left[G_{noise}(f)\left[\frac{2\tau+\tau'}{\tau}\frac{\sin(2\pi fT)}{2\pi fT}\frac{2\sin[\pi f(\tau+\tau')]\sin[\pi f(\tau+\tau')]}{\sin[\pi f(\tau+\tau')]}\right]^2 df\right]\right\}^{1/2} \quad \textbf{(((2.5)}$$

Here $G_{\text{noise}}(f)$ is the power spectral density at frequency f associated with the temperature noise that the probe is subject to, and $2T$ is the total time over which the averaging is performed. For example, for 100 molecular junctions, the total averaging time $2T$ equals 110 s. By following the protocol that we have developed previously[87] to measure the noise spectrum of a Pt resistance thermometer, we can estimate the power spectral density. With this information and the above equation, we estimate $\Delta G_{\text{th,min}}$ to be ~2 pW K^{-1}.

Finally, we note that the electrical conductance traces show additional stepwise changes before a rupture of the last junction that represents recordings during the withdrawal of the tip from multi-molecule junctions. These additional charges do not yield identifiable multiple conductance states in electrical conductance histograms (see, for example, Figure 2.14 (a)). Further, given the low thermal conductance of the studied molecular junctions, the thermal traces of multi-molecule junctions are, as expected, largely featureless. An averaging approach analogous to the successful analysis of the thermal conductance of single-molecule junctions cannot yield the corresponding thermal conductances of these multiple-molecule junctions, as these states are not well correlated in time and step-size compared to the single-molecule junction states.

2.5.8 Effect of Joule heating on thermal conductance measurements

When a small sinusoidal electric voltage of 1mV at 10 kHz is applied across the scanning probe and the substrate, the small amplitude of the applied bias gives rise to very small amounts of Joule heating in single molecular junctions (~25 pW). This is negligible in comparison to the heat flows through the single molecular junctions, which exceed 10 nW for single molecular junctions (when a 20 K temperature differential is applied as we do in our measurements).

However, we need to account for the heat dissipation that results from the applied electrical bias in single molecular experiments. Specifically, when a voltage bias (V) is supplied across a junction of resistance R, it results in total heat dissipation of V^2/R. Since the Seebeck coefficient of alkanedithiol junctions is very small[93], the heat dissipation in the electrodes is symmetric to an excellent approximation[63]. Therefore, the heat dissipated in the probe due to the voltage bias is given by $V^2/2R$. When the single-molecule junction is broken, the probe not only heats up due to the loss of a thermal conduction pathway, but there is also a competing effect that attenuates the temperature drop as the heat dissipation in the probe decreases by $V^2/2R$. In order to systematically account for this effect, we add $\Delta T_{\text{Joule}} = V^2/(2RG_{\text{th,P}})$ to the measured data in the range 0 to t_b seconds (that is, for the region before the junction is broken) to obtain the ΔT_P plot in Fig. 2.14 (b) and all other related ΔG_{th} plots shown in the manuscript (Figs. 2.12 c,d). These corrections are modest for C6 (~20%), C8 (<2%) and C10 (<2%) junctions, but they are sizable for C2 (~60%) and C4 (~30%) junctions. Here, all the percentages represent how large ΔT_{Joule} is with respect to the observed temperature drop ΔT_P when the junction breaks.

2.6 Results

2.6.1 Results of quantized thermal conductance measurement

From the resistance network of Figure 2.10 (a), we can directly relate the thermal conductance (G_{Th}) of the atomic junctions to ΔT_{P} by $G_{\mathrm{Th}} = \Delta T_P/[R_P(T_S - T_P - \Delta T_P)]$, where R_{P} was experimentally characterized (see Chapter 2.4.2 and Figure 2.8(c)) to be 1.4×10^6 K/W. Representative thermal (red) and electrical conductance (blue) traces recorded while the Au coated scanning probe is withdrawn from a heated Au substrate are shown in Figure 2.12(a). From these representative traces, it is clear that the electrical conductance decreases in discrete steps with some of the curves showing preferential conductance values that occur at integer multiples of G_0 as expected from past work [26]. It can also be seen that the corresponding thermal conductance curves are closely correlated with the electrical conductance curves. Further, several of the thermal conductance curves show steps with preferential conductances at $2\pi^2 {k_B}^2 T/3h$, a value that is twice the quantum of thermal conductance ($G_{0,\,\mathrm{Th}}$). The factor of 2 is a consequence of the spin degeneracy in electron transport and is not present in the usual definition of $G_{0,\mathrm{Th}}$ because it was introduced in the context of phonon transport, where spin degeneracy is absent.

Past studies[94-96] on electrical conductance quantization established that the presence of plateaus in the conductance traces is insufficient evidence of quantization. Definitive conductance quantization requires an unbiased statistical analysis from a large data set. We obtained ~2000 consecutive electrical and thermal conductance traces with the procedure outlined above, which yielded electrical and thermal conductance histograms with clear peaks at $1G_0$ and $2G_{0,\mathrm{Th}}$, respectively in Figure 2.12 (c) and (d). The thermal conductance histogram is broader than its electrical counterpart because the time constant for our thermal measurements (~25 ms) is larger

than that for our electrical measurements (~10 μs). The 2D histogram in Figure 2.12(b) was constructed by collecting the electrical conductance (G_e) and the corresponding Lorenz number (L / L_0) of the four measured electrical and thermal conductance traces shown in Figure 2.12(a) and counting the number of data falling into the joint bins of $[(G_e)_i, (L / L_0)_j]$, where i, j = 1, 2, …, N. In constructing our histograms N was chosen to be sufficiently large (>100, as large as 1000 in some cases) to give results that were invariant with further increasing the value of N. The same procedure was applied to obtain the joint plot of electrical and thermal conductances in Fig. 2E, where we used ~2000 traces of concurrently measured G_e and G_{Th}, without any data selection. These measured traces were also used to obtain 1D histograms of electrical conductance (Figure 2.12(c)) and thermal conductance (Figure 2.12(d)) and the corresponding Lorenz number (Figure 2.12(f)).

The close correlation between the thermal and electrical conductances (Figure 2.12(a)) provides important information regarding the validity of the Wiedemann-Franz law, which relates the electronic contribution of the thermal conductance, $G_{Th,e}$, to the electrical conductance, G_e, by $G_{Th,e} = L_0 T G_e$, where $L_0 = (\pi^2/3)(k_B/e)^2$ is the Lorenz number[97]. Because this basic law was originally derived with semiclassical arguments and is approximately obeyed in macroscopic wires of standard metals[97], it is unclear whether it should remain valid in metallic atomic junctions, where the transport mechanisms are different[98]. To test the validity of the Wiedemann-Franz law in atomic junctions, we used the data in Figure 2.10(a) to obtain the Lorenz ratio, $L/L_0 = G_{Th}/L_0 G_e T$, as a function of G_e. Here, T = 305 K is the average temperature of the tip and the sample. This process was repeated for each set of curves shown in Figure 2.12(a), and the data from all four curves were collected into the two-dimensional (2D) histogram shown in Figure 2.12(b). It is clear from the data that the value of L/L_0 is very close to 1.

We plotted a 3D histogram from 2000 concurrently measured electrical and thermal conductance traces, without any data selection (Figure 2.12(e)). The histogram features a large peak corresponding to (G_0, $2G_{0,\mathrm{Th}}$), showing that the electrical and thermal conductance quantization occurs concurrently and that the quantized state is a statistically favored atomic configuration. This close correlation is also reflected in the 2D histogram (Figure 2.12(f)), where we computed $L/L_0 = G_{\mathrm{Th}}/L_0 G_{\mathrm{e}} T$ = 1.06 as mean value from the 2000 traces. The small increase above 1.00 is primarily due to contributions from phonons to the thermal conductance, which we estimate to add ~5 to 10% (see below). The increase in L/L_0 could also reflect small contributions (~10 to 20 pW/K) from near-field radiative heat transfer[91] and even smaller contributions from the overestimation of the thermal conductance during periods of rapid transition in the electrical conductance, when the thermal response lags the electrical response.

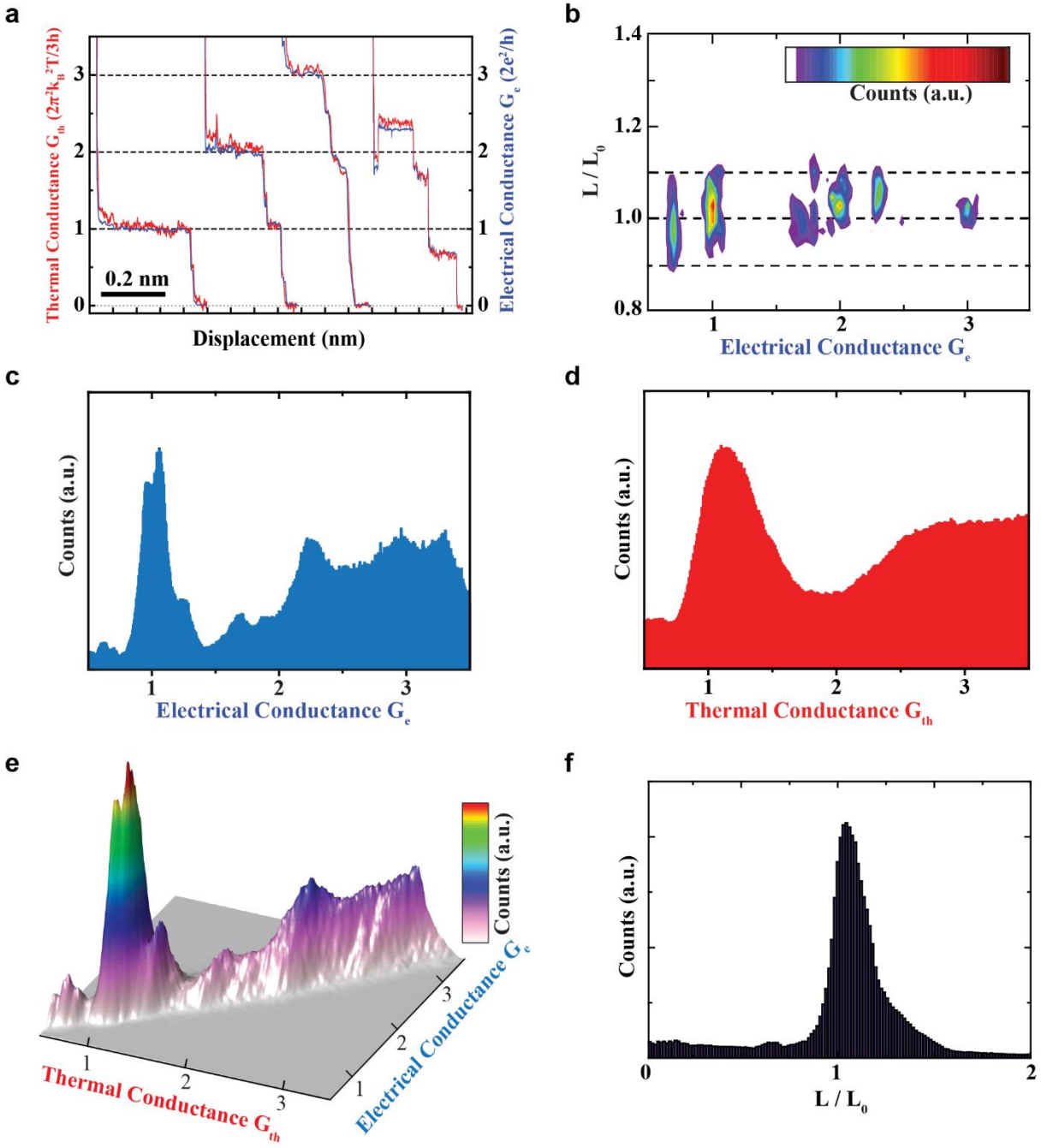

Figure 2.12 Thermal conductance quantization in Au atomic junctions.
(**a**) Representative traces of thermal and electrical conductances measured while reducing the transverse constriction of Au atomic junctions by displacing the Au tip of the C-SThM probe away from the Au substrate. The thermal (red) and electrical (blue) conductance traces are plotted in units of $2\pi^2k_B{}^2T/3h$ ($2G_{0,Th}$, twice the thermal conductance quantum) and $2e^2/h$ (G_0, the electrical conductance quantum), respectively. (**b**) Histogram of the ratio of the thermal conductance to the electrical conductance, showing good agreement with the Lorenz number (L/L_0). The color bar indicates the number of counts, increasing from white to red. (**c** and **d**) Electrical and thermal conductance histograms

obtained from 2000 concurrently measured electrical and thermal conductance traces (without any data selection), similar to those shown in (a). (**e**) A joint plot of the electrical and thermal conductance traces shows the tight correlation between the occurrence of electrical and thermal conductance quantization. (**f**) Analysis of the data in (c) and (d) shows that the Wiedemann-Franz law accurately predicts the thermal conductance of Au atomic junctions (the peak is at 1.06). a.u., arbitrary units.

The observed thermal conductance quantization in Au junctions is a direct consequence of the electronic structure of these junctions, which in turn is also responsible for the validity of the Wiedemann-Franz law. However, the opposite is not true: The validity of the Wiedemann-Franz law is a consequence of the smooth energy dependence of the electronic transmission[99,100], but this does not imply that thermal transport is quantized in all cases. To unambiguously test these predictions, we performed measurements with a Pt-coated scanning probe and a Pt substrate, using the same methodology that we used for Au atom junctions. The histograms obtained from the measured electrical and thermal conductance traces for Pt junction are shown in Figure 2.13(a) and (b). As explained in the manuscript, the histograms for Pt atomic junction, in contrast to histograms for Au atomic junctions, do not show any clear peaks at integral multiples of G_0, $G_{0,Th}$, suggesting that there is no observable thermal conductance quantization for Pt junctions at room temperature. The measured electrical and thermal conductance traces in Figure 2.13(c) show plateaus. Histograms of electrical and thermal conductance traces do not show conductance quantization. However, a histogram-based analysis of 100 Pt traces in Figure 2.13(d) revealed that the Lorenz ratio is very close to 1 and therefore obeys the Wiedemann-Franz law. This demonstrates that thermal conductance quantization is not a universal feature of all metallic systems at room temperature.

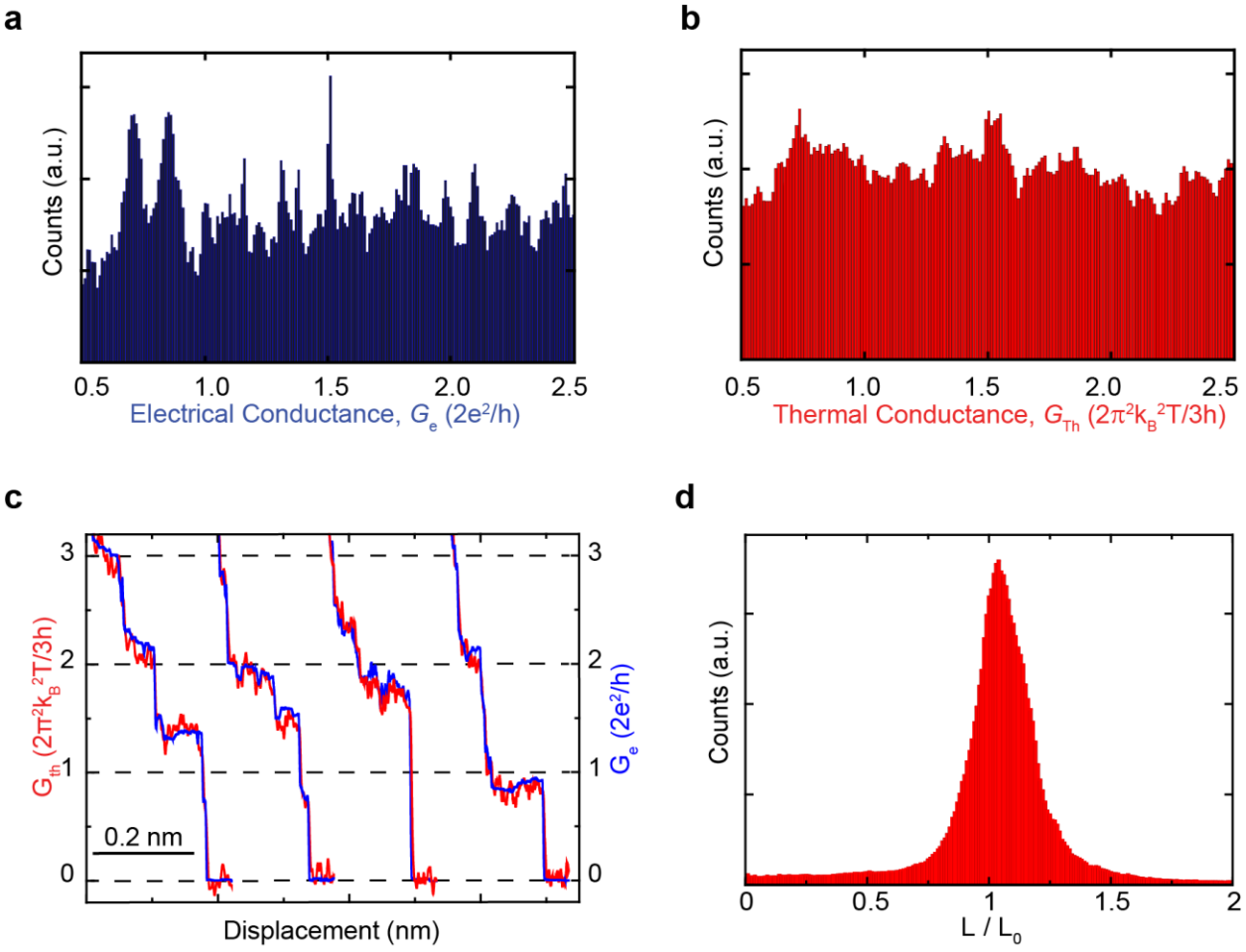

Figure 2.13 Histograms and measured transport properties of Pt atomic junctions.
(a, b) Electrical and thermal conductance histograms for Pt atomic junctions (obtained from experimental data). The histograms are relatively featureless and do not display any distinct conductance quantization. (**c**) Representative measured traces of electrical (blue) and thermal (red) conductances for Pt atomic junctions show discrete steps (conductance histograms do not display electrical or thermal conductance quantization). (**d**) Histogram similar to that shown in Figure 2.10(f) but for Pt data, showing that the Wiedemann-Franz law is applicable (the peak is at 1.04).

2.6.2 Results of single molecule junctions thermal conductance measurement

We first trap molecules of 1,6-hexanedithiol (C6) between the Au-coated tip of the C-SThM probe and the Au substrate. Figure 2.14(a) shows representative electrical conductance–distance traces obtained by repeatedly displacing the tip away from the substrate, and the electrical conductance histogram constructed from about 500 independently measured traces. The histogram features a pronounced conductance peak at about $5.1 \times 10^{-4} G_0$ (electrical conductance

quantum, $G_0 = 2e^2/h \approx 77.5$ μS), indicating the most probable low-bias conductance of a single-molecule junction. This value is interpreted as the electrical conductance of a single C6 molecule bridging the Au electrodes, and is in good agreement with the previous work[101].

To probe the thermal conductance of single-molecule junctions, we stop the tip withdrawal process when the electrical conductance of Au–C6–Au junctions is close to (within one standard deviation around the Gaussian-fitted histogram peak) the most probable low-bias conductance, and monitor the electrical current and temperature of the probe until the molecular junction spontaneously breaks. The top panel in Figure 2.14(b) shows a typical electrical conductance trace measured for an Au–C6–Au single-molecule junction, showing how the electrical conductance suddenly drops within a few milliseconds (the time constant of the electrical measurements) when the molecular junction breaks. As the Joule heating is small for Au–C6–Au junctions (see Chapter 2.5.8) and breaking removes the thermal conduction pathway through the molecular junction, we expect a small temperature rise in the probe (ΔT_P) immediately after the junction is broken. This temperature change can be related to the change in the thermal conductance of the junction (ΔG_{th}), that is, the thermal conductance of a single-molecule junction ($G_{th,SMJ}$), via $G_{th,SMJ} = -\Delta G_{th} \approx G_{th,P}\, \Delta T_P/(T_P - T_S)$ (see Chapter 2.4.2), where $G_{th,P}$ is the thermal conductance of the probe and $T_P - T_S$ is the temperature difference between the probe and the substrate. The bottom panel of Fig. 2.14(b) presents the measured temperature change of the probe (right *y*-axis), from which the thermal conductance, ΔG_{th} (left *y*-axis), can be directly determined. (See Chapter 2.5.8 for a description of how the measured temperature change of the probe is processed and how the effects of Joule heating, which are small in this case but increase for shorter molecules, are systematically accounted for.)

Because the thermal conductance of the Au–C6–Au single-molecule junction is small relative to the noise present in ΔT_P, preventing reliable direct detection of changes in thermal conductance, we applied an averaging scheme to improve the signal-to-noise ratio of the thermal measurements and resolve ΔG_{th}. In brief, we performed many measurements (hundreds) following the protocol described above, and first used the electrical conductance versus time traces to identify the time point t_b when the single-molecule junction breaks (t_b = 0.5 s in Figure 2.14(b)). Using the electrical signal as a reference, thermal signals were then aligned and averaged (see Chapter 2.5.7). As the averages over 20, 50, 100 and 300 traces in Fig. 2.14 (c) illustrate, averaging suppresses noise and reveals a clear thermal conductance change (ΔG_{th}) that coincides with the electrical conductance change caused by the breaking of the single-molecule junction. This approach reveals a change in the conductance of about 18 pW K^{-1}, which represents the thermal conductance of the Au–C6–Au single-molecule junction ($G_{th,SMJ}$). In contrast to the rapid transition of the electrical signal on the breaking of the junction, the roll-off of the thermal conductance is much slower because it is limited by the thermal time constant of the scanning probe (about 25 ms).

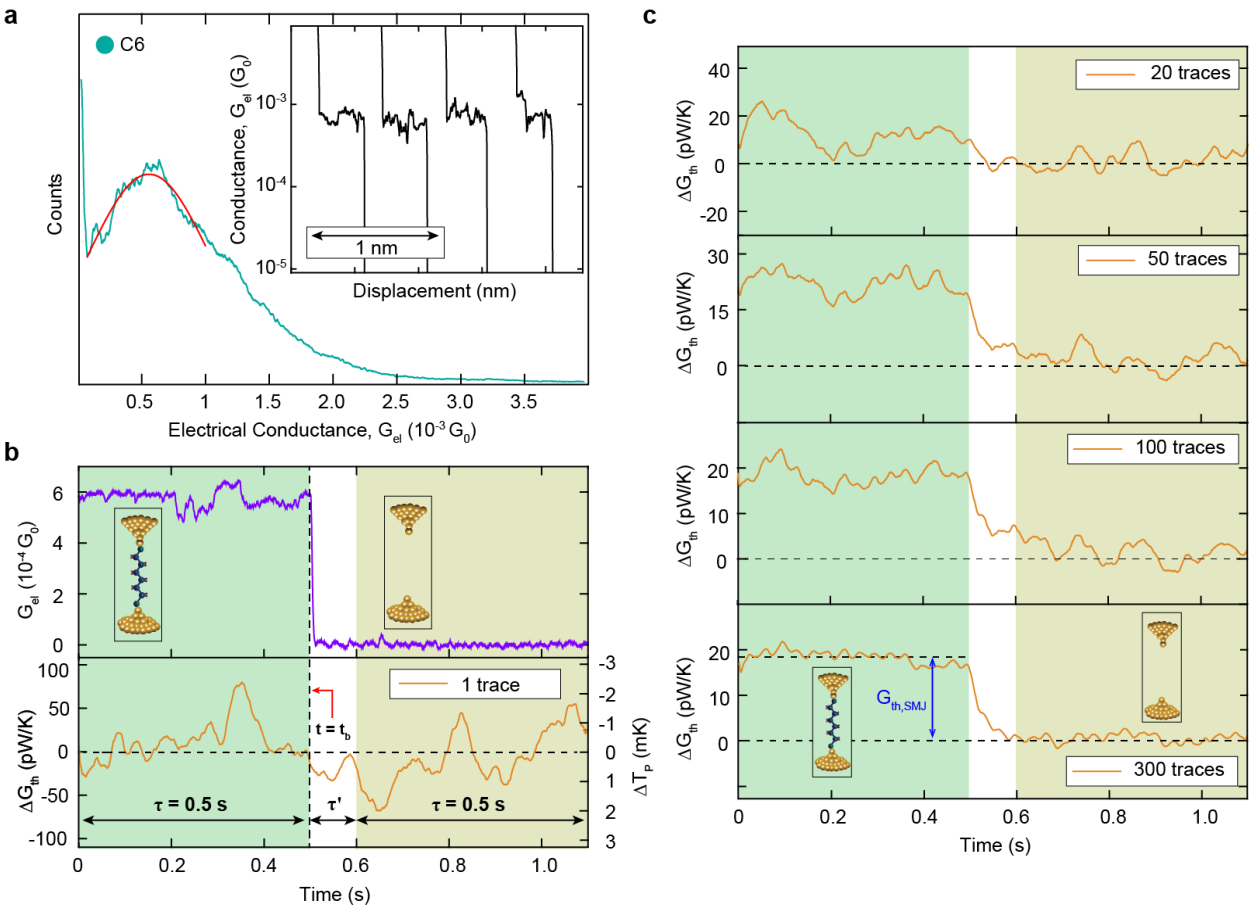

Figure 2.14 Measurement of electrical and thermal conductance of Au–C6–Au single-molecule junctions. (a) Main panel, histogram (shown in teal) of the electrical conductance of Au–C6–Au junctions obtained from approximately 500 independent traces of electrical conductance versus displacement. Inset, representative traces of the electrical conductance for four independent measurements. A Gaussian fit to the histogram peak is represented by the solid red line. (b) Experimental protocol for measuring the thermal conductance of a single-C6 junction. Upper panel, the electrical conductance trace indicates rupture (at time $t = t_b$) of a single-molecule junction by a sudden drop of the measured G_{el} value. Lower panel, the coincident thermal conductance change (ΔG_{th}, left axis) and the related temperature change of the probe (ΔT_P, right axis), where the small effects of Joule heating are already accounted for (see Chapter 2.5.8). It can be seen that, unlike the clearly identifiable electrical conductance change associated with the breaking of the junction, the corresponding thermal conductance change is not discernible in the noisy signal. (c) An improved signal-to-noise ratio is obtained upon aligning via G_{el} and averaging multiple thermal conductance traces. $G_{th,SMJ}$, indicated by the drop in the thermal conductance signal after 0.5 s, can be seen after averaging 50 traces and is about 18 pW K^{-1} for Au–C6–Au single-molecule junctions. The coloured regions in (b) and (c) with their insets indicate the discernible pre- and post-rupture portions of the recorded and averaged traces.

The ability to resolve the thermal conductance at the single-molecule scale offers unique opportunities to address fundamental questions[28,30] with regard to how thermal transport in single-molecule junctions depends on molecular characteristics. We illustrate this with additional thermal

transport measurements on a series of alkanedithiol molecules differing in the number of CH_2 units (from 2 to 10, with these molecules referred to as C2 to C10, respectively), to explore the influence of molecular length. Figure 2.15(a) shows the measured electrical conductance histograms for the studied molecules, with the Gaussian-fitted peak values summarized in Figure 2.15(c). The data document an exponential decay of the electrical conductance (G_{el}) of single-alkanedithiol junctions with increasing molecular length (L), indicating tunneling-dominated electron transport. We extract a tunneling decay constant (β, where $G_{el}/G_0 \propto e^{-\beta L}$) of 0.92 ± 0.05 per CH_2 unit, which agrees well with past work[75]. The measured thermal conductance of the single-molecule junctions containing C2 to C10 is shown in Figure 2.15(b), and the summary of the thermal conductance values is included in Figure 2.15(c). We note that, for all molecular junctions, the effect of Joule heating is systematically accounted for (see Chapter 2.5.8). In strong contrast to the measured length-dependent electrical conductance, the thermal conductance of the single-alkanedithiol junctions exhibits a nearly length-independent behavior with a value of approximately 20 pW K^{-1}, suggesting that thermal transport in single-molecule junctions is ballistic.

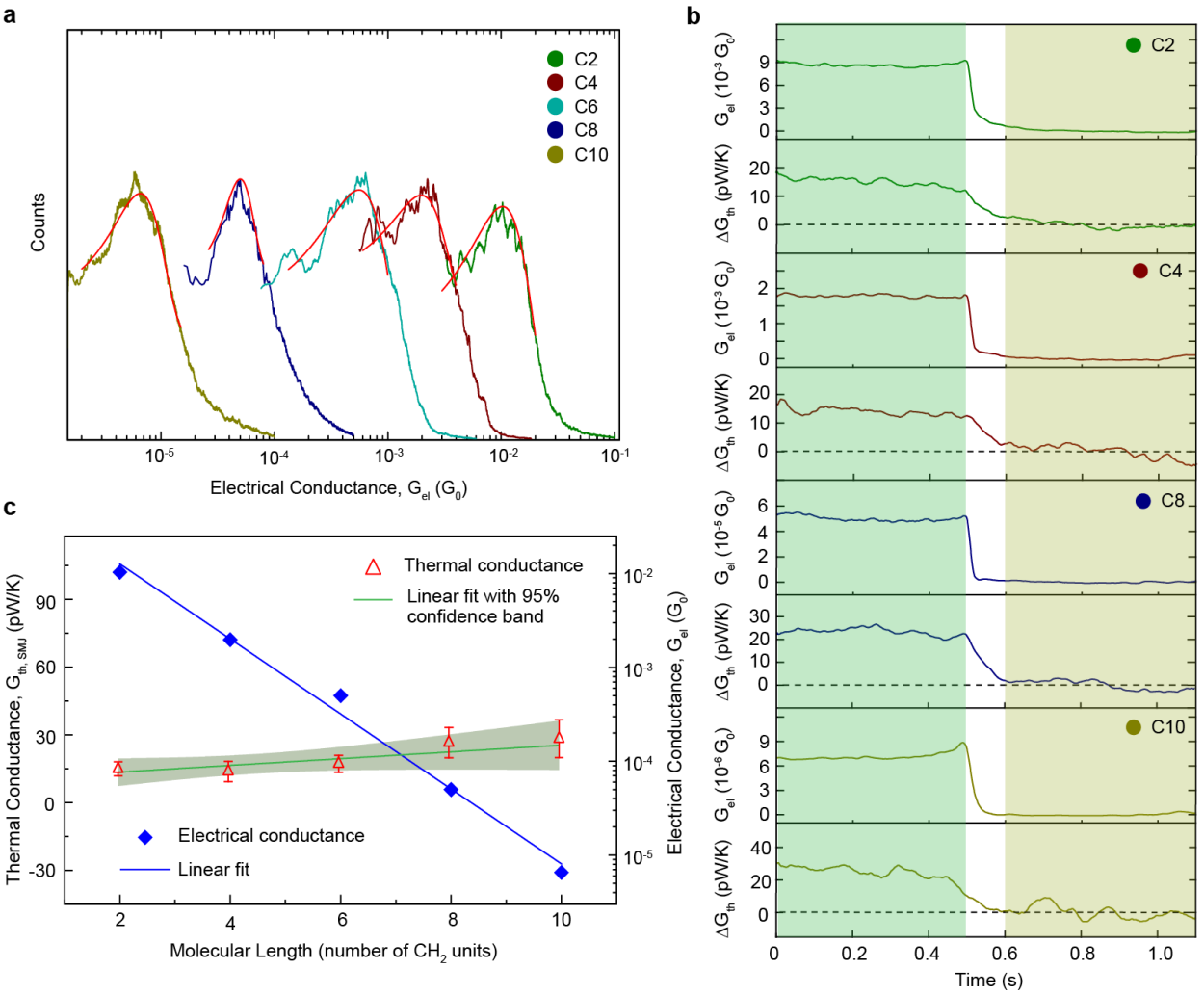

Figure 2.15 Length-dependent electrical and thermal transport in Au–alkanedithiol–Au single-molecule junctions. (a) Measured electrical conductance histograms for different alkanedithiol junctions (C2 to C10; see key). Red lines represent the Gaussian fit of the histogram peaks. (b) Electrical conductance and thermal conductance traces of single-alkanedithiol junctions obtained by averaging >100 traces for C2 (155 traces), C4 (133 traces), C8 (110 traces) and C10 (108 traces) junctions following the experimental protocol described in Figure 2.14(b). (c) Measured electrical (blue diamonds, right axis) and thermal conductance (red triangles, left axis) as a function of the molecular length, as given by the number of CH_2 units in the alkanedithiol junctions. The solid blue line indicates a linear fit to the electrical conductance data on a logarithmic scale. The measured thermal conductance data are fitted by a linear curve (green line) on a linear scale, with the region shaded in light green representing the 95% confidence band. Error bars represent one standard deviation of the data obtained from three sets of measurements for each molecule.

2.7 Discussion

The experimental results of single atomic junctions thermal conductance provide insights into thermal transport in atomic-size Au contacts and reveal conductance quantization at room temperature in Au atom junctions. We have also established the applicability of the Wiedemann-Franz law for analyzing thermal transport in metallic atomic-size contacts.

The experimental results of the single molecule thermal conductance illustrate a nearly length-independent thermal conductance in alkane-based single-molecule junctions, which is in strong contrast with the corresponding exponential dependence of the electrical conductance on length. In contrast to work on monolayers and polymer bundles, our work realizes the long-sought goal of unambiguous identification of thermal conductance at the single-molecule level.

From a measurement standpoint, the above-reported experiments were made possible by the caloric scanning thermal microscopy (C-SThM) probes I fabricated. The experimental advances presented here will enable systematic studies of thermal transport through 1D chains of atoms, individual polymer chains, and other one-dimensional systems, which have been studied theoretically and computationally for more than half a century[64,102] but have not been probed experimentally because of the lack of experimental tools.

Chapter 3

A Calorimeter Development for Probing Metabolic Heat Generation in *C. elegans*

3.1 Abstract

Calorimetry has been widely used in metabolic studies, but direct measurements from individual small biological model organisms such as *C. elegans* or isolated single cells have been limited by sensitivity and difficulties in resolving very small heat outputs. Here, by attenuating ambient temperature fluctuations to the micro-Kelvin level, via feedback control, and by careful thermal engineering, we developed a robust and highly sensitive and bio-compatible calorimetric platform that features an unprecedented resolution of ~270 pW, more than a 500-fold improvement over the most sensitive calorimeter previously used for measuring the metabolic heat output of *C. elegans*. Using this calorimeter, we demonstrate for the first time time-resolved metabolic measurements from single *C. elegans* worms at various developmental stages and found metabolic outputs ranging from 4 nW to 100 nW. Next, our data unambiguously show that the metabolic output is significantly lower in *C. elegans* mutants with greater life expectancy. These demonstrations clearly highlight the broad potential of this tool for studying the role of metabolism in disease, development, and aging of small model organisms, single cells and other reactions with sub-nanowatt thermal signatures.

3.2 Introduction

Calorimetry, a technique that can be utilized to quantify the amount of heat released or absorbed during chemical or physical processes, has been instrumental in analyzing the thermodynamics of reaction mechanisms[39,103]. Importantly, calorimeters are also critical for analyzing the metabolism of living cells and organisms, which is defined as the sum total of all the heat output associated with the biochemical processes in cells[41]. Because of the central role that energy and metabolism play in the normal function of cells[40], it is not surprising that metabolic changes are implicated in aging[104,105] and human diseases, such as cancers[106]. Calorimetric measurements, which directly record the heat generated by a (biological) system, represent a non-invasive approach for accurately characterizing metabolism, as the metabolic heat output is an integrated signal of both aerobic and anaerobic processes[107-109]. However, such calorimetric measurements have not been able to resolve the heat output from small individual organisms such as the nematode worm *Caenorhabditis elegans* (*C. elegans*), or isolated cells, due to poor sensitivity, insufficient long-term stability, and challenges in physiological compatibility.

In this work, we describe a novel calorimeter capable of systematically studying the metabolism of individual *C. elegans,* which is a widely used model organism for studies in cell and developmental biology because of their ease of maintenance and short generation times[110,111]. We note that this tool is expected to be broadly useful, as *C. elegans* metabolism is being actively investigated due to its promise for providing insights into human disease and ageing[104,105,109,112-115]. For example, it is well known that genetic mutations, such as *age-1* and *daf-2* mutants increase the lifespan of the worms mediated via various transcription factors with roles in insulin signaling, autophagy, and cellular energy metabolism[115-117]. Thus, metabolic heat output measurements on single worms through direct calorimetry can provide fundamental insights into

metabolic pathway regulation in the context of the above biological mechanisms. We note that so far *C. elegans* metabolic heat output studies have been limited to large populations of worms as existing calorimeters lack the desired sensitivity (~200–300 pW resolution) to resolve signals from a single worm[107-109,118]. Figures 3.1(a) and (b) show the highest resolution claimed for biological calorimetry is at the nanowatt level (1.9 nW)[119], and was achieved by miniaturizing calorimetric platforms[46,119] to such small sizes that they are unsuitable for studying relatively larger biological samples such as *C. elegans*. As a result, the most sensitive calorimeter used for measuring *C. elegans* was limited to a resolution of 170 nW[118] making it impossible to study metabolism from individual worms as shown in Figure 3.1(c). Finally, we note that none of the available tools have been able to monitor real-time metabolic heat changes with respect to worm size, their activity levels and individual physiological or genetic differences, posing significant barriers to progress.

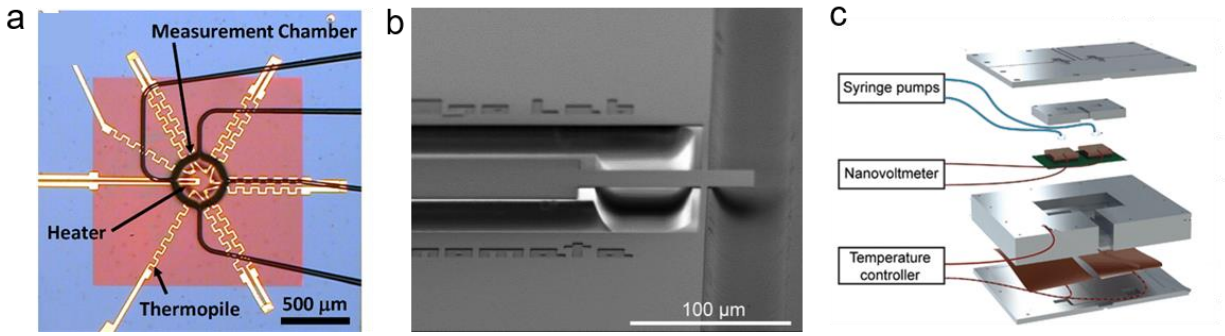

Figure 3.1 Biocalorimeters developed in past work.
(a) W. Lee et al[46] reported that this biocalorimeter achieved 4.2 nW resolution. They demonstrated chemical reactions using this calorimeter but did not apply to metabolic studies. (b) N. Inomata et al[119] microfabricated cantilever based calorimeter. When the cantilever temperature changes, the oscillating frequency is shifted to a different frequency. This calorimeter was used to measure a single brown fat cell metabolic rate but the reported value (more than a µW) is questionable. (c) R. Krenger et al.[118] introduced a temperature-controlled calorimter for monitoring *C. elegans* metabolic heat generation. The resolution of this calorimeter is 170 nW so that they monitored hundreds of *C. elegans* together. This calorimeter is the best-performing calorimeter used for probing *C. elegans* metabolic activities.

3.3 Fabrication of the calorimeter

The calorimeter reported in this dissertation was fabricated by Rohith Mittapally and myself. As described in detail below, the calorimeter is well suited for probing metabolic rates of single *C. elegans nematodes*. To increase a sensitivity of the calorimeter, lowering thermal conductance and improving temperature resolution are key requirements. For these reasons, nanofabrication processes and vacuum systems were introduced to miniaturize calorimeter size and to remove gas that contributed to heat transport. However, a biocalorimeter has several restrictions, because it has to accommodate biological samples. The calorimeter size cannot be smaller than the biological sample size and it also needs to incorporate liquid flow channels. In the case of *C. elegans*, the biocalorimeter sensing chamber size must be larger than that of adult *C. elegans*, which results at least in a $100\ \mu m \times 100\ \mu m$ cross-sectional size, and a length of at least 1 mm[110].

Borosilicate capillary tubes are adapted to calorimeter tubes for several reasons. First, a borosilicate capillary tube has the advantage of transparency for optical imaging. Second, borosilicate has a low thermal conductivity (k), which is reported as ~1.1 W/m.K[120]. Third, their flat surfaces aid in imaging by avoiding aberrations due to curvature.

Every thermal pathway must be carefully considered for lowering thermal conductance (G_{Th}): thermal conductance along via a gas ($G_{\mathrm{Th,cond,gas}}$) and solid materials ($G_{\mathrm{Th,cond,solid}}$), thermal conductance of convective heat transfer through liquid flow ($G_{\mathrm{Th,liquid}}$), and thermal conductance through radiation ($G_{\mathrm{Th,rad}}$). Here, thermal radiation ($G_{\mathrm{Th,rad}}$) contributions to the total thermal conductance ($G_{\mathrm{Th,total}}$) becomes significant in smaller size and this value is comparable to heat conduction along tubes ($G_{\mathrm{Th,cond,solid}}$). Since thermal radiation is proportional to the

surface area and borosilicate emissivity is relatively large (> 0.8), the capillary tubes are coated by thin gold (Au) films, which has lower emissivity (< 0.1)[121]. In addition, this a high-quality Au film can be utilized for uninterrupted electrical current flow to a NTC thermistor (10 k, -4% TCR).

3.3.1 Fabrication steps

The steps involved in the fabrication of the calorimeter are shown in Figure 3.2.

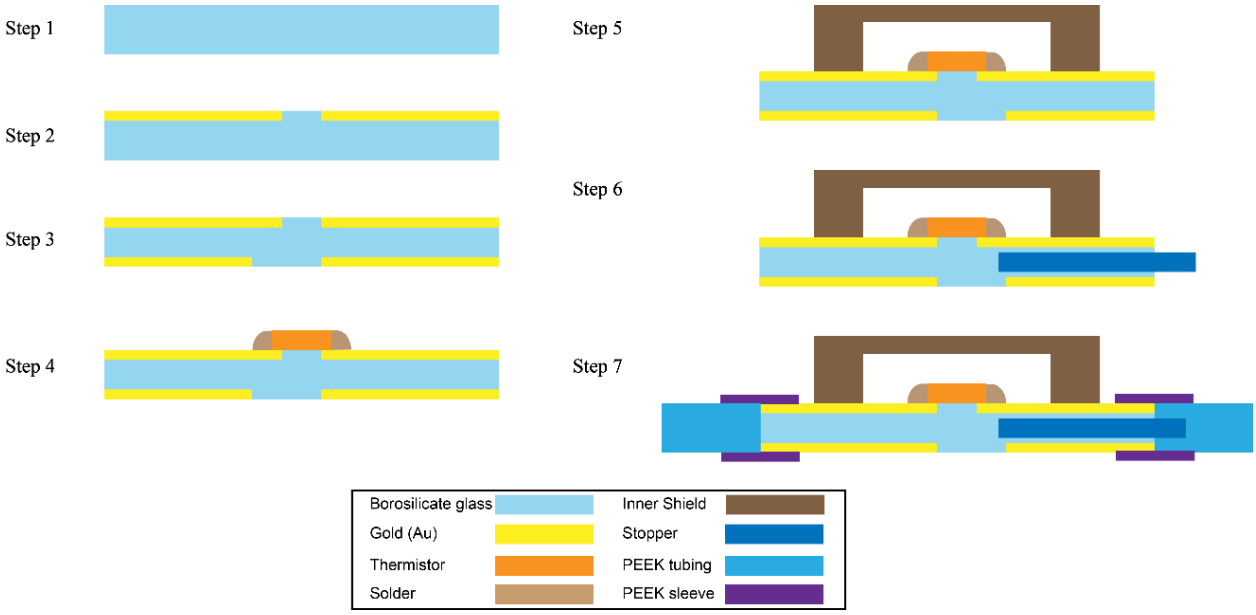

Figure 3.2 Fabrication steps for the calorimeter.
(Step 1) Perform chemical and oxygen plasma cleaning of borosilicate capillary tubes. (Step 2) Using a shadow mask, deposit 10/100 nm Ti/Au to form a metal coating. (Step 3) Flip the tubes and deposit 10/100 nm Ti/Au again to cover most of the tubes including sides of the tube while leaving a small access window at the center for imaging. (Step 4) Position and solder a thermistor (Murata Electronics, NCP03, 10 kΩ) between the Au films deposited in step 3. (Step 5) Affix the tubes to the IS using silver epoxy to achieve good thermal contact with the window facing downwards. (Step 6) Insert a stopper inside the tube to localize the worms. (Step 7) Connect PEEK tubing to the borosilicate capillary tube using PEEK tubing sleeves.

The fabrication process proceeds as follows.

Step 1)

Borosilicate capillary tubes (VITROCOM) are 50 mm long, hollow, borosilicate capillary tube (250 × 250 µm, wall thickness 50 µm), shown in Figure 3.2 and Figure 3.3. They are cleaned

through chemical processes (10 min piranha solution + 5 min acetone + 5 min isopropyl alcohol). Subsequently, tubes are further cleaned in an oxygen plasma cleaner (Yes plasma cleaner, 800 W at 150° C for 1 minute) to remove organic contaminants and improve surface adhesion for further processing. Note that a reverse action tweezer is recommended for handling tubes during wet cleaning.

Step 2)

Tubes are then masked with Kapton tape before coating with 100 nm thick gold on all sides except a small portion in the center to provide optical access for imaging. 10 nm Titanium (Ti) is used for an adhesion layer in Au deposition. The first mask (~ 400 µm across) in the center provides the isolated electrical leads. Figure 3.3 shows a detailed view of borosilicate capillary tubes as thermal bridges.

Step 3)

To coat Au on the opposite surface, tubes are flipped from a wafer and again masked with Kapton tape. The Kapton tape width for a mask (~2 mm) is thicker than the first mask (~400 µm) to generate a transparent window for optical access. Note that two sidewalls of the capillary tubes are also coated with Au because of the isotropic directionality of sputtering. We estimate that two sides of the tubes' Au thickness are similar to the front and backside because these sides were deposited twice.

Step 4)

Tubes are fixed to the glass slide using Kapton tape and the glass slide is placed on the heater. A thermistor (Murata Electronics, 10 kΩ) is used because it is one of the smallest thermistors available on the market with high TCR values (-4%). The thermistor is loaded between Au films (electrodes at here) using vacuum epoxy (Loctite) for adhesion. Vacuum epoxy is mixed

on the other dish and a small amount of epoxy is placed on the tube through a needle tip to minimize the adhesive amount. Subsequently, the thermistor is placed on the tube and warmed at 60 °C for 4 hours for curing epoxy. When the epoxy is fully cured, a liquid solder (Koki lead-free solder paste, S3X58-M406-3) is applied on the thermistor leads. The amount of liquid solder is also minimized by dipping a needle tip on a liquid solder dish. The solder tip is held near the thermistor until the liquid solder forms an electric connection between a thermistor and Au pads on the tubes.

Step 5)

The tubes are flipped and mounted on the inner shield (IS). Here, a thin glass slide (100 μm thickness) is used for electrical isolation between the IS and the tubes. This glass slide can increase thermal resistance between tubes and inner shield; this should be avoided to maintain the temperature stability of tubes. For this reason, instead of general vacuum epoxy, a silver epoxy (H20E Epo-Tek) is adopted for better thermal contact. The silver epoxy is sandwiched between a glass slide and an inner shield surface and therefore it takes up to 24 hours to be cured on a hot plate warmed to 60 °C.

Step 6)

A 125 μm core diameter glass fiber was inserted into the capillary tube as a stopper for biological samples to be located under the thermistor for resolving heat output. The fiber is fixed at the exposed end with epoxy. The vacuum epoxy is applied on the glass fiber-inserted side of the tube to fix the stopper's location during liquid flow. It is cured for 4 hours at 60 °C. Once the epoxy is cured, the remaining extruded glass fiber is cut so that the PEEK tubing is accessible in the following step.

Step 7)

A PEEK tube (360 µm/150 µm OD/ID) is connected to the capillary tube through a PEEK tubing sleeve (800 µm/400 µm OD/ID) and all the gaps are sealed with a vacuum epoxy. Figure 3.3 shows a detailed cross-sectional view of PEEK tubing connections. PEEK tubing sleeves are first connected to the ends of borosilicate capillary tubes and vacuum epoxy is applied. When PEEK tubing sleeves are cured, the PEEK tubing (360 µm OD, 150 µm ID) is connected into the sleeves and vacuum epoxy is again applied. After this step, the calorimeter is ready to be connected to the middle shield and outer shield. This tubing system is then anchored to the middle shield (MS). The glass side with silver epoxy is also placed on the middle shield so that PEEK tubing can sit on the middle shields too. The connection to the MS can further stabilize calorimeter temperature. Finally, PEEK tubing is passed through microfluidic connectors (MicroTight® Adapter PEEK 1/16" ID x 360 µm w/Fittings) on the outer shield (OS) which act as vacuum feedthroughs to the outside.

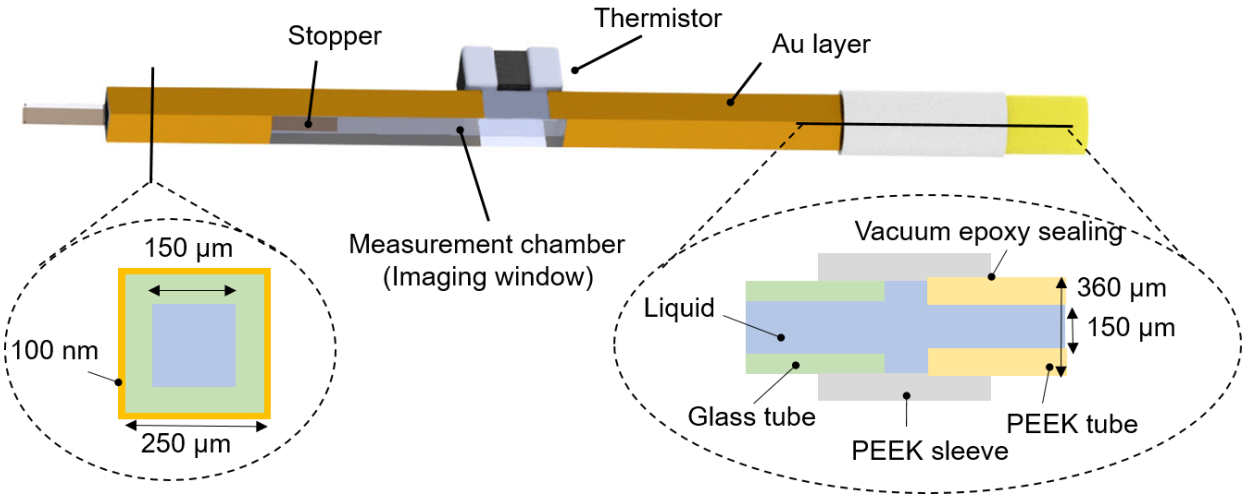

Figure 3.3 Schematics of the custom-designed biocalorimeter.
(a) Schematics of the sensing calorimeter. (b) The cross-sectional view of the capillary tubes. Note that the square capillary tubes have 50 µm wall thickness. The Au layer is coated on the outside of tubes to reduce radiative conduction. (c) The cut-view of the interface between borosilicate tubes and PEEK tubes. The diagonal width of glass capillary tube is 350 µm ($250\sqrt{2} \times \mathbf{250}$ **µm**) so that it can be aligned to the PEEK tube (360 µm). Both tubes are inserted to the PEEK sleeve with vacuum epoxy to seal.

3.4 Characterization of calorimeter properties

3.4.1 Thermal conductance of the calorimeter

The heat output resolution is determined by the thermal conductance of the capillary tube (low values of G_{th} are desirable for increased resolution of $\dot{Q}_{metabolic}$) and the temperature resolution of the thermistor[42,87]. In our system, we achieve a small G_{th} by carefully engineering the capillary tube to minimize the contribution of the various heat pathways (conduction, convection, and radiation). Specifically, the conductive contribution to G_{th} is minimized by choosing a sufficiently small cross-section ($G_{capillary}$ = 9.6 μW/K, G_{buffer} = 6 μW/K), while the thin gold coating (G_{Au} = 2.7 μW/K) on the capillary reduces the radiative contribution to G_{th}. Nevertheless, providing optical access to the calorimeter results in some unavoidable radiative coupling (G_{rad} ~6 μW/K) to the outside environment. Since the capillary is operated in a vacuum system, the convective contribution is reduced to negligible levels ($G_{th,air}$ ~ 250 μW/K).

To experimentally measure the thermal conductance of our capillary system, power is provided by Joule heating (DC voltage through the thermistor) and the resultant temperature rise is measured by the thermistor on the capillary tube. A DC voltage (V_{DC}) is superimposed on the sensing AC voltage (V_{AC}) that results in DC temperature rise (T_{DC}) of the sensing capillary tube corresponding to the power rise of $P_{DC} = V_{DC}^2/R_{th}$, where R_{th} is the nominal resistance of the thermistor at room temperature (~10 kΩ). This temperature rise T_{DC} is measured with the thermometry technique discussed above. The slope of P_{DC} with respect to T_{DC} gives the thermal conductance G_{th} of the capillary system (Figure 3.4(a)). 3 different flow rate conditions (stationary, 100 nL/min and 200 nL/min) are tested and G_{th} are 25 μW/K, 27 μW/K, and 29 μW/K, respectively.

3.4.2 Time constant of the calorimeter

The definition and basic equation of time constant are covered in the previous chapter with Eq. 2.4. A small thermal time constant is preferred because the calorimeter can resolve the thermal signal within a short time. However, thermal time constant and thermal conductance are correlated so that the time constant cannot be infinitely reduced. In this biocalorimeter, thermal conductance and time constant are dependent on the length of the tube (L). When the length (L) increases to lower thermal conductance (G_{th}), it results in time constant (τ_{th}) increase. A too-long time constant (τ_{th}) cannot monitor real-time change metabolic heat output change. As a result, the 20 mm length of capillary tube was designed to prevent time constant (τ_{th}) from exceeding 100 sec. The temperature signal read by a thermistor is monitored by applying Joule heating to the calorimeter. DC voltage was applied to the thermistor to increase 1 mK of the sensing chamber, and the temperature signal of a thermistor was monitored. As a result, the temperature signal monitored by a thermistor should be delayed due to calorimeter thermal time constant (τ_{th}) and it is determined to be ~100 sec. In other words, the temporal resolution of our calorimeter is set by the thermal time constant of the device which is ~100 sec (Figure 3.4(d)).

3.4.3 Thermal resolution of the probe

The principle of operation of our calorimeter can be understood by noting that when heat is generated inside the sensing capillary tube (e.g. due to the metabolic output of a sample), its temperature rise, $\Delta T_{th,}$, is detected by the thermistor and can be directly related to the metabolic heat output ($\dot{Q}_{metabolic}$) via $\dot{Q}_{metabolic} = G_{th} \times \Delta T_{th}$, where G_{th} is the thermal conductance of the sensing capillary tube. G_{th} can be directly measured in Chapter 3.4.1 and the G_{th} under operating conditions (100 nL/min) is 27 μW/K, and the noise floor of the temperature measurement is 10

μK (see Chapter 3.5). As a result, our calorimetry successfully detects 270 pW of heat output ($\dot{Q}_{metabolic}$ = G_{th} × ΔT_{th} = 27 μW/K × 10 μK). It is noted that we did not claim our resolution by simply multiplying thermal noise floor and thermal conductance. Here, we demonstrate that our calorimeter can actually resolve 270 pW power input by adopting the G_{th} measurement technique. A DC voltage (V_{DC}) is superimposed on the sensing AC voltage (V_{AC}) that results in DC temperature rise (T_{DC}) of the sensing capillary tube corresponding to the power rise of $P_{DC} = V_{DC}^2/R_{th}$, where R_{th} is the nominal resistance of the thermistor at room temperature (~10 kΩ). In Figure 3.4(c), the sensing signal (green line) clearly reads the applied heat output increments of 270 pW, which is an unquestionable demonstration of calorimeter's thermal resolution.

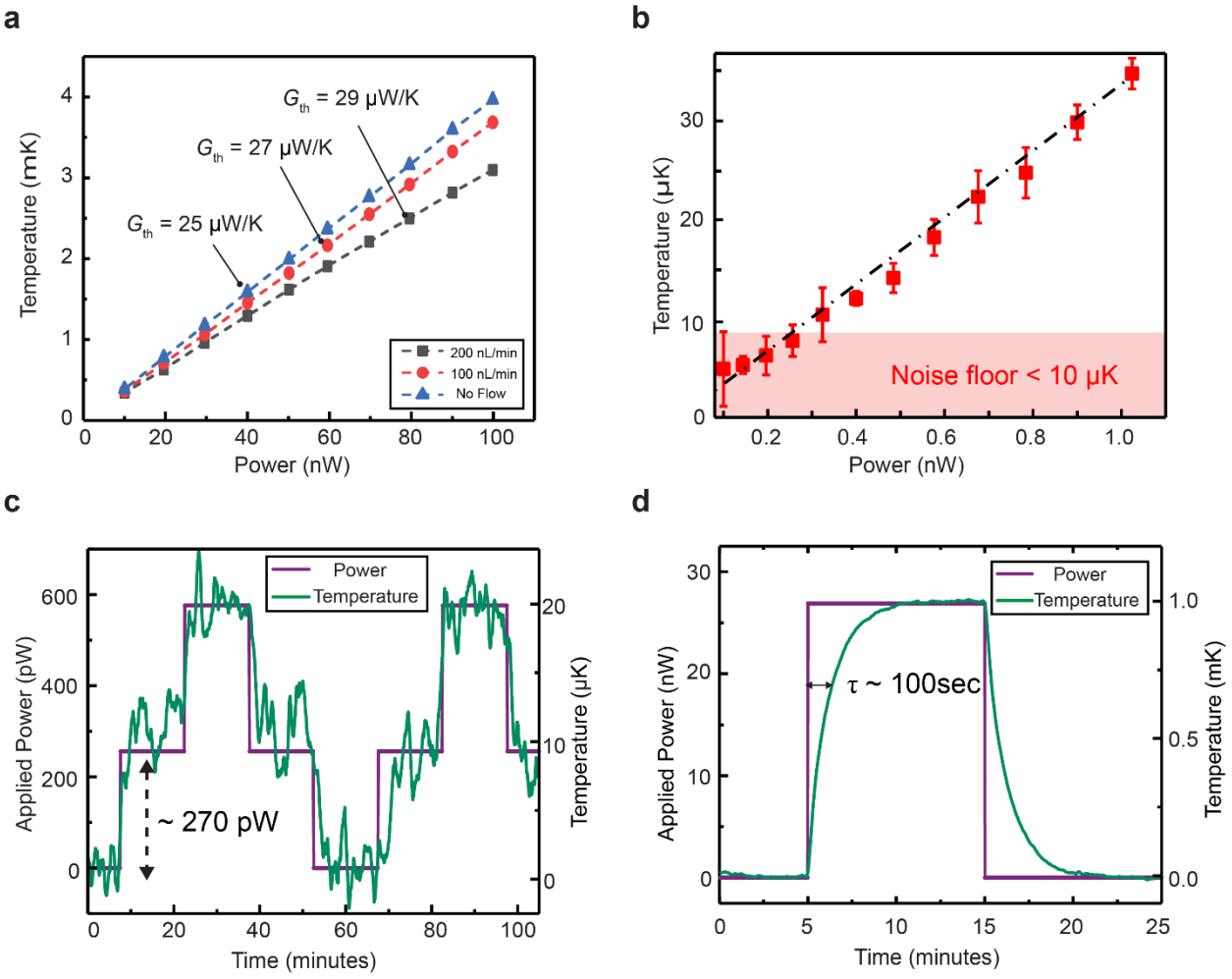

Figure 3.4 Thermal characterization of the calorimeter.
(a) Thermal conductance (G_{th}) measurement under different operation conditions: Effect of flow rates, G_{th} increases as flow rate increases. Our metabolic heat output measurements were performed at a 100 nL/min flow rate, which corresponds to a thermal conductance of 27 μW/K. (b) The temperature rise in the range of 0-40 μK, indicating a noise floor of ~10 μK. (c) Validation of thermal resolution. A thermal pulse (purple solid line) with steps of 270 pW applied on the capillary resulted in a corresponding 10 μK rise on the temperature signal (green solid line), validating our calorimeter's capability to resolve at least 270 pW (heat resolution). (d) Time constant of the sensing capillary tube. A square thermal pulse (purple solid line) in steps of ~27 nW results in a first-order temperature response with a time constant of ~1.5 minutes.

3.5 Thermal system for achieving high temperature stability

3.5.1 High stability temperature system

To improve the temperature resolution, we built a three-shield system (Figure 3.5) with large thermal time constants to decouple high-frequency temperature fluctuations from the ambient

and controlled individual shields' temperature in a proportional-integral-derivative (PID) loop to reduce low-frequency temperature fluctuations. All three shields are made of Cu and machined by CNC (Okuma GENOS M560-V). The outer shield (OS) is a nested three-shield structure forming a vacuum enclosure ($20 \times 20 \times 12$ cm^3, wall thickness 1.2 cm) with electrical, optical and fluidic feedthroughs holding vacuum down to at least 10 μTorr. Thermistors (US Sensor Corp. USP12838) are bonded using epoxy (3M Scotch-Weld Epoxy Adhesive 2216 B/A) to each shield in a drilled hole at a representative location and provide temperature feedback for PID control. Polyimide flexible heaters (Omega KH series) are attached in series to each shield on different surfaces providing uniform heat to the system. The middle shield (MS) ($7 \times 7 \times 3.5$ cm^3) with a central pocket ($4 \times 4 \times 2$ cm^3), is held on the bottom part of OS supported by four spherical borosilicate balls. The inner shield (IS) ($3 \times 3 \times 1.2$ cm^3) with a central pocket ($2 \times 0.8 \times 0.6$ cm^3), is then suspended in the MS pocket by 3 polymer supports with a spherical end. These spherical contacts provide weak thermal links (OS/MS – 50 mW/K & MS/IS – 5 mW/K) while maintaining robust mechanical stability. IS in Figure 3.6(a) is coated by thin Au film to reduce thermal radiation coupling to MS and OS (Figure 3.6(b)). The lead TO headers (Spectrum Semiconductor Materials Inc, HDR01833) are inserted in the IS to sense thermal signals from both calorimeter and IS. From the thermal mass of copper shields and the calculated thermal conductance, the thermal time constants of the OS, MS, and IS are estimated to be 3,000 s, 12,000 s, and 1,600 s respectively, which match the time constants obtained experimentally. The PID control scheme, as described in the following section, enables our setup to maintain OS, MS and IS temperatures to within ±1 mK, ±15 μK, and ±15 μK, respectively.

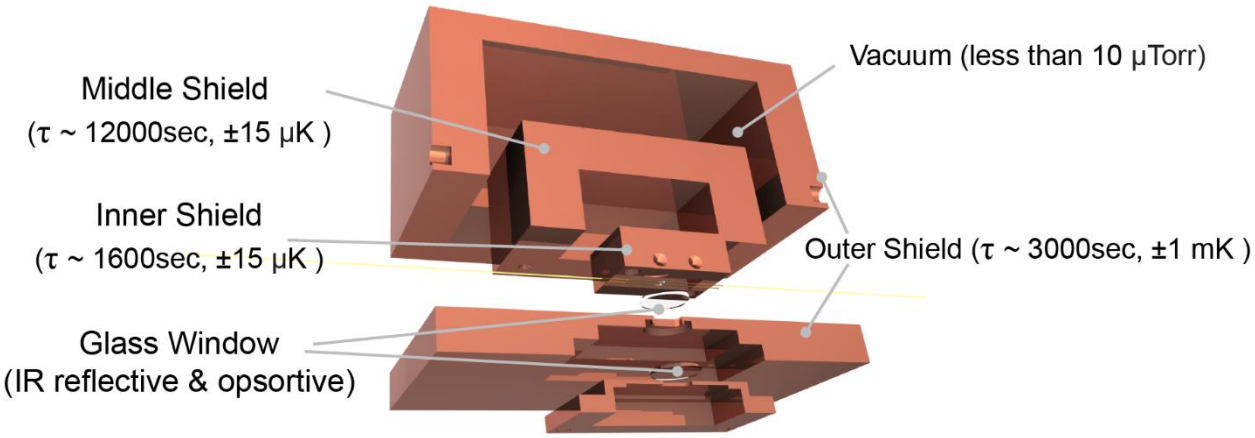

Figure 3.5 Expanded view of thermal shields.
Detailed isometric expanded view of the thermal system showing the assembly of all components.

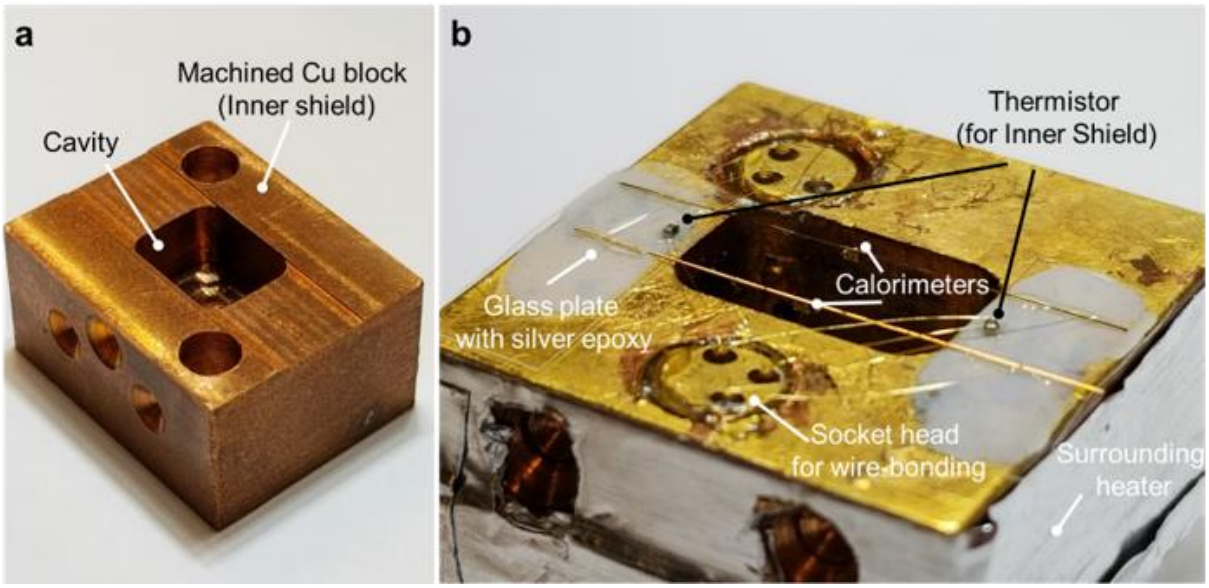

Figure 3.6 Actual image of the Inner Shield.
(a) Inner Shield of a machined Cu block. (b) Actual image of Inner Shield after calorimeter loading. Note that this calorimeter cannot operate because the ends of the capillary tubes were cut. Two sockets were fixed to the Inner Shield and electrically isolated from Inner Shield to acquire signals for temperature sensing and control. The sides of Inner Shield are wound by flexible heaters.

3.5.2 Thermometry & temperature control of shields

In order to measure temperature changes with μK resolution, we used resistance-based thermometry in an ac-driven Wheatstone bridge configuration (Figure 3.7(a)). Briefly, the right half of the bridge consists of a sensing resistor on the lower branch with an associated resistance on the top while the left side is described as the matching side. Fixed resistors with ultra-low temperature coefficient of resistance (Vishay Z201 Series Z-Foil Resistors, $\pm$ 0.2 ppm/K) are used with the resistance values chosen to improve the stability and resolution based on previous studies[25,31]. To balance the bridge, a fixed matching resistance equal to that of the sensing thermistor's resistance at its average temperature of operation is used while a potentiometer (Vishay Spectrol 534 series, $\pm$ 20 ppm/K) is used on the top branch of the matching side for fine tuning. The bridge is excited by a sinusoidal voltage (1 V peak-to-peak) using a waveform generator (Agilent 33210) at frequencies in the range of 10-100 Hz (frequencies were selected to avoid cross-talk). We note that this sinusoidal voltage dissipates ~12.5 μW in the calorimeter, causing the sensing capillary temperature to rise by 0.5 K above the IS temperature. The matching and the sensing signals are then fed into an instrumentation amplifier (Analog Devices AD524) where the common-mode signal is subtracted, and differential mode AC signals are amplified (Gain = 100 and Gain drift is at most 25 ppm/K). The amplitude of this amplified signal is then measured in a lock-in scheme (SRS 830) at a bandwidth of 0.1 Hz and recorded using a data acquisition card (PCI-6014) in the LabVIEW environment. The temperature resolution of the resulting circuit is quantified to be ±5 μK (Fig. 3.8).

To provide current to the polyimide heaters introduced above, we developed a voltage-controlled current source (Figure 3.7(b)) where the emitter voltage of the transistor is controlled through an op-amp with the polyimide heater on the collector side. This op-amp is configured to

sum a manual voltage signal (V_{man}) providing heat to reach the desired temperature and a controlled voltage signal (V_{PID}) to stabilize the temperature at that set-point in a PID loop (Figure 3.7(c)). The temperature measured from the Wheatstone bridge circuit acts as a feedback to the PID controller (implemented in LabVIEW) whose output controls V_{PID}. Preliminary PID parameters were obtained from the step response of each thermal system using SIMC criterion[32] and were further manually tuned to minimize the temperature fluctuations.

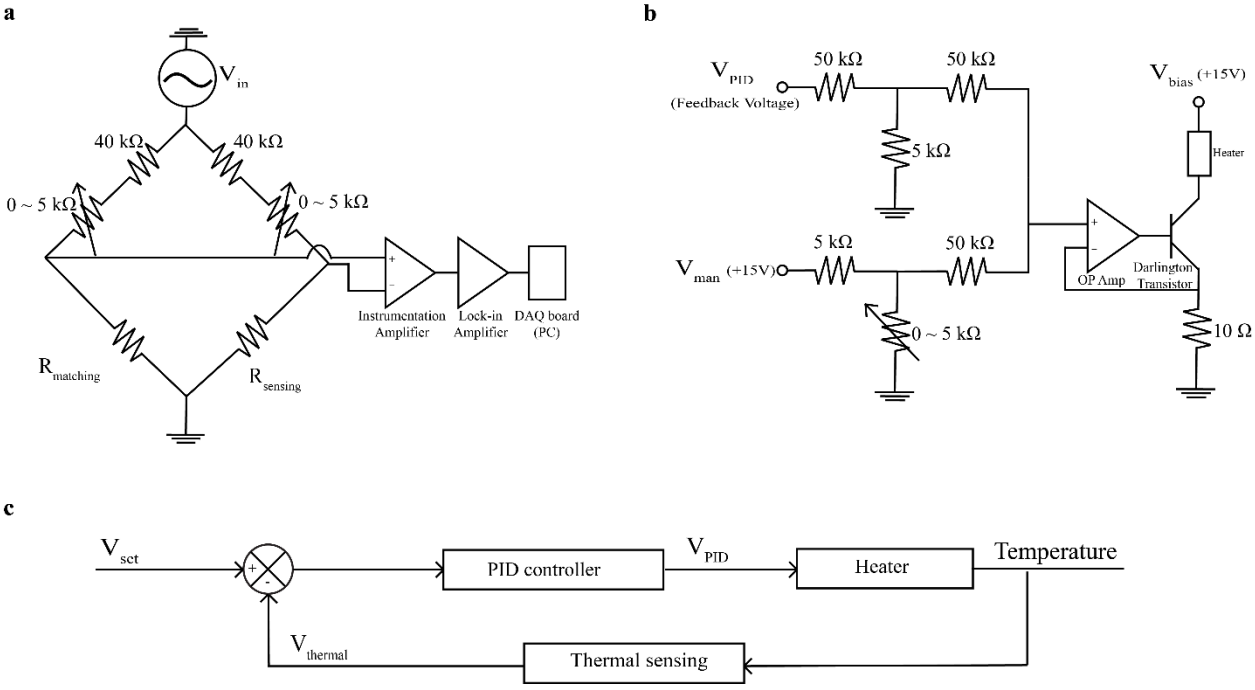

Figure 3.7 Electronic circuit diagram and schematic of the Proportion Integral Derivative (PID) controller employed for temperature control.
(a) Circuit diagram for the calorimetry temperature measurement and shields' temperature measurement. When the resistance of the sensing thermistor, $R_{sensing}$, changes due to *C. elegans* heat production at the center of the tube, an AC voltage difference, $V_{sensing} - V_{matching}$, develops across the bridge. When the resistance of the sensing thermistor, $R_{sensing}$, changes due to environmental temperature drift, similar changes also arise in the resistance of the matching thermistor $R_{matching}$ and keep the bridge voltage balanced, thus attenuating detrimental effects of temperature drift. This ac voltage is amplified in an instrumentation amplifier (AD524) and demodulated with a Lock-in Amplifier (Stanford SR830). This output voltage, $V_{thermal}$, is digitized via a data acquisition board (PCI-6014) and a custom LabVIEW program. We note that similar circuits are used for sensing the shields' temperature by incorporating a precision fixed resistor as $R_{matching}$. (b) Schematic of the circuit employed to drive the heater. V_{man} is set to a certain value to supply a fixed current through the resistive heater. V_{PID} is added to V_{man} to adjust the current supplied to the heater by controlling the transistor emitter voltage. The current to the heater is set by $V_{emitter}$ divided by 10 Ω. (c) Block diagram of PID feedback loop. Temperature is controlled stably through a PID control system. $V_{thermal}$ is compared to V_{set} and a net voltage is delivered to PID controller. V_{PID} adjusts the current flow through the resistive heaters (as shown in (b)) and the controlled temperature is read by thermal sensing circuit (as shown in (a)). This loop continues to maintain $V_{thermal}$ to be V_{set}.

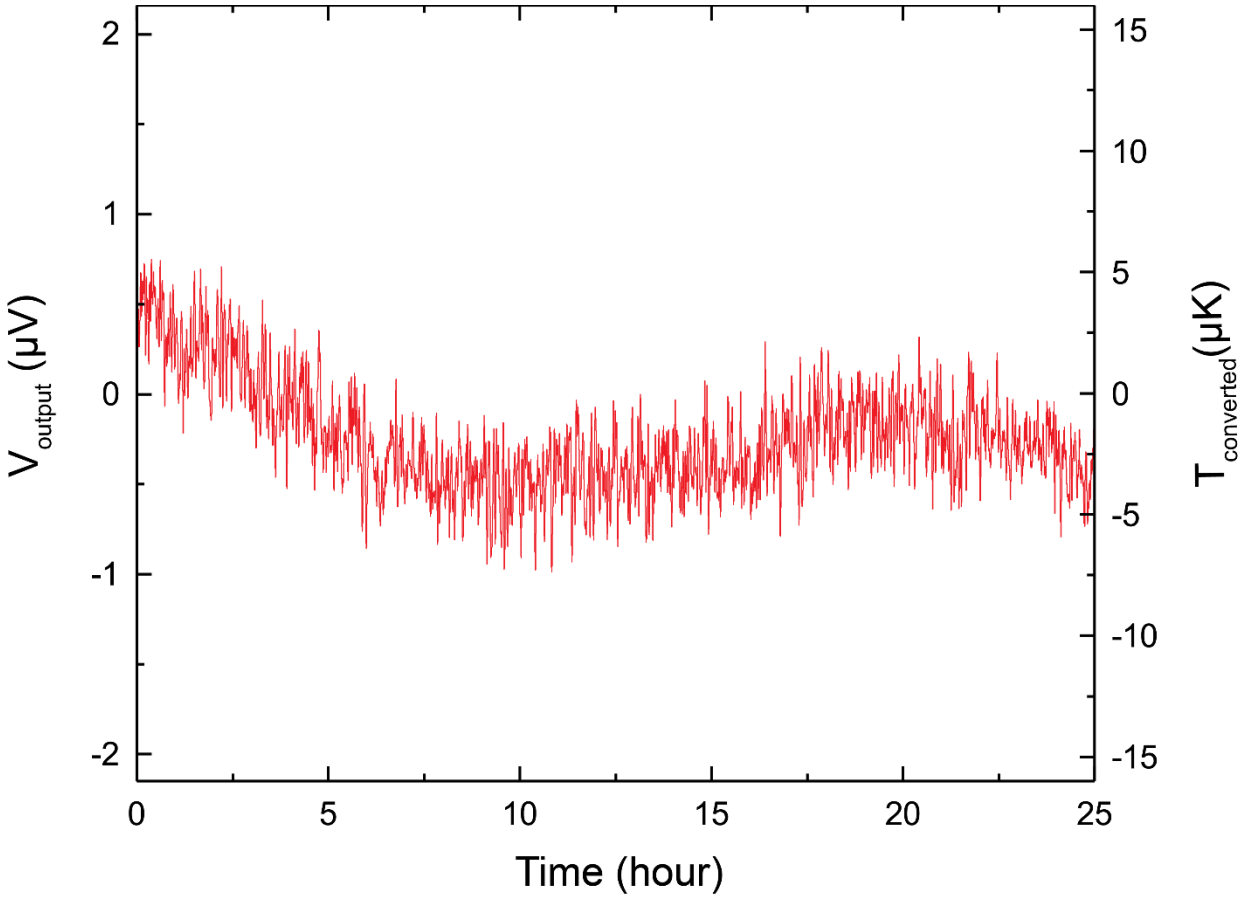

Figure 3.8 Drift of the output signal of the electronic circuits over a 25 hour period with fixed inputs.
For this control measurement, the sensing thermistors were replaced with fixed precision resistors. The corresponding temperature drift is ±5 μK.

3.5.3 Temperature stability of the calorimeter through the thermal shields and the temperature control system

To elaborate, the shields are comprised of an OS, MS and an IS (Figure 3.5 and Figure 3.10), which are nested into each other and are mechanically held together by weak thermal links to provide excellent thermal isolation from the ambient. The OS also serves as a vacuum chamber such that the all components included in it (including the capillary tubes) are maintained at a vacuum level below 10 μTorr. Further, the OS features custom-made instrumentation, fluidic and optical feedthroughs, and is actively controlled to temperature stability of ±1 mK (all temperature

signals are measured in a bandwidth of 0.1 Hz, unless otherwise mentioned). The MS and IS provide temperature stabilities down to ±15 μK through active PID feedback control (see Figure 3.5). We note that this temperature stability (with direct optical access) is comparable to the best stabilities achieved previously in similar approaches but without optical access[122,123].

The sensing and matching capillary tube systems are suspended on the IS (Figure 3.6(b) and Figure 3.11). Both tubes are instrumented with thermistors at the center of the tubes. The two capillary tubes have nominally identical dimensions and are 20 mm-long borosilicate tubes with a square cross-section, (250 μm × 250 μm outer dimensions and 50 μm wall thickness). Further, the tubes are coated with a 100 nm-thick layer of gold on all sides except a small portion in the center that provides optical access for imaging (Figure 3.3 and 3.11). A 125 μm-diameter borosilicate rod is inserted from one end into the sensing capillary tube until it reaches the center and serves to localize the worm in the center of the capillary tube where the thermistor is mounted (Figure 3.3 and 3.11).

We achieved excellent temperature resolution (ΔT_{th} = 10 μK) by employing an AC-excited Wheatstone bridge to minimize thermal fluctuations of the capillary tube via feedback-controlled shields (described above). Further, we take advantage of a thermistor embedded into the matching capillary tube (see Figure 3.6(b) and 3.11) to attenuate any common-mode temperature drift. Taken together, this approach enables a noise equivalent temperature (NET) resolution of ±5 μK over 2 hours and ~10 μK drift (bandwidth of 5 mHz) over 24 hours (Figure 3.9). This implies that, in addition to being able to resolve transient heat output changes (occurring in mins) of 270 pW (Figure 3.4(c)), our system can track heat output changes over a day with a same accuracy. Thus, our instrument is well-suited for real-time metabolic measurements on several small biological specimens like *C. elegans*.

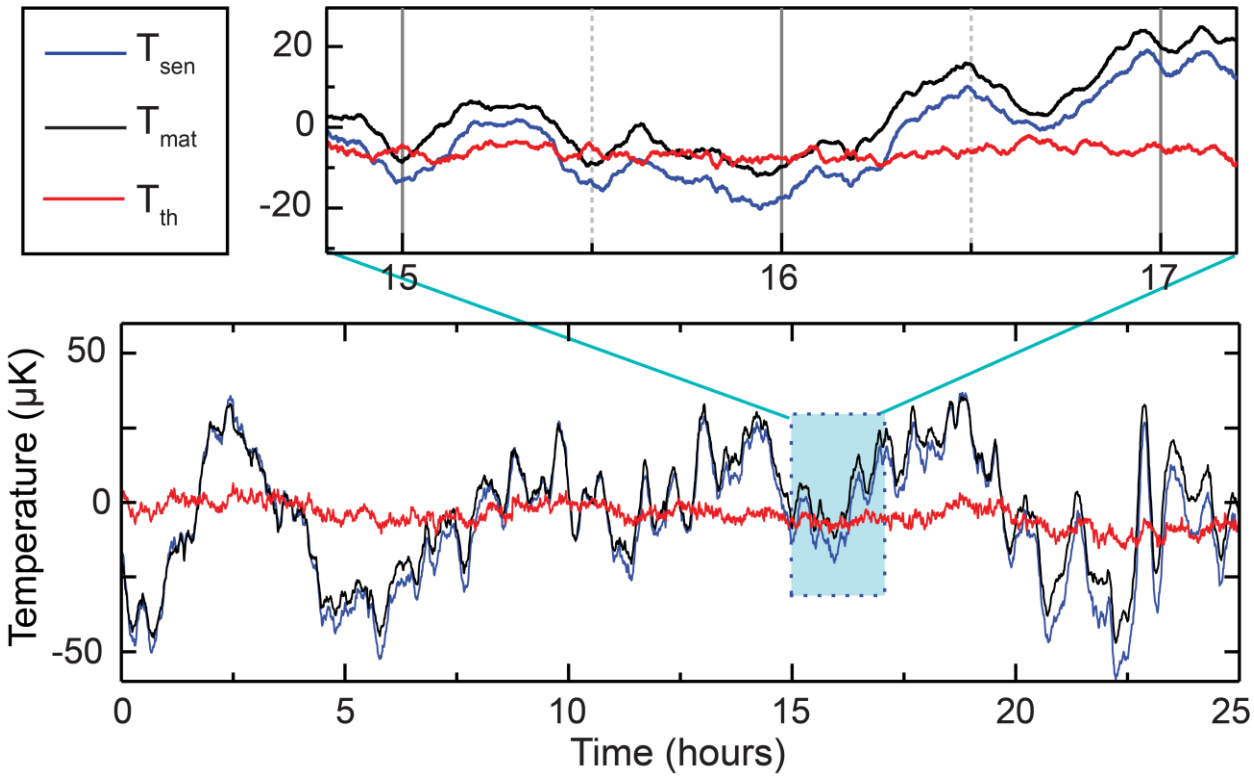

Figure 3.9 Long-term temperature stability for both sensing and matching calorimeters
Temperatures of both the capillaries (T_{mat} in solid black, T_{sen} in solid blue) without any sample in the sensing capillary tube are plotted for a 30 h timespan, indicating fluctuations of ±5 μK in the differential signal. A 2 h window (blue box) clearly shows that T_{mat} follows T_{sen} indicating a common-mode radiative coupling to the environment.

3.6 Experimental setups and measurement protocols

Our novel calorimeter provides an unprecedented heat resolution of ~270 pW—a 500-fold improvement over calorimeters employed for past *C. elegans* studies and a 10-fold improvement compared to the state-of-the-art biocalorimeters. Further, our approach also incorporates a fluidic environment and optical imaging capabilities. Our instrument is made possible by integrating three sub-systems (see Fig. 3.10(a) and (b)): First, a thermal system composed of three nested shields (Fig. 3.10(a)) made from copper (whose temperature is feedback-controlled) that house two capillary tubes—a sensing capillary tube containing the sample of interest and a matching capillary

tube which acts as a reference (described in Chapter 3.5)—ensures that ambient temperature fluctuations have a minimal effect on the temperature of the capillary tubes. Second, a fluidic system enables transfer of individual worms into the sensing capillary tube and maintaining them under physiological conditions in Figure 3.10(a) and (b). Third, an inverted microscope-based imaging system facilitates tracking of the activity of the biological specimen in Figure 3.10(a) and (b). The schematic drawing shows 3 systems (thermal, fluidic and imaging), but the actual system is more complex. Figure 3.10(b) shows more detailed information of experimental setups. Note that vacuum pumps and data acquisition (DAQ) systems are located outside of the measurement room to avoid temperature fluctuations while the circuits (Wheatstone-bridge, heater) are placed close to the thermal shields due to 1) the limited electric feedthrough cable lengths and 2) the necessity of stable temperature to avoid circuits' signal drifts. There are 8 circuits in total on the left side (near the syringe pump). 3 heater circuits are for controlling thermal shield temperatures, 3 Wheatstone-bridge circuits are for reading 3 shields temperature to feedback control, and 2 Wheatstone bridge circuits are for acquiring thermal signal from both the sensing and matching calorimeters.

The entire system is mounted on an inverted microscope and the sensing capillary is imaged through a 10x objective to monitor the specimen's activity. Finally, the fluidic system consists of a syringe pump at one end, for manipulating the specimen and flow rate, and a reservoir (petri dish) at the other end, for loading or unloading specimens (see Figure 3.10(a)).

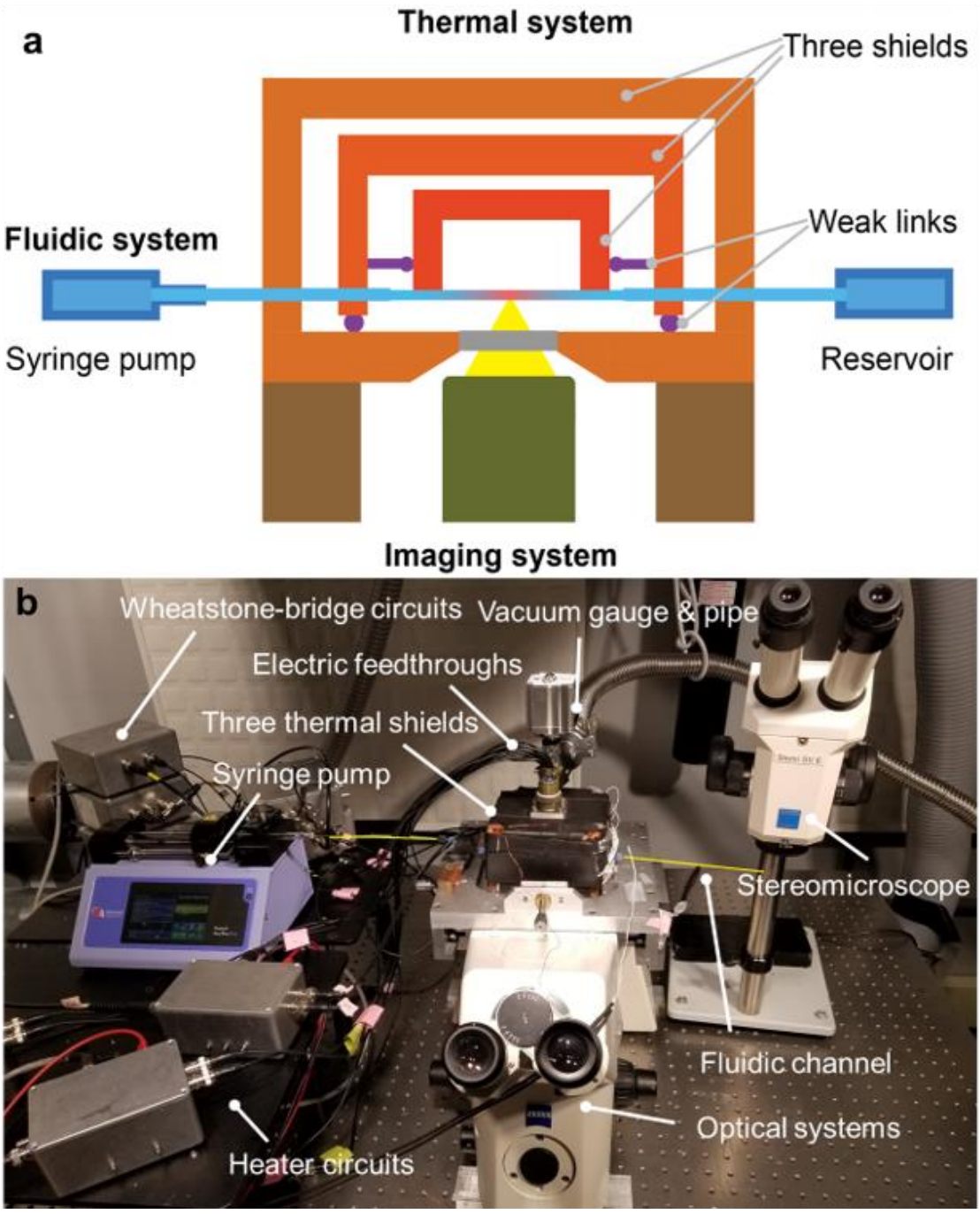

Figure 3.10 Experimental setup.
(a) Schematic depicting the three subsystems in our calorimeter: the fluidic system (shaded in blue) with the syringe pump and reservoir for sample handling, the optical imaging system (green) focused to the center of the capillary tube and the thermal system involving the three shields with weak thermal links (between OS and MS, MS and IS shown in purple) mounted on the microscope stage. (b) Our lab experimental settings. Note that the reservoir and CCD camera are not shown here.

3.6.1 Heat output measurement protocol and analysis

To establish the applicability of our system to biological measurements, we performed metabolic measurements on individual *C. elegans*. A typical measurement in our calorimeter involves five phases in Figure 3.13: first, establishing a baseline T_{th} (shown in gray) without a worm in the sensing capillary and a flow rate of 100 nl/min (all measurements reported here were performed at this flow rate). The worm is then loaded from an external reservoir under visual inspection at a larger flow rate of ~2-10 µl/min (shown in violet). Once the worm is loaded and properly localized in the sensing capillary tube, the flow rate is reduced to 100 nl/min, for continuously recording its heat output and for monitoring its activity (see Methods) via video microscopy (indicated by orange region in Figure 3.13(a)) for a desired time (~1-2 hrs). This optimal flow rate was chosen so as to both replenish the oxygen content in the fluidic medium (typical oxygen concentration < 8 mg.O_2/l at atmospheric pressure), thus avoiding oxygen deprivation of the worm (maximum reported oxygen consumption of 16 ng.O_2/h/worm[107]), and holding the worm in the desired location, which is facilitated by both the flow and the borosilicate fiber stopper (see Figure 3.11(b)). This approach solves the difficult task of constraining the worm[124] to the center of the sensing capillary while not inhibiting its natural swimming behavior. After monitoring the worm for the desired time interval, it is unloaded by reversing the flow at rates of 2-10 µl/min (shown in blue in Figure. 3.13(a)). Once the worm is unloaded from the sensing capillary, the temperature (shown in grey) of the capillary is again recorded to confirm the stability of the reference temperature (T_{th}). The worm is then transferred to Nematode Growth Medium (NGM) Agar plate, to feed and grow (room temperature 22° C), and the measurement cycle is repeated the following day, thus monitoring the metabolic heat changes of the same individual worm through its life-cycle. Maintaining such a small heat resolution while

continuously replenishing nutrients and oxygen has not been possible in the most sensitive calorimeter[20], where the cells die within 20 minutes of their measurement due to lack of oxygen.

3.6.2 Vacuum system in Ultra-low Noise Measurement Environment

All measurements in this experiment were performed in custom-made high vacuum (< 10 μTorr) chamber. Two vacuum pumps, a dry scroll pump (Agilent IDP-10) and a turbomolecular pump (Agilent TwisTorr 84FS), are serially connected to vacuum chamber (Outer shield, or OS). A foreline vacuum hose is connected to the Outer Shield and the vacuum pressure level is monitored by a pressure gauge (MKS 925 MicroPirani Transducer). All the gaps are sealed with Viton® O-rings. Electrical signals for MS/IS temperature control and calorimeter thermal sensing are delivered through 19-pin electrical feedthroughs (JANIS). Finally, The tubing system is passed through microfluidic connectors (MicroTight® Adapter PEEK 1/16" ID x 360 μm w/Fittings) on the OS that act as vacuum feedthroughs to the outside. The instrument was housed inside an ultra-low noise facility where the ground vibrations were attenuated to meet the requirement of NIST-A standard. Temperature drift in the room where the experimental setup is located was actively controlled to be within <100 mK around the set-point temperature (295 K).

3.6.3 Fluidic system

To establish the applicability of our system to biological measurements, we performed metabolic measurements on an individual *C. elegans*. A distinctive feature of biocalorimetry is that it requires a fluid or air supply to sustain physiological activities. The liquid system is integrated into biocalorimeter to sustain *C. elegans* activity. In addition, this fluidic system is used for delivering *C. elegans* into the measurement chamber which is at the center of the suspended tubes in the vacuum chamber. We use S-basal as a medium for the experiment. A syringe pump (Harvard Apparatus Pump 11 Pico Plus Elite) with a syringe (Hamilton® 100μL) infuses or

withdraws a liquid in a various flow rates from 1 nL/min to 100μL/min. A typical measurement in our calorimeter is described below.

Step 1)

Establishing a baseline T_{th} (shown in gray) without a worm in the sensing capillary at a flow rate of 100 nl/min (all measurements reported here were performed at this flow rate). This step is important because the heat output quantification is acquired by the increased temperature from the baseline temperature (T_{th}). If baseline temperature is unstable or drifting, it is impossible to precisely measure applying heat on the sensing chamber.

Step 2)

The worm is then loaded from an external reservoir under visual inspection at a larger flow rate of ~2-10 μl/min (shown in violet in Figure 3.13 (a)). Before this step, locating *C. elegans* to the reservoir should be preceded. The *C. elegans* is transferred to the reservoir from Nematode Growth Medium (NGM) Agar plate using a pipette. First, drop an S-basal liquid using a 10 μl volume pipette onto the *C. elegans* Agar plate. Subsequently, *C. elegans* starts swimming on this liquid drop and then approaching pipette proximity to the liquid drop and soak *C. elegans*. Afterward, transfer this *C. elegans* into the fresh S-basal medium reservoir. We note that this *C. elegans* should be recollected from this reservoir not to transfer *E. Coli* into the calorimeter which disturbs *C. elegans* metabolic heat generation measurement. *C. elegans* is again soaked from the S-basal reservoir and transferred to the reservoir for loading. The reservoir is on a stereomicroscope (Zeiss Stemi Sv 6) so that an entrance of PEEK tube can be focused to locate *C. elegans*. When the end of PEEK to is proximity to the *C. elegans*, increase withdraw flow rate of ~2-10 uL/min to pull *C. elegans*. The loading procedure takes ~1-10 mins which are dependent on

the flow rate and *C. elegans* activity. If *C. elegans* is reluctant to follow the liquid flow, it takes longer to reach the imaging region.

Step 3)

Once the worm is loaded and properly localized in the sensing capillary tube, the flow rate is reduced to 100 nl/min, for continuously recording its heat output and for monitoring its activity via video microscopy (indicated by orange region in Figure 3.13(a)) for a desired time (~1-2 hrs). It is noted that we also have tried other conditions, such as different flow rates and monitoring periods. When flow rate is lower than 100 nl/min, the G_{Th} decrease is advantageous but *C. elegans* often escapes from the sensing chamber. When the flow rate is higher than 100nL/min increases G_{Th} and also *C. elegans* becomes less active to secure their position under aggressive flow condition.

As a careful consideration, this optimal flow rate (100 nL/min) was chosen so as to both replenish the oxygen content in the fluidic medium (typical oxygen concentration < 8 mg.O_2/l at atmospheric pressure), thus avoiding oxygen deprivation of the worm (maximum reported oxygen consumption of 16 ng.O_2/h/worm[107]) and holding the worm in the desired location, which is facilitated by both the flow and the borosilicate fiber stopper (see Figure 3.11(b)). This approach solves the difficult task of constraining the worm to the center of the sensing capillary while not inhibit its natural swimming behavior.

Step 4)

After monitoring the worm for the desired time interval, it is unloaded by reversing the flow at rates of 2-10 µl/min (shown in blue in Figure 3.13(a)). It is noted that the syringe should have at least more than 50 µl/min for the case when *C. elegans* does not come out from the tube easily. In that case, I would recommend withdrawing a liquid again until *C. elegans* reaches to the

monitoring window. Once the *C. elegans* locates to the monitoring window and liquid volume in the syringe is over a half (50 µl), then infusing a syringe pump to unload *C. elegans*.

Step 5)

Once the worm is unloaded from the sensing capillary, the temperature (shown in grey) of the capillary is again recorded to confirm a stability of the reference temperature (T_{th}). It is noted that the reference temperature is identical to the baseline temperature, which indicates that the system including the calorimeter thermal reservoir is stable over the measurement. The worm is then transferred to Nematode Growth Medium (NGM) Agar plate, to feed and grow (room temperature 22° C), and the measurement cycle repeated the following day, thus monitoring the metabolic heat changes of the same individual worm through its life-cycle. Maintaining such a small heat resolution while continuously replenishing nutrients and oxygen has not been possible in the most sensitive calorimeter[119], where the cells die within 20 minutes of their measurement due to lack of oxygen.

3.6.4 Optical Imaging

Our calorimeter incorporates good optical access to the central region of the sensing capillary tube, which aids in trapping and monitoring the activity of the *C. elegans*. This optical imaging system enables us to verify *C .elegans* activity and its condition during the measurement. In addition, we could estimate the size of the worm under study from these images.

Though systems employing multiple shields to achieve thermal stability are well established, integrating an optical imaging capability is challenging as this naturally couples environmental fluctuations into the system through radiative coupling and the illumination source. A combination of IR reflective (Hot Mirror-Edmund Optics) and IR absorptive (Heat absorbing KG5 Schott filter) windows, sealed to the bottom part of the OS (see Figure 3.5) reduce the

coupling to the outer environment by reflecting IR radiation (~90%) to the environment and absorbing the remaining transmitted radiation. The temperature-controlled calorimeter is mounted on an inverted microscope (ZEISS Axiovert 200) and imaging is performed with epi-illumination through a 10x objective (CFI Plan Fluor DL 10XF). A DC power supply (Agilent 6033A) provides power (3V, 0.75A) to the Halogen light source while a CCD camera (RET-4000R-F-M-12-C) controlled through Micro-Manager 1.4.22 acquires images at 1 frame per second. The minimum illumination that provides a legible image at an exposure time of 0.5 sec is chosen to minimize thermal instabilities due to the light source fluctuations, which results in a temperature rise of ~1 mK (corresponding to ~27 nW) on both sensing and matching capillary tubes. We note that all thermal signals reported here were measured under this illumination setting.

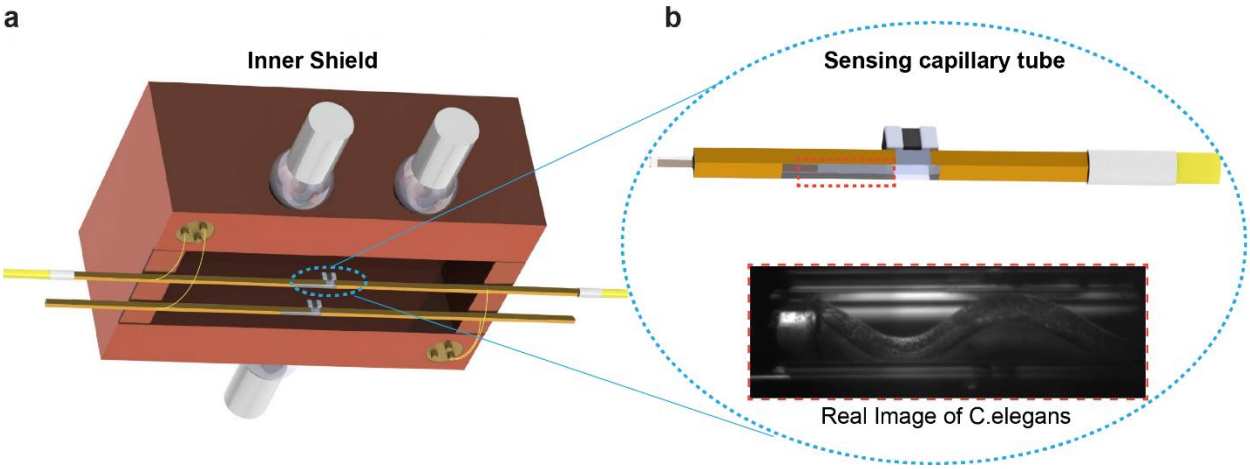

Figure 3.11 An image of *C. elegans* in thesensing capillary tube
(a) Illustration of IS assembly (not to scale) showing two capillary tubes, the sensing capillary with a PEEK tubing assembly and the matching capillary, with respective thermistors connected in a Wheatstone bridge configuration to extract differential thermal signal. (b) Magnified view of the ringed area in (a), depicting the capillary tube coated with gold on all four sides, except for the central region, where the C. *elegans* is localized, and instrumented with a thermistor to record the temperature. A borosilicate stopper traps the C. *elegans* in the center of the sensing capillary tube. A CCD image (marked in red dashed line) of a trapped C. *elegans* during a reference measurement shows the corresponding stopper and Au layer.

3.6.5 Estimating the size and activity of C. elegans

The mass/volume of an individual *C. elegans* needed for obtaining the mass-specific properties was estimated from the images captured during the measurement. Considering the axisymmetric structure of the organism, the body is carefully divided into small sections of cylinders along the length of organism (Fig. 3.12(a)). The relevant dimensions (pixel lengths) for each section (diameter D_n and width H_n) were measured in ImageJ with the appropriate calibration of the microscope' magnification. The volume of the organism is the sum of the volumes of all cylindrical sections. The mass of each organism is then derived from the total estimated volume with the density considered to be ~ 1.08 g/cc[125].

$$\text{Volume} = \sum_{n=1}^{N} \frac{\pi D_n^2 H_n}{4} \tag{3.1}$$

An activity factor is defined to quantitatively represent the organism's activity which is derived by performing the following image analysis in ImageJ on a stack of images collected during the measurement at a frame rate of 1 sec. Initial brightness and contrast adjustments are performed on two image stacks, where the second image stack is a duplicate of the first with a single frame offset. The two stacks are then subtracted to create a new stack which now represents the organism activity, i. e. subtracting a frame at $(n+1)^{th}$ sec (Fig. 3.12(b)) from that at the n^{th} sec eliminates the motionless background and captures only the movement of the organism. To quantify this movement, the mean pixel intensity of each frame was then calculated and converted to a dimensionless activity factor ranging from 0 to1, where 0 and 1 indicate the lowest and the highest activity levels of a given organism. We note that absolute quantities can be used for activity comparison between Wild-type and *daf-2* organisms, instead of normalized quantities.

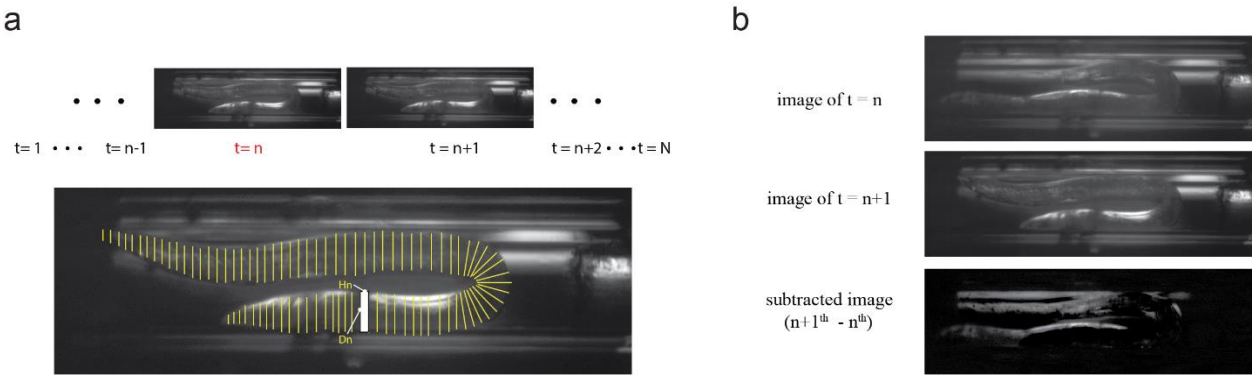

Figure 3.12 Size measurement and analysis of *C. elegans*.
(a) *C. elegans* size measurement. (Step 1) Choose a clear image from the acquired image stack. (Step 2) Divide the organism into small sections manually. (Step 3) Sum all volumes by acquiring the diameter (D_n) and thickness (H_n) of small cylinders. (b) *C. elegans* activity analysis: Image at time t = n is subtracted pixel-wise from image at t = n+1, resulting in the bottom image. Intensity (brightness) of each pixel in the subtracted image indicates the movement of the organism at that location.

3.6.6 Sample preparation and control

The nematodes were maintained at 20° C on NGM agar plates with OP50 *E. coli* as food source, according to standard protocols[126]. The following strains were used in our studies: Bristol N2 (used as wild-type), *daf-2(e1370).* For heat output measurements, the worms were transferred to the sensing capillary tube at 25° *C*, which was filled with S-basal buffer.

3.7 Results

In all our measurements, we observe that the worm's activity included prolonged periods of rapid swimming and resting periods, which are reflected, as expected, in distinct thermal signals. A normalized activity factor (see Chapter 3.6.5) that quantifies worm activity shows that the metabolic heat output is strongly correlated with activity (correlation coefficient ~0.82, see Figure 3.13(b)). Note that the blue line in Figure 3.13(b) shows a representative activity trace from a single *C. elegans,* while the red line presents simultaneously obtained metabolic heat output. From the measured thermal signal, we extract two metabolic heat output readings, which we call the

Average Metabolic Rate (AMR) and the Basal Metabolic Rate (BMR) (red and blue dashed lines respectively in Figure 3.13(b)). AMR is the average of the thermal signal in a 30-minute window (after an initial thermal equilibration time of 15 minutes) and BMR is the average of the metabolic heat output in the worm's resting state. We define the worm to be in resting state when activity factor is below 0.25 (green shaded region in Figure 3.13(b)). These measurements clearly demonstrate our system's unique capability to monitor activity-related metabolic changes in single nematode worms.

Here, all the measurement was done within 1~2 hours because metabolic heat output decreases over time due to lack of sufficient nutrition. The decrease of metabolic rate might be due to two reasons: slower activity over time or basal metabolic rate decrease. We confirmed that the decrease is related to the basal metabolic decrease. While total metabolic heat rate started to decrease after 1 hour, Figure 3.14 (a) clearly shows that the activity factor did not decrease after hours of measurement. To further calculate the decrease of metabolic rate, *C. elegans* metabolic rate was monitored up to 12 hours and a decrease rate of metabolic heat output was - 4 %/hour. The decrease rate means that the total metabolic heat output becomes a half of initial output after 12 hours without food supply. Our system could not accommodate *C. elegans* food because *E. coli*, typical food for *C. elegans* also generates heat which disturbs thermal signals from *C. elegans*[126]. For this reason, all *C. elegans* metabolic heat output data reported in the following parts is measured within 2 hours. In addition, all AMR and BMR are defined at the first 30-minute measurement range to avoid confusion between normal and starving *C. elegans*.

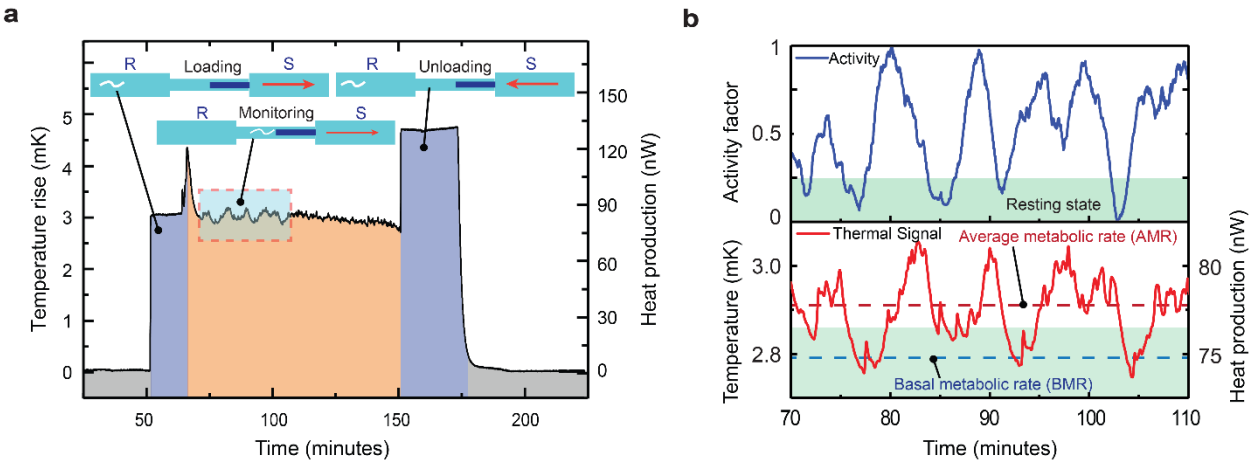

Figure 3.13 *C. elegans* metabolic heat output measurement and analysis.
(a) A typical procedure to measure heat output from a single *C. elegans* involves establishing an initial reference (gray region), followed by loading the worm (violet region) from the reservoir side (R) with a syringe pump (S) at withdraw flow rates (R→S) of ~2-10 µl/min. The orange region indicates the monitoring phase (1-2 hrs), followed by unloading (R←S, violet region) at flow rates of ~2-10 µl/min. (b) Temperature rise (red plot in bottom panel) and activity factor (blue plot in top panel) of a reference measurement (marked blue region in fig. 3a). In the panel showing the activity factor, the worm's resting activity level is highlighted in green. From the corresponding metabolic signal, BMR (blue dashed line, bottom panel) is derived. AMR (red dashed line, bottom panel) is determined by averaging the thermal signal in a 30 minute time interval.

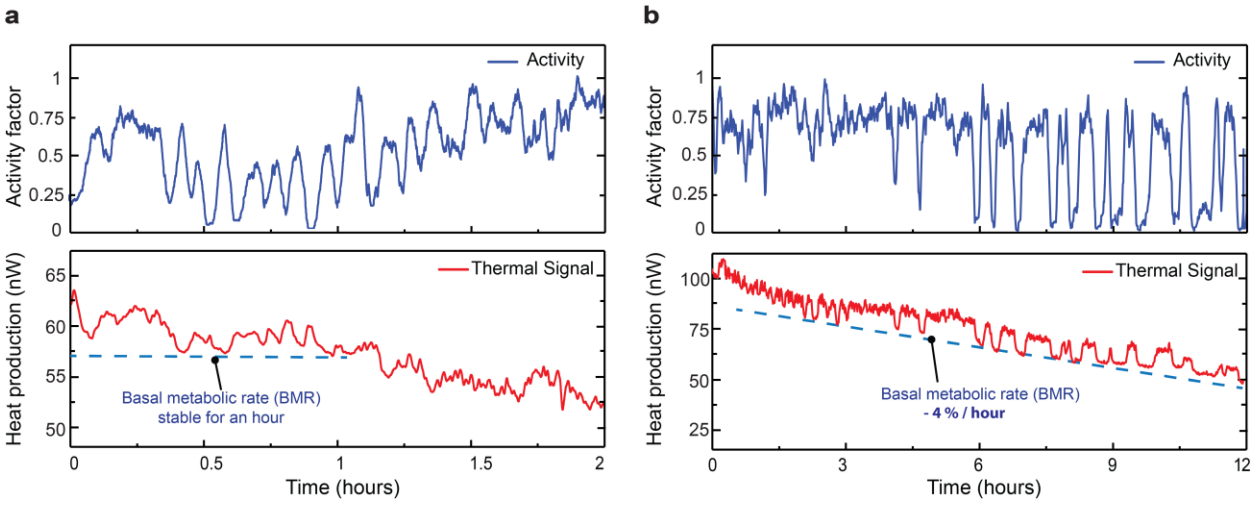

Figure 3.14 2-hour and 12-hour *C. elegans* metabolic heat output measurement and analysis.
(a) 2-hour heat production rate (red plot in bottom panel) and activity factor (blue plot in top panel) of a *reference C. elegans*. In the panel showing the activity factor, the worm's activity factor does not decline for two hours and even slightly increases after one hour. On the other hand, metabolic heat production was stable in the first hour but steadily decreases in the second. (b) 12-hour measurement on another *C. elegans*. Note that activity factor did not decrease over 12 hour measurement but metabolic heat rate decreases by 4% per hour. As a result, the metabolic heat output after 12 hours becomes half of the initial metabolic heat output.

3.7.1 Size-dependent metabolic measurements on N2 wild-type at different developmental stages

To investigate the metabolic changes during development, we monitored the AMR of N2 wild-type strain from L1 larval stage to the adult stage (day 4). Since the size of *C. elegans* increases by more than an order of magnitude over the course of their development, it is expected that early-stage *C. elegans* metabolic heat output is smaller. As plotted in Figure 3.15(a), our measurements reveal the metabolic heat output to vary from ~4 nW for the L1 stage to ~100 nW for the adult stage, more than a 20-fold change during their development. The metabolic heat output increased with the developing worm stage and is consistent with the previously observed oxygen consumption rates and heat output measurement performed on large number of worms[109,113,127].

Furthermore, we report metabolic heat output measurements from 61 N2 wild-type specimens (Figure 3.15(b), red triangles for AMR and blue triangles for BMR) as a function of weight. The weight (volume times density) of each worm was estimated by analyzing the 2D images captured from the imaging system (see Chapter 3.6.5). These measurements indicate that the average mass-specific AMR and BMR in Figure 3.15(c) are 55.8 ± 14.45 μW/mg and 52.17 ± 12.65 μW/mg, respectively, demonstrating our calorimeter's ability to delineate small changes in activity-related metabolic heat output from that of the resting state (~ 7% increase above BMR). In these measurements, the metabolic heat output of individual *C. elegans* worms increased with activity from 5-25% relative to the observed BMR. Further, it is known that the relationship between any organism's metabolic rate and size is expected to follow a simple exponential scaling law[128], described as $Q = aM^b$, where *Q*, *M*, *a* and *b* are basal-metabolic heat output, body size, scalar constant and exponential constant, respectively. Most studies focused on this exponential

constant *b* across species (inter-specific) of animals ranging from unicellular microbes to elephants[129], including in *C. elegans*[130]. Here, we deduce an exponential constant of 0.76 ± 0.06 (see Figure 3.15(d)) from the metabolic rate measurements (BMR) of wild-type worms (intra-specific) at different stages (L3 – Day 3), which concurs with the reported inter-specific value of 0.72 ± 0.09[130]. Thus, our work shows that the above scaling law is applicable to adult *C. elegans* intra-specifically and predicts the mass-specific metabolic rate across developmental stages.

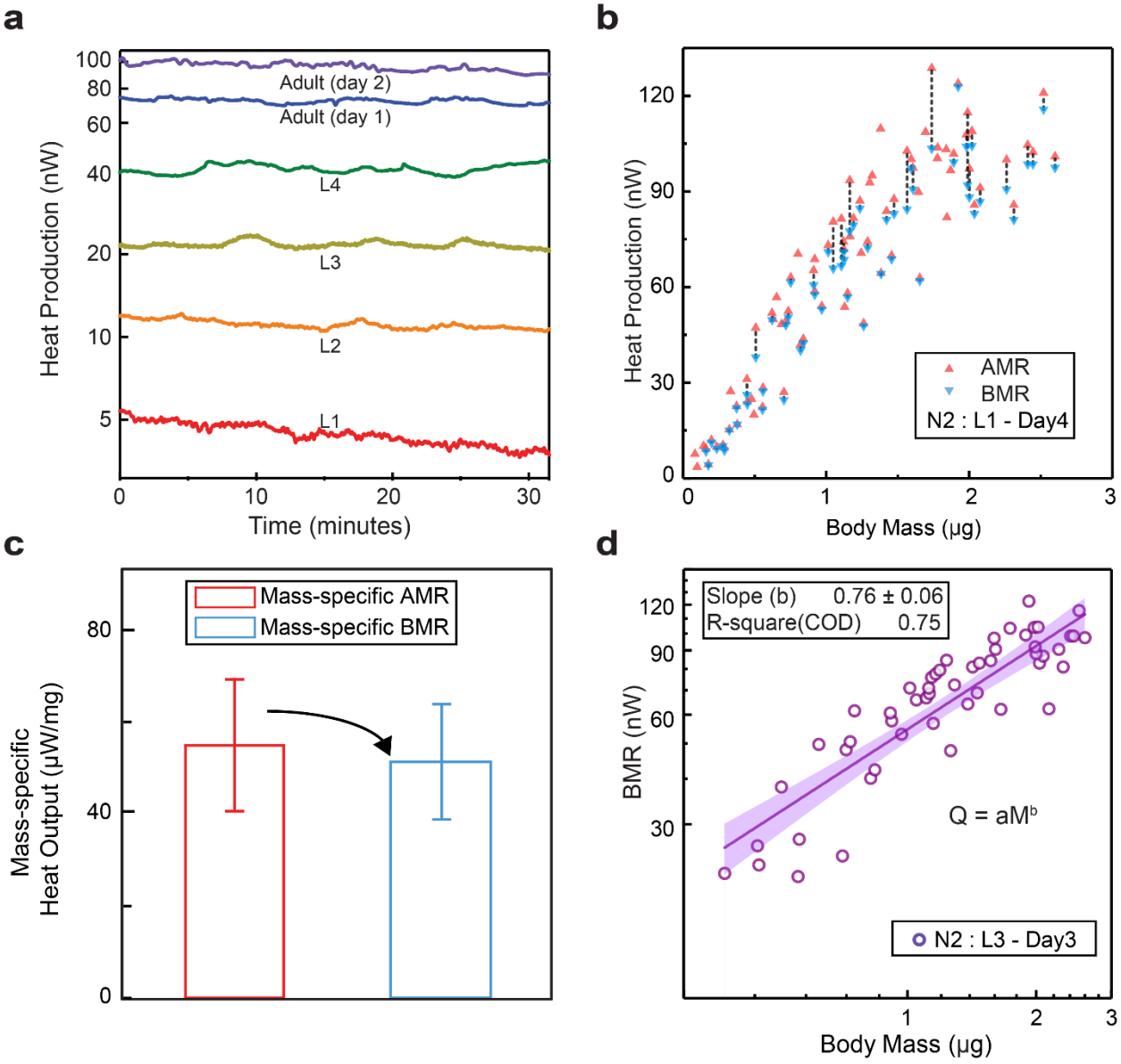

Figure 3.15 Size-dependent metabolic heat output measurements on N2 wild-type.
(a) Real-time metabolic heat output profiles of referential C. *elegans* from L1 stage to Adult (Day 2) stage. (b) Metabolic heat output measurements of 61 wild-type worms at different developmental stages from L1 to Adult (Day 4). The red and blue triangles represent the AMR and BMR of individual worms, respectively, and are connected by a black dashed line to identify measurements from individual worms. (c) The inset shows the mass-specific AMR and BMR averaged over the entire sample set. (d) AMR vs. body size on a log-log plot to extract an allotropic scaling constant of 0.76. The purple solid line represents the best-fit with R-squared error of 0.75. The purple shaded region indicates the 95% confidence interval.

3.7.2 Comparison of metabolic heat output measurements on N2 and daf-2, a long-lived mutant

To further demonstrate our system's ability to detect differences in metabolic activities, we have performed age-dependent metabolic heat measurements on a long-lived mutant, *daf-2(e1370)*. It is well established that the mutations that reduce the activity of a gene called *daf-2* (insulin/insulin-like growth factor-1 receptor) double the worm's lifespan[115]. This gene, which controls the expression of multiple longevity genes, is known to affect several biological processes including development, metabolism, and resistance to stress. Assaying physiological factors like metabolic rates of such mutants in addition to the chronological lifespan measures could provide further insights into aging mechanisms[108]. In our studies, both the strains (N2 wild-type and *daf-2* mutant) are cultured and maintained at identical conditions (room temperature 22° C) and care was taken to perform the measurements under the same environmental conditions (inner shield temperature 25° C, flow rate 100 nl/min) for a consistent comparison. We performed metabolic rate measurements on adult wild-type and *daf-2* mutant worms across developmental stages Day 1 – Day 4 and observed significant differences in metabolic heat outputs (wild-type: 92.2 ± 17 nW, *daf-2*: 53.9 ± 8.7 nW) between both genotypes in Figure 3.16(a). In the case of wild-type, an increase in AMR from 78.3 ± 11.6 nW to 108.1 ± 9.1 nW is observed as the worm progresses from Day 1 – Day 4 in Figure 3.16(b). The metabolic rates of *daf-2* reveal a significant metabolic shift to lower rates with Day 1 worms showing an AMR of 61.8 ± 5.8 nW, which further drops to 45 ± 5.8 nW on Day 4. We note that the variations (±12 nW maximum) observed in the metabolic heat outputs of worms of the same age may result from the limited duration from which the AMR is determined, differences in the time of day when the measurements were taken or individual physiological variability, which further highlights our instrument's capability to discern such differences. Based on the size measurements from CCD

images, we also report age-dependent mass-specific AMR (Figure 3.16(c) and (d)) of the same sample set described above where it is known that metabolic rate normalized with protein content is negatively correlated with age of the adult worms[127]. We observe that the mass-specific AMRs of Day 1 wild-type and *daf-2* worms are significantly different with average values of 69.3 ± 9.6 μW/mg and 36.1 ± 5.7 μW/mg respectively, which further reduced to 42.9 ± 3.8 μW/mg and 27.8 ± 7.3 μW/mg on Day 4. The rate of decrease in mass-specific AMR of daf-2 (~ -2.7 μW/mg/day) is significantly small compared to that of wild-type (~ -9 μW/mg/day), suggesting a potential mechanism for increased longevity.

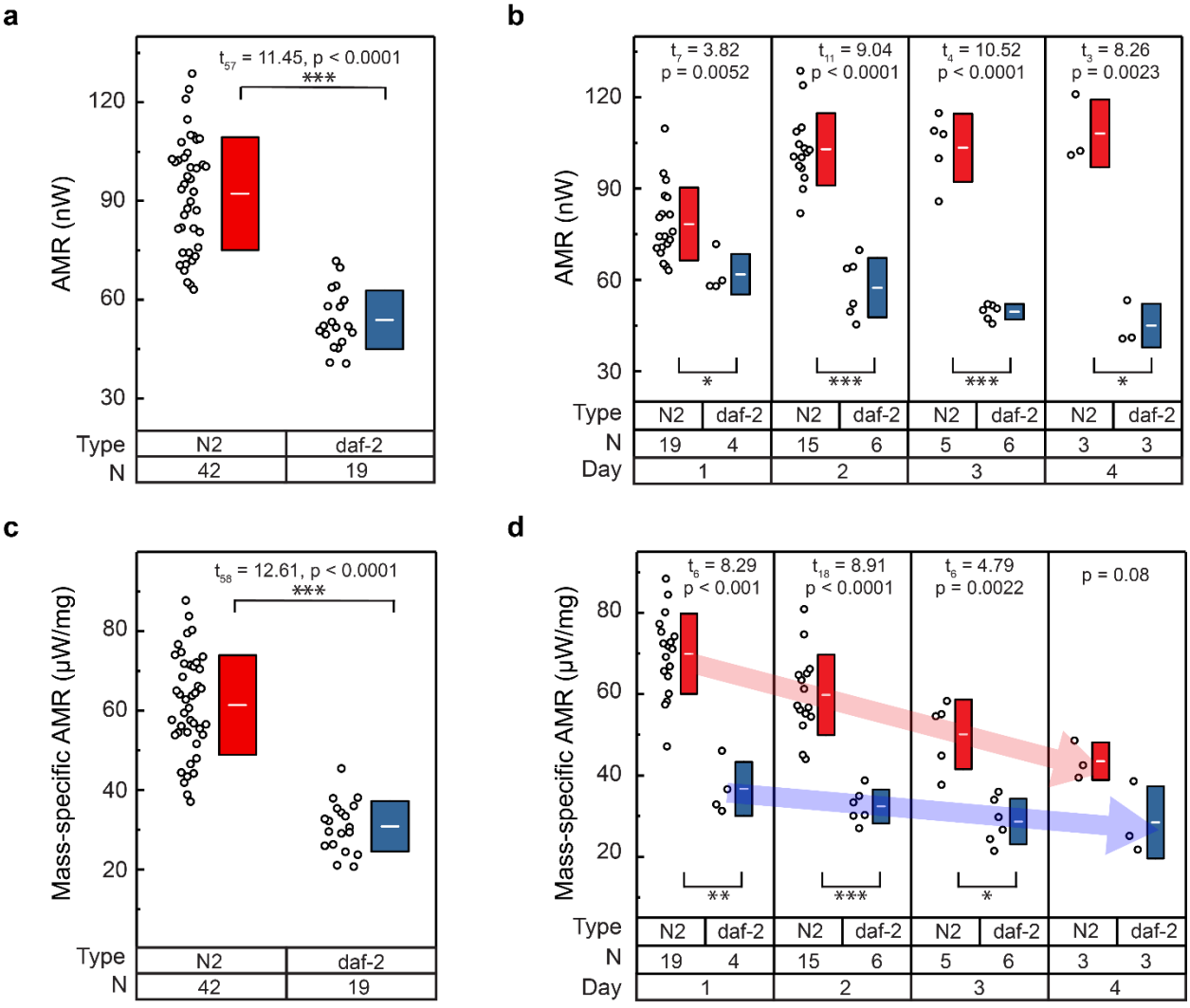

Figure 3.16 Age-dependent metabolic heat output measurements on N2 wild-type and *daf-2* mutant
(a) AMR from 42 worms of wild-type and 19 worms of *daf-2* at different stages of development. The white line in the center of the box represents the mean value of the corresponding set, while the height of the box represents the standard deviation. N indicates the corresponding number of samples. (b) AMR of several worms (black circles) of wild-type (red) and *daf-2* (blue) from Adult Day 1 to Day 4. (c) Mass-specific AMR of the sample set in Fig. 3.16a. (d) Mass-specific AMR is plotted for the same sample set in Fig. 3.16b. Statistical analysis was performed using two-tailed t-test. Statistical significance was determined for $p<0.05$; *$p<0.01$, **$p<0.001$, ***$p<0.0001$.

3.8 Discussion

We have successfully developed a sub-nW resolution (~270 pW with a temporal resolution of 100 sec) direct calorimeter with an integrated fluidic system and optical access for probing the metabolic rate of an individual model organism like *C. elegans*. This was accomplished by a combination of low thermal conductance capillary tubes (G_{th} ~ 27 μW/K) and high-resolution (ΔT ~ 10 μK) thermometry. This resolution presents more than two orders of magnitude improvement over the best calorimeters previously employed[118] in *C. elegans* studies and one order of resolution improvement over the most sensitive calorimeter[119] to date for biological studies. Further, we demonstrate for the first time that intermittent heat output measurements on the same individual worm over many developmental stages can be performed by continuously supplying oxygen and nutrition. We demonstrate the usefulness of this new instrument for studies on *C. elegans* by conducting a series of measurements on larval and adult stages. In fact, this work represents the first metabolic rate measurement on a single *C. elegans* from L1 to the adult stage. In addition, our calorimeter captures variations of metabolic heat generation corresponding to the worm's locomotive activity, which is shown to be about 5-25% above the BMR. Further, the worm's metabolic responses to external stimuli, like temperature and oxygen deprivation, can also be explored in our system. We note that our calorimeter, built from commercially available parts, without involving any complicated microfabrication processes, can in principle be employed to study metabolism of several other model organisms (e.g. *Chlamydomonas*, brown fat cells) whose metabolic output is in the nanowatt range.

Chapter 4

Discussion and Outlook

Overall, the calorimetric scanning thermal microscopy (C-SThM) probes successfully measured 1) quantized thermal conductance along the single-atomic junctions and 2) length-independent thermal conductance in single-molecule junctions. I contributed to establishing the applicability of the Wiedemann-Franz law for analyzing thermal transport in metallic atomic contacts. In contrast to work on monolayers and polymer bundles, our single-molecular junction measurement realizes the long-sought goal of identifying thermal conductance at the single-molecule level.

Still, several interesting studies have not been explored sufficiently due to the lack of experimental tools. The C-SThM resolution can even be more improved in 3 ways. First, the Pt heater layer thickness can be reduced. The current version Pt thickness is 30 nm and it is expected that the thickness may be reduced to ~20 nm while maintaining film uniformity. In this case, the total resistance can be increased by ~2 times, because the Pt resistivity in a thin film increases with decreasing thickness[88]. The increase of electrical resistance is beneficial for resistive thermometry to improve temperature resolution, because a corresponding temperature change becomes smaller with respect to the same electrical resistance change. Second, the size of sensing island where Pt serpentine is patterned can be larger. When the sensing island area (40 μm wide, 80 μm long) is

doubled, the integration of Pt serpentine can also be doubled, which results in a two-times-larger electrical resistance for resistive thermometry. In this case, the thermal time constant increase is inevitable but doubling a current thermal time constant (~25 msec) is still acceptable to stably holding atomic and molecular junctions for monitoring. Third, we can elongate the cantilever. A longer cantilever is advantageous for achieving low thermal conductance and better thermal resolution. Currently, the length is 200 μm and two times that length is possible with a less than 100 msec thermal time constant. Under these conditions, calorimeters are expected to achieve sub-pW/K resolution.

To summarize, the experimental advances presented using C-SThM probes will enable systematic studies of thermal transport through 1D chains of atoms, individual polymer chains, and other one-dimensional systems, which have been studied theoretically and computationally for more than half a century[64,102] but have not been probed experimentally because of the lack of experimental tools.

In metabolic studies, we have successfully developed ~270 pW direct calorimeter with an integrated fluidic system and optical access for probing the metabolic rate of an individual model organism like *C. elegans*. This resolution presents more than two orders of magnitude improvement over the best calorimeters previously employed[118] in *C. elegans* studies and one order of resolution improvement over the most sensitive calorimeter[119] to date for biological studies. This is the first time metabolic rate for a single *C. elegans* has been monitored over several developmental stages. In fact, this work represents the first metabolic rate measurement on a single *C. elegans* from L1 to the Adult stage. Further, the worm's metabolic responses to external stimuli, like temperature and oxygen deprivation, can also be explored in our system. There are not enough metabolism studies on *C. elegans* with respect to the temperature. Since *C. elegans* is a

poikilotherm, its temperature is determined by the environmental temperature. Interestingly, *C. elegans* lives more than 3 times longer at 15 ℃ than 25 ℃, but the key mechanism of longevity is insufficiently explored[109,131].

There are a few ways to improve this calorimeter. First, we can add more fluidic channels on both input and output to flow a different liquid medium. These modifications are useful because we can track metabolic changes in real-time during chemical treatment, such as norepinephrine or carbonyl cyanide 4-(trifluoromethoxy)phenylhydrazone (FCCP), which affects biological samples' metabolism and ATP synthesis.[118,119] Second, for probing biological samples smaller than *C. elegans*, such as single cells, we can adopt smaller capillary tubes to reduce thermal conductance. Moreover, thin-film thermistors, such as vanadium oxide (V_2O_5) or niobium nitride (NbN_x) which have high TCR but can be deposited through sputtering, can substitute for the current commercially available thermistor and reduce thermal radiation contributions.

Lastly, building thermal shields through aluminum machining can be simpler than that of copper. We started with copper due to its high thermal conductivity but later realized that aluminum would be acceptable in achieving uniform temperature at the outer shield. Furthermore, the middle shield, which isolated the outer shield from the inner shield, can be omitted because more than half of a calorimeter is already exposed to the outer shield, so most of the thermal fluctuation comes directly from the outer shield windows. For these reasons, changing the material (from Cu to Al) and removing the middle shield could be options for preventing many challenging steps.

Probing metabolic heat generation is a fundamental approach to elucidate metabolic activities, but it has not been improved due to experimental difficulties. We note that our calorimeter, which was built from commercially available parts without involving any

complicated microfabrication processes, can, in principle, be employed to study the metabolisms of several other model organisms (e.g. *Chlamydomonas*, Brown fat cells, etc.) whose metabolic outputs are in the nanowatt range. Furthermore, following the above suggestions to improve resolution and modify fabrication is expected to realize readily available calorimeters for probing various biochemical properties.

Bibliography

1 Chu, S. & Majumdar, A. Opportunities and challenges for a sustainable energy future. *Nature* **488**, 294-303 (2012).

2 Perez-Lombard, L., Ortiz, J. & Pout, C. A review on buildings energy consumption information. *Energ Buildings* **40**, 394-398 (2008).

3 Forman, C., Muritala, I. K., Pardemann, R. & Meyer, B. Estimating the global waste heat potential. *Renew Sust Energ Rev* **57**, 1568-1579 (2016).

4 Cullen, J. M. & Allwood, J. M. Theoretical efficiency limits for energy conversion devices. *Energy* **35**, 2059-2069 (2010).

5 Duro, J. A., Alcantara, V. & Padilla, E. International inequality in energy intensity levels and the role of production composition and energy efficiency: An analysis of OECD countries. *Ecol Econ* **69**, 2468-2474 (2010).

6 Chakravarty, S. & Tavoni, M. Energy poverty alleviation and climate change mitigation: Is there a trade off? *Energ Econ* **40**, S67-S73 (2013).

7 Cahill, D. G. *et al.* Nanoscale thermal transport. II. 2003-2012. *Appl Phys Rev* **1** (2014).

8 Cahill, D. G. *et al.* Nanoscale thermal transport. *J Appl Phys* **93**, 793-818 (2003).

9 Shi, L. *et al.* Evaluating Broader Impacts of Nanoscale Thermal Transport Research. *Nanosc Microsc Therm* **19**, 127-165 (2015).

10 Heremans, J. P., Dresselhaus, M. S., Bell, L. E. & Morelli, D. T. When thermoelectrics reached the nanoscale. *Nat Nanotechnol* **8**, 471-473 (2013).

11 Pop, E. Energy Dissipation and Transport in Nanoscale Devices. *Nano Res* **3**, 147-169 (2010).

12 Ghosh, S. *et al.* Extremely high thermal conductivity of graphene: Prospects for thermal management applications in nanoelectronic circuits. *Appl Phys Lett* **92** (2008).

13 Shakouri, A. Nanoscale thermal transport and microrefrigerators on a chip. *P Ieee* **94**, 1613-1638 (2006).

14 Kittel, C. *Introduction to solid state physics*. 8th edn, (Wiley, 2005).

15 Chen, G. *Nanoscale energy transport and conversion : a parallel treatment of electrons, molecules, phonons, and photons*. (Oxford University Press, 2005).

16 Cahill, D. G., Goodson, K. E. & Majumdar, A. Thermometry and thermal transport in micro/nanoscale solid-state devices and structures. *J Heat Trans-T Asme* **124**, 223-241 (2002).

17 Brites, C. D. S. *et al.* Thermometry at the nanoscale. *Nanoscale* **4**, 4799-4829 (2012).

18 Jeong, W., Hur, S., Meyhofer, E. & Reddy, P. Scanning Probe Microscopy for Thermal Transport Measurements. *Nanosc Microsc Therm* **19**, 279-302 (2015).

19 Carreto-Vazquez, V. H., Wojcik, A. K., Liu, Y. S., Bukur, D. B. & Mannan, M. S. Miniaturized calorimeter for thermal screening of energetic materials. *Microelectron J* **41**, 874-881 (2010).
20 Kim, K. *et al.* Radiative heat transfer in the extreme near field. *Nature* **528**, 387-391 (2015).
21 Thompson, D. *et al.* Hundred-fold enhancement in far-field radiative heat transfer over the blackbody limit. *Nature* **561**, 216-221 (2018).
22 Fiorino, A. *et al.* Nanogap near-field thermophotovoltaics. *Nat Nanotechnol* **13**, 806-811 (2018).
23 Kim, K., Jeong, W. H., Lee, W. C. & Reddy, P. Ultra-High Vacuum Scanning Thermal Microscopy for Nanometer Resolution Quantitative Thermometry. *Acs Nano* **6**, 4248-4257 (2012).
24 Reddy, P., Jang, S. Y., Segalman, R. A. & Majumdar, A. Thermoelectricity in molecular junctions. *Science* **315**, 1568-1571 (2007).
25 Cui, L. *et al.* Peltier cooling in molecular junctions. *Nat Nanotechnol* **13**, 122-127 (2018).
26 Agrait, N., Yeyati, A. L. & van Ruitenbeek, J. M. Quantum properties of atomic-sized conductors. *Phys Rep* **377**, 81-279 (2003).
27 Henry, A. & Chen, G. High Thermal Conductivity of Single Polyethylene Chains Using Molecular Dynamics Simulations. *Phys Rev Lett* **101** (2008).
28 Segal, D., Nitzan, A. & Hanggi, P. Thermal conductance through molecular wires. *J Chem Phys* **119**, 6840-6855 (2003).
29 Schwab, K., Henriksen, E. A., Worlock, J. M. & Roukes, M. L. Measurement of the quantum of thermal conductance. *Nature* **404**, 974-977 (2000).
30 Klockner, J. C., Burkle, M., Cuevas, J. C. & Pauly, F. Length dependence of the thermal conductance of alkane-based single-molecule junctions: An ab initio study. *Phys Rev B* **94** (2016).
31 Sun, T. & Morgan, H. Single-cell microfluidic impedance cytometry: a review. *Microfluid Nanofluid* **8**, 423-443 (2010).
32 Yeom, S. H., Kang, B. H., Kim, K. J. & Kang, S. W. Nanostructures in biosensor-a review. *Front Biosci-Landmrk* **16**, 997-1023 (2011).
33 Blum, L. c. J. & Coulet, P. R. *Biosensor principles and applications*. (M. Dekker, 1991).
34 Dittrich, P. S. & Manz, A. Lab-on-a-chip: microfluidics in drug discovery. *Nat Rev Drug Discov* **5**, 210-218 (2006).
35 de Jong, J., Lammertink, R. G. H. & Wessling, M. Membranes and microfluidics: a review. *Lab Chip* **6**, 1125-1139 (2006).
36 Lee, S. C., Hur, S., Kang, D., Kim, B. H. & Lee, S. J. The performance of bioinspired valveless piezoelectric micropump with respect to viscosity change. *Bioinspir Biomim* **11** (2016).
37 Bai, T. T. & Gu, N. Micro/Nanoscale Thermometry for Cellular Thermal Sensing. *Small* **12**, 4590-4610 (2016).
38 Fiorino, A. *et al.* Parallelized, real-time, metabolic-rate measurements from individual Drosophila. *Scientific Reports* **8** (2018).
39 Lamprecht, I. Calorimetry and thermodynamics of living systems. *Thermochim Acta* **405**, 1-13 (2003).
40 DeBerardinis, R. J. & Thompson, C. B. Cellular Metabolism and Disease: What Do Metabolic Outliers Teach Us? *Cell* **148**, 1132-1144 (2012).

41 Maskow, T. & Paufler, S. What does calorimetry and thermodynamics of living cells tell us? *Methods* **76**, 3-10 (2015).
42 Sadat, S., Meyhofer, E. & Reddy, P. Resistance thermometry-based picowatt-resolution heat-flow calorimeter. *Appl Phys Lett* **102** (2013).
43 Incropera, F. P. & Incropera, F. P. *Fundamentals of heat and mass transfer*. 6th edn, (John Wiley, 2007).
44 Sadat, S. *et al.* Room temperature picowatt-resolution calorimetry. *Appl Phys Lett* **99** (2011).
45 Dechaumphai, E. & Chen, R. K. Sub-picowatt resolution calorimetry with niobium nitride thin-film thermometer. *Rev Sci Instrum* **85** (2014).
46 Lee, W., Fon, W., Axelrod, B. W. & Roukes, M. L. High-sensitivity microfluidic calorimeters for biological and chemical applications. *Proceedings of the National Academy of Sciences of the United States of America* **106**, 15225-15230 (2009).
47 Kim, P., Shi, L., Majumdar, A. & McEuen, P. L. Thermal transport measurements of individual multiwalled nanotubes. *Phys Rev Lett* **87** (2001).
48 Cahill, D. G. Thermal-Conductivity Measurement from 30-K to 750-K - the 3-Omega Method. *Rev Sci Instrum* **61**, 802-808 (1990).
49 Paddock, C. A. & Eesley, G. L. Transient Thermoreflectance from Thin Metal-Films. *J Appl Phys* **60**, 285-290 (1986).
50 Maldonado, O. Pulse Method for Simultaneous Measurement of Electric Thermopower and Heat-Conductivity at Low-Temperatures. *Cryogenics* **32**, 908-912 (1992).
51 Min, S., Blumm, J. & Lindemann, A. A new laser flash system for measurement of the thermophysical properties. *Thermochim Acta* **455**, 46-49 (2007).
52 Kim, P., Shi, L., Majumdar, A. & McEuen, P. L. Mesoscopic thermal transport and energy dissipation in carbon nanotubes. *Physica B-Condensed Matter* **323**, 67-70 (2002).
53 Canetta, C. & Narayanaswamy, A. Sub-picowatt resolution calorimetry with a bi-material microcantilever sensor. *Appl Phys Lett* **102** (2013).
54 Cui, L. *et al.* Thermal conductance of single-molecule junctions. *Nature* **572**, 628-633 (2019).
55 Cui, L. *et al.* Quantized thermal transport in single-atom junctions. *Science* **355**, 1192-1195 (2017).
56 Crossno, J. *et al.* Observation of the Dirac fluid and the breakdown of the Wiedemann-Franz law in graphene. *Science* **351**, 1058-1061 (2016).
57 Cuevas, J. C. & Scheer, E. *Molecular electronics : an introduction to theory and experiment*. (World Scientific, 2010).
58 Scheer, E. *et al.* The signature of chemical valence in the electrical conduction through a single-atom contact. *Nature* **394**, 154-157 (1998).
59 van den Brom, H. E. & van Ruitenbeek, J. M. Quantum suppression of shot noise in atom-size metallic contacts. *Phys Rev Lett* **82**, 1526-1529 (1999).
60 Wheeler, P. J., Russom, J. N., Evans, K., King, N. S. & Natelson, D. Shot Noise Suppression at Room Temperature in Atomic-Scale Au Junctions. *Nano Lett* **10**, 1287-1292 (2010).
61 Ludoph, B. & van Ruitenbeek, J. M. Thermopower of atomic-size metallic contacts. *Phys Rev B* **59**, 12290-12293 (1999).
62 Evangeli, C. *et al.* Quantum Thermopower of Metallic Atomic-Size Contacts at Room Temperature. *Nano Lett* **15**, 1006-1011 (2015).

63 Lee, W. *et al.* Heat dissipation in atomic-scale junctions. *Nature* **498**, 209-212 (2013).
64 Dubi, Y. & Di Ventra, M. Colloquium: Heat flow and thermoelectricity in atomic and molecular junctions. *Rev Mod Phys* **83**, 131-155 (2011).
65 Chiatti, O. *et al.* Quantum thermal conductance of electrons in a one-dimensional wire. *Phys Rev Lett* **97** (2006).
66 Meschke, M., Guichard, W. & Pekola, J. P. Single-mode heat conduction by photons. *Nature* **444**, 187-190 (2006).
67 Jezouin, S. *et al.* Quantum Limit of Heat Flow Across a Single Electronic Channel. *Science* **342**, 601-604 (2013).
68 Partanen, M. *et al.* Quantum-limited heat conduction over macroscopic distances. *Nat Phys* **12**, 460-464 (2016).
69 Gotsmann, B. & Lantz, M. A. Quantized thermal transport across contacts of rough surfaces. *Nat Mater* **12**, 59-65 (2013).
70 Aradhya, S. V. & Venkataraman, L. Single-molecule junctions beyond electronic transport. *Nat Nanotechnol* **8**, 399-410 (2013).
71 Shen, S., Henry, A., Tong, J., Zheng, R. T. & Chen, G. Polyethylene nanofibres with very high thermal conductivities. *Nat Nanotechnol* **5**, 251-255 (2010).
72 Xiang, D., Wang, X. L., Jia, C. C., Lee, T. & Guo, X. F. Molecular-Scale Electronics: From Concept to Function. *Chem Rev* **116**, 4318-4440 (2016).
73 Rincon-Garcia, L., Evangeli, C., Rubio-Bollinger, G. & Agrait, N. Thermopower measurements in molecular junctions. *Chem Soc Rev* **45**, 4285-4306 (2016).
74 Smit, R. H. M. *et al.* Measurement of the conductance of a hydrogen molecule. *Nature* **419**, 906-909 (2002).
75 Xu, B. Q. & Tao, N. J. J. Measurement of single-molecule resistance by repeated formation of molecular junctions. *Science* **301**, 1221-1223 (2003).
76 Garner, M. H. *et al.* Comprehensive suppression of single-molecule conductance using destructive sigma-interference. *Nature* **558**, 415-419 (2018).
77 Wang, R. Y., Segalman, R. A. & Majumdar, A. Room temperature thermal conductance of alkanedithiol self-assembled monolayers. *Appl Phys Lett* **89** (2006).
78 Wang, Z. H. *et al.* Ultrafast flash thermal conductance of molecular chains. *Science* **317**, 787-790 (2007).
79 Meier, T. *et al.* Length-Dependent Thermal Transport along Molecular Chains. *Phys Rev Lett* **113** (2014).
80 Wang, X. J., Ho, V., Segalman, R. A. & Cahill, D. G. Thermal Conductivity of High-Modulus Polymer Fibers. *Macromolecules* **46**, 4937-4943 (2013).
81 Majumdar, S., Malen, J. A. & McGaughey, A. J. H. Cooperative Molecular Behavior Enhances the Thermal Conductance of Binary Self-Assembled Monolayer Junctions. *Nano Lett* **17**, 220-227 (2017).
82 Mosso, N. *et al.* Heat transport through atomic contacts. *Nat Nanotechnol* **12**, 430-433 (2017).
83 Sadeghi, H., Sangtarash, S. & Lambert, C. J. Oligoyne Molecular Junctions for Efficient Room Temperature Thermoelectric Power Generation. *Nano Lett* **15**, 7467-7472 (2015).
84 Weisenhorn, A. L., Hansma, P. K., Albrecht, T. R. & Quate, C. F. Forces in Atomic Force Microscopy in Air and Water. *Appl Phys Lett* **54**, 2651-2653 (1989).

85 Miner, A. C., Chapp, M., Li, D. Y. & Majumdar, A. A scanning probe microscopy based measurement tool for thermoelectric studies of nanostructures. *Twenty-First International Conference on Thermoelectrics, Proceedings ICT '02*, 325-328 (2002).
86 Hibbeler, R. C. *Engineering mechanics. Statics & dynamics*. 12th edn, (Prentice-Hall, 2010).
87 Sadat, S., Meyhofer, E. & Reddy, P. High resolution resistive thermometry for micro/nanoscale measurements. *Rev Sci Instrum* **83** (2012).
88 Zhai, Y. J. *et al.* Study on the resistance characteristic of Pt thin film. *Physcs Proc* **32**, 772-778 (2012).
89 Song, B. *et al.* Enhancement of near-field radiative heat transfer using polar dielectric thin films. *Nat Nanotechnol* **10**, 253-258 (2015).
90 Khan, A., Philip, J. & Hess, P. Young's modulus of silicon nitride used in scanning force microscope cantilevers. *J Appl Phys* **95**, 1667-1672 (2004).
91 Cui, L. *et al.* Study of radiative heat transfer in angstrom ngstrom- and nanometre-sized gaps. *Nat Commun* **8** (2017).
92 Olesen, L. *et al.* Apparent barrier height in scanning tunneling microscopy revisited. *Phys Rev Lett* **76**, 1485-1488 (1996).
93 Malen, J. A. *et al.* Identifying the Length Dependence of Orbital Alignment and Contact Coupling in Molecular Heterojunctions. *Nano Lett* **9**, 1164-1169 (2009).
94 Olesen, L. *et al.* Quantized Conductance in an Atom-Sized Point-Contact. *Phys Rev Lett* **72**, 2251-2254 (1994).
95 Krans, J. M. *et al.* Quantized Conductance in an Atom-Sized Point-Contact - Comment. *Phys Rev Lett* **74**, 2146-2146 (1995).
96 Olesen, L. *et al.* Quantized Conductance in an Atom-Sized Point-Contact - Reply. *Phys Rev Lett* **74**, 2147-2147 (1995).
97 Ashcroft, N. W. & Mermin, N. D. *Solid state physics*. (Holt, 1976).
98 Sivan, U. & Imry, Y. Multichannel Landauer Formula for Thermoelectric Transport with Application to Thermopower near the Mobility Edge. *Phys Rev B* **33**, 551-558 (1986).
99 Jain, A. & McGaughey, A. J. H. Thermal transport by phonons and electrons in aluminum, silver, and gold from first principles. *Phys Rev B* **93**, 081206(R) (2016).
100 Bergfield, J. P. & Stafford, C. A. Thermoelectric Signatures of Coherent Transport in Single-Molecule Heterojunctions. *Nano Lett* **9**, 3072-3076 (2009).
101 Jang, S. Y., Reddy, P., Majumdar, A. & Segalman, R. A. Interpretation of Stochastic events in single molecule conductance measurements. *Nano Lett* **6**, 2362-2367 (2006).
102 Li, N. B. *et al.* Colloquium: Phononics: Manipulating heat flow with electronic analogs and beyond. *Rev Mod Phys* **84**, 1045-1066 (2012).
103 Wadso, L. & Galindo, F. G. Isothermal calorimetry for biological applications in food science and technology. *Food Control* **20**, 956-961 (2009).
104 Barzilai, N., Huffman, D. M., Muzumdar, R. H. & Bartke, A. The Critical Role of Metabolic Pathways in Aging. *Diabetes* **61**, 1315-1322 (2012).
105 Finkel, T. The metabolic regulation of aging. *Nature Medicine* **21**, 1416-1423 (2015).
106 Cairns, R. A., Harris, I. S. & Mak, T. W. Regulation of cancer cell metabolism. *Nature Reviews Cancer* **11**, 85-95 (2011).
107 Braeckman, B. P., Houthoofd, K. & Vanfleteren, J. R. Assessing metabolic activity in aging Caenorhabditis elegans: concepts and controversies. *Aging Cell* **1**, 82-88 (2002).

108 Van Voorhies, W. A. Metabolism and aging in the nematode Caenorhabditis elegans. *Free Radical Biology and Medicine* **33**, 587-596 (2002).
109 Houthoofd, K. *et al.* DAF-2 pathway mutations and food restriction in aging Caenorhabditis elegans differentially affect metabolism. *Neurobiol Aging* **26**, 689-696 (2005).
110 Corsi, A. K., Wightman, B. & Chalfie, M. A Transparent Window into Biology: A Primer on Caenorhabditis elegans. *Genetics* **201**, 339-339 (2015).
111 Kaletta, T. & Hengartner, M. O. Finding function in novel targets: C-elegans as a model organism. *Nat Rev Drug Discov* **5**, 387-398 (2006).
112 Krijgsveld, J. *et al.* Metabolic labeling of C-elegans and D-melanogaster for quantitative proteomics. *Nature Biotechnology* **21**, 927-931 (2003).
113 Houthoofd, K. *et al.* Metabolism, physiology and stress defense in three aging Ins/IGF-1 mutants of the nematode Caenorhabditis elegans. *Aging Cell* **4**, 87-95 (2005).
114 Guarente, L. & Kenyon, C. Genetic pathways that regulate ageing in model organisms. *Nature* **408**, 255-262 (2000).
115 Lapierre, L. R. & Hansen, M. Lessons from C. elegans: signaling pathways for longevity. *Trends in Endocrinology and Metabolism* **23**, 637-644 (2012).
116 Uno, M. & Nishida, E. Lifespan-regulating genes in C. elegans. *Npj Aging and Mechanisms of Disease* **2** (2016).
117 Kenyon, C., Chang, J., Gensch, E., Rudner, A. & Tabtiang, R. A C-Elegans Mutant That Lives Twice as Long as Wild-Type. *Nature* **366**, 461-464 (1993).
118 Krenger, R., Lehnert, T. & Gijs, M. A. M. Dynamic microfluidic nanocalorimetry system for measuring Caenorhabditis elegans metabolic heat. *Lab Chip* **18**, 1641-1651 (2018).
119 Inomata, N., Toda, M. & Ono, T. Highly sensitive thermometer using a vacuum-packed Si resonator in a microfluidic chip for the thermal measurement of single cells. *Lab Chip* **16**, 3597-3603 (2016).
120 Assael, M. J., Botsios, S., Gialou, K. & Metaxa, I. N. Thermal conductivity of polymethyl methacrylate (PMMA) and borosilicate crown glass BK7. *Int J Thermophys* **26**, 1595-1605 (2005).
121 Glaser, H. J. History of the development and industrial production of low thermal emissivity coatings for high heat insulating glass units. *Appl Optics* **47**, C193-C199 (2008).
122 Tan, S., Wang, S., Saraf, S. & Lipa, J. A. Pico-Kelvin thermometry and temperature stabilization using a resonant optical cavity. *Optics Express* **25**, 3578-3593 (2017).
123 Unni, P. K. M., Gunasekaran, M. K. & Kumar, A. +/- 30 mu K temperature controller from 25 to 103 degrees C: Study and analysis. *Rev Sci Instrum* **74**, 231-242 (2003).
124 Hulme, S. E., Shevkoplyas, S. S., Apfeld, J., Fontana, W. & Whitesides, G. M. A microfabricated array of clamps for immobilizing and imaging C-elegans. *Lab Chip* **7**, 1515-1523 (2007).
125 Reina, A., Subramaniam, A. B., Laromaine, A., Samuel, A. D. T. & Whitesides, G. M. Shifts in the Distribution of Mass Densities Is a Signature of Caloric Restriction in Caenorhabditis elegans. *PloS One* **8** (2013).
126 Brenner, S. The genetics of Caenorhabditis elegans. *Genetics* **77**, 71-94 (1974).
127 Decuyper, C. & Vanfleteren, J. R. Oxygen-Consumption during Development and Aging of the Nematode Caenorhabditis-Elegans. *Comparative Biochemistry and Physiology a-Physiology* **73**, 283-289 (1982).

128 West, G. B. & Brown, J. H. The origin of allometric scaling laws in biology from genomes to ecosystems: towards a quantitative unifying theory of biological structure and organization. *J Exp Biol* **208**, 1575-1592 (2005).
129 West, G. B., Woodruff, W. H. & Brown, J. H. Allometric scaling of metabolic rate from molecules and mitochondria to cells and mammals. *Proceedings of the National Academy of Sciences of the United States of America* **99**, 2473-2478 (2002).
130 Klekowski, R. Z., Paplinska, E. & Wasilewska, L. Oxygen-Consumption by Soil-Inhabiting Nematodes. *Nematologica* **18**, 391-403 (1972).
131 Krajniak, J. & Lu, H. Long-term high-resolution imaging and culture of C. elegans in chip-gel hybrid microfluidic device for developmental studies. *Lab Chip* **10**, 1862-1868 (2010).